CARBON BASED NANOMATERIALS AS TRANSPARENT CONDUCTIVE ELECTRODES

A Thesis
Presented to
The Academic Faculty

by

Fernando Reiter

In Partial Fulfillment
of the Requirements for the Degree
Masters of Science in the
George W. Woodruff School of Mechanical Engineering

Georgia Institute of Technology
August 2011

CARBON BASED NANOMATERIALS AS TRANSPARENT CONDUCTIVE ELECTRODES

Approved by:

Dr. Samuel Graham, Advisor
School of Mechanical Engineering
Georgia Institute of Technology

Dr. Kyriaki Kalaitzidou
School of Mechanical Engineering
Georgia Institute of Technology

Dr. Baratunde Cola
School of Mechanical Engineering
Georgia Institute of Technology

Date Approved: April 25, 2011

In loving memory of older brother Sacha Reiter (May 5, 1970-June 16, 2009)

TABLE OF CONTENTS

PAGE NUMBER

ACKNOWLEDGEMENTS

First and foremost, I would like to thank God for his enduring love, teachings, and spiritual support throughout my college career.

I would like to thank my mother and my family for their love and support throughout my educational career. My mother, Ruth Balarezo, has spent many nights praying for my success and has always been my number one fan. She has supported me throughout every step of my life and has always gone out of her way to help me. The love of a mother is one that truly cannot be expressed in words and for that motherly love I am eternally grateful. I would also like to thank my step father Jose Carlos Del Risco for investing many nights to help me with my homework and teaching me how to learn on my own when I was in elementary school.

I would like to thank my girlfriend, Darlene Swan for supporting throughout my high and low points throughout graduate school. Most notably, I would like to thank her for supporting me emotionally when my older brother Sacha passed away during my first year of graduate school. I would also like to thank her for all the support she had given me during her many visits to help me advance my studies and research. Darlene made my relatively short journey in graduate school more comfortable and enjoyable.

I acknowledge all my close friends Carlos Vallin, Jose Felix Medina Pardo, Mihir Gaurang Pathak, Munir Gaurang Pathak, Praachi Dipak Jani, Alejandro Infante, Daniel Infante, Silvia Calderon, Francisco Gonzalez, Frank Gonzalez, and Judy Gonzalez for always being supportive of my studies, always willing to give a helping hand, and putting a smile on my face whenever I needed it.

I would like to thank my advisor Dr. Graham for his advisement, guidance, and patience throughout the course of this research. He was always willing to meet up with me multiple times during the week when I needed it most, especially when things went bad in the lab and I needed extra assistance. I would also like to thank him for his understanding and patience when my older brother passed away and for letting me take a short leave to cope and spend time with my family. I would also like to thank him for giving me the opportunity to do research and for taking me under his wing since I completed his undergraduate heat transfer course.

I would like to thank Dr. Anuradha Bulusu for her continual support throughout this work. This work could not have been possible without her. She provided much of the needed support with experiments and characterizing my samples with XPS. I acknowledge the many discussions that I have had with her and the lessons she taught me. She was always willing to explain something or lead me in the right direction whenever I was confused. She truly is a “teacher” in her own right.

I would like to thank Hossein Sojoudi for the CVD graphene samples provided for this work and for his assistance with annealing studies performed in this work. I acknowledge him for the many discussions I had with him and for asking me fundamental questions of my research that often pushed the limits of my understanding. Also his assistance in performing my annealing studies was invaluable and I am grateful for the countless hours he assisted me in the process.

I acknowledge Dr. Neal Armstrong and Gordon MacDonald for their assistance with the C-AFM and AFM measurements taken on my nanotube electrodes. I acknowledge Dr. Robert Haddon for providing graphene oxide samples for me to conduct experiments with.

Special thanks to Dr. Roderick Jackson for being a role model/mentor since I first joined the group as an undergrad in August 2008. His example, support with my experiments, and teachings have been essential for this work. He was always willing to help and answered my questions even after he had graduated from Georgia Tech.

I would like to thank Dr. Wayne Whiteman and Dr. Srinivas Garimella for being wonderful professors and for teaching me what it means to be a “mechanical engineer”. I am honored to have been instructed by such highly educated individuals and could have

not asked for better professors in my college career. I truly learned from the “best” and have the utmost respect for them.

I would like to Dr. Thomas Beechem and Dr. Adam Christensen for the time they took to answer my questions with regards to research and engineering in general. I would also like to thank the remaining Graham group members past and present Dr. Anusha Venkatachalam, Dr. Jimmy Granstrom, Dr. Namsu Kim, Premkumar Nagarathnam, Ashante Allen, Parisa Pour Shahid Saeed Abadi, Fatma Nazli Donmezer, William Thomas James, Yongjin Kim, Hyungchul Kim, Sukwon Choi, Steven Walker, Mark Gleva, Minseok Ha, Shweta Natarajan, Christopher Ford, Yishak Habtemichael, and Christopher Mandela Bynes.

I would like to thank my committee members Dr. Baratunde Cola and Dr. Kyriaki Kalaitzidou for their assistance with my master’s thesis. For their flexibility in meeting with me to discuss my thesis and for their support throughout the process.

I acknowledge the Center for Device and Material Information Technology Research (CDMITR), Center for Organic Photonics and Electronics (COPE), Materials Research Science and Engineering Center (MRSEC), and the George W. Woodruff school of Mechanical Engineering as funding providers.

Lastly, I would like to thank the Society of Hispanic Professional Engineers (SHPE) and the Office of Minority Education and Development (OMED) for helping minority students be successful engineers through their numerous educational initiatives.

LIST OF TABLES

LIST OF FIGURES

LIST OF ABBREVIATIONS

1D	One Dimensional
2D	Two Dimensional
3D	Three Dimensional
a	Graphene Lattice Vector
A_c	Cross-sectional Area
A_s	Surface Area
Ag	Silver
A/D	Acceptor/Donor
AFM	Atomic Force Microscopy
BZ	Brillouin Zone
C	Carbon
c	Speed of Light
C-AFM	Conductive Tip Atomic Force Microscopy
CBN	Carbon Based Nanomaterials
COOH	Carboxylic Acid
CMC	Sodium Carboxymethyl Cellulose
CMG	Chemically Modified Graphene
CNT	Carbon Nanotube
CVD	Chemical Vapor Deposition
D	Diameter
d	Thickness of Graphene Film
d_i	Varying Contact Spacings
DGU	Density Gradient Ultracentrifugation
DI	Deionized
DOS	Density of States

DMF	Dimethylformamide
E-Beam	Electron Beam
e	Electron Charge
E_{2D}	2 Dimensional Energy Dispersion Relation
E_{c}	Energy of the Conduction Band
E_{f}	Fermi Energy
E_{g}	Energy Gap
E_{s}	Separation Energy
E_{v}	Energy of the Valence Band
EG	Exfoliated Graphite
EL	Electroluminescence
eV	Electron Volt
$FeCl_3$	Iron Chloride
FLG	Few-Layer Graphene
g	Earth’s Gravitational Force
I_G/I_D	Graphitic to Defect Ratio
GIC	Graphite Intercalation Compounds
GO	Graphene Oxide
GPS	Graphene Puresheets
H_2	Hydrogen
H_2SO_4	Sulfuric Acid
HM	Hummer’s Method
HNO_3	Nitric Acid
HOPG	Highly-Oriented Pyrolytic Graphite
I	Current
IPA	Isopropyl Alcohol
ITO	Indium Tin Oxide

J	Current Density
k	Geometrical Correction Factor for Four Point Probe
K	Corners of 1st Brillouin Zone
L	Length
L_T	Characteristic Transfer Length
M	Middle point Between Corners of 1st Brillouin Zone
M-SWNT	Metallic Single Wall Carbon Nanotube
MCE	Mixed Cellulose Ester
MIS	Minimum industrial standard
n	Charge Carrier Density
N	Number of Unit Cells in Structure
NMP	N-methylpyrrolidone
NTN	Nanotube Network
OPV	Organic Photovoltaic
PDMS	Polydimethylsiloxane
PET	Poly(ethylene terephthalate)
p_loss	Resistive Power Loss
PMMA	Poly(methyl methacrylate)
R	Resistance
R_φ	Diameter Resistance
R_c	Contact Resistance
R_sh	Sheet Resistance
RGO	Reduced Graphene Oxide
RMS	Root Mean Square
RTA	Rapid Thermal Annealing
S	Spacing

Sc-SWNT	Semiconducting Single Walled Carbon Nanotube
SCCM	Standard Cubic Centimeters per Minute
SDBS	Sodium Dodecylbenzene Sulfonate
SDS	Sodium Dodecyl Sulfate
SEM	Scanning Electron Microscope
SiO_2	Silicon Dioxide
SLG	Single Layer Graphene
$SOCl_2$	Thionyl Chloride
SWNT	Single Wall Carbon Nanotube
t	Thickness
T	Transparency
TCE	Transparent Conductive Electrode
TCO	Transparent Conductive Oxide
TEM	Tunneling Electron Microscope
TiO_2	Titanium Dioxide
TLM	Transfer Length Method
UV Vis NIR	Ultraviolet Visible Near-Infrared
USSC	Ultrasonic Spray Coating
V	Voltage
VdW	Van der Waal Forces
W	Width
WEG	Worm-like Exfoliated Graphite
XPS	X-Ray Photoelectron Spectroscopy
w/v	Weight by Volume
Z_0	Impedance of Free Space

LIST OF SYMBOLS

ϵ_o	Permittivity of Free Space
ε	Energy of a Photon
ε_f	Final Energy
ε_g	Energy at Ground State
ε_i	Initial Energy of Photons from Monochromatic Laser
ε_v	Energy at Excited Virtual Energy State
ε_{2v}	Energy at Secondary Virtual Energy State
$\hbar$	Reduced Planck's constant
ρ	Resistivity
ρ_c	Specific Contact Resistance
σ	Conductivity
σ_{dc}	Direct Current Conductivity
σ_{op}	Optical Conductivity
μ	Charge Mobility
μ_0	Permeability of Free Space
Φ	Work Function
λ	Wavelength
λ_{mfp}	Mean Free Path
φ_b	Schottky Barrier
Γ	Center of 1st Brillouin Zone
ω	Angular Frequency
ω_i	Incident Photon Frequency
ω_p	Optical Phonon Frequency
χ	Electron Affinity

SUMMARY

Flexible organic optoelectronic devices have garnered much research interest due to their potential as lightweight, environmental friendly, and flexible devices. Particularly of interest are organic light emitting diodes (OLEDs) and organic photovoltaics (OPVs). Which have inverse principles of operations in that OLEDs consume power to emit light and OPVs absorb light to store energy for future power output. However, OLEDs and OPVs need a positive transparent conductive electrode for light to exit/enter the device and simultaneously allow for the injection/extraction of holes, respectively.

Optically transparent carbon based nanomaterials including graphene and single wall carbon nanotubes (SWNTs) are promising candidates as transparent conductive electrodes due to their high electrical conductivity coupled with high optical transparency, are robust materials that can be flexed several times with minimal deterioration in their electronic properties, and they do not require costly high vacuum processing conditions. Therefore, carbon based nanomaterials transparent electrodes are investigated in this work.

In practice carbon nanotubes are easily solution processed through the use of surfactants sodium dodecyl sulfate (SDS) and sodium cholate (SC). Allowing SWNTs to be deposited onto transparent substrates through vacuum filtration, ultrasonic spray coating, dip coating, spin coating, and inkjet printing. However, surfactants are electrically insulating, limit chemical doping, and increase optical absorption thereby decreasing overall performance of carbon based nanomaterial electrodes. Fortunately, surfactants can be removed through nitric acid treatment and annealing in an inert environment (e.g. argon), respectively.

In this thesis, the impact of surfactant removal on the electrode performance was investigated. The first goal of this thesis was to add to the fundamental understanding of the physics involved with the removal of surfactants for solution processed SWNT

electrodes through thermal and chemical treatments at both the nanoscale and the macroscale. Nitric acid treatments have been shown to p-dope SWNTs and remove the surfactant SDS. However, nitric acid p-doping is naturally dedoped with exposure to air, does not completely remove the surfactant SC, and has been shown to damage SWNTs by creating defect sites. Annealing at temperatures up to 1000°C is advantageous in that it removes insulating surfactants. However, annealing may also remove surface functional groups that dope SWNTs. Therefore, there are competing effects when annealing SWNT electrodes. The impacts on electrode performance were investigated through the use of conductive-tip atomic force microscopy, sheet resistance, and optical transmittance measurements.

The second goal of this thesis was to investigate the potential of graphene SWNT composite electrodes as high performing transparent electrodes. To this end, the optoelectronic properties and healing of defects of as-made and annealed graphene oxide SWNT composites electrodes where characterized. Comparisons were done with as-made and annealed SWNT electrodes to understand the individual effects on graphene oxide and SWNTs after thermal treatments at temperatures of 1000°C. Furthermore, the optoelectronic properties of a chemical vapor deposition grown graphene M-SWNT composite electrodes will be characterized to investigate improvements in electrode performance.

In this thesis, the knowledge gained on the impact of surfactant removal on SWNT electrode performance at the nanoscale and macroscale, was utilized to expand the present understanding of surfactant removal through thermal and chemical treatment. Furthermore, the optoelectronic properties of an M-SWNT electrode were found to have a considerable improvement by adding a layer of chemical vapor deposition grown graphene below and above the M-SWNT electrode. Finally, a suspected air leakage during the period of the work done on annealing graphene oxide SWNT composite electrodes produced post annealed samples with an observed increase in optical transmittance, decrease in sheet resistance, and increases in the graphitic to defect ratio (indicating the healing of defects). SWNT electrodes prepared for comparison and annealed in the same furnace with the suspected air leak exhibited similar behaviors; with the exception of mixed SWNTs experiencing an increase in sheet resistance. This was attributed to the removal of surface functional groups as was demonstrated in the annealing studies performed for the impact of the removal of surface functional groups. An extensive study of annealing SWNTs in a controlled oxygen environment was not performed due to time constraints and is left as future work.

CHAPTER 1 : INTRODUCTION AND MOTIVATION

1.1 The Importance of Optoelectronic Devices

Transparent conductive oxides (TCOs) permeate into numerous technological applications such as solar cells, display technologies, and lighting sources. A subset of TCO applications includes next generation flexible organic optoelectronic devices; which have garnered much research interest due to their potential as lightweight, environmentally friendly, and flexible devices. As such TCOs are an integral part of modern technology and emerging technologies.

Currently transparent conductive oxides in industry are dominated by indium tin oxide (ITO) or tin doped indium oxide[1]. Thin films of indium tin oxide in industry are used as the principal transparent electrode because of ITO's high electrical conductivity coupled with high optical transmittance. ITO is capable of delivering a thin film with optoelectronic properties of 10Ω/sq coupled with 85% optical transmittance at a wavelength of 550nm[2]. ITOs' remarkable optoelectronic properties are necessary to provide acceptable resistive capacitive delays for flat panel displays [2]. However, indium tin oxide is inherently brittle, strains as low as 1.5%[3] result in severe deterioration of electronic properties [4, 5], is not chemically stable[1], has poor transmittance in the blue-green visible regime[6], and a mismatch of ITO's work function with hole transport layers in organic light emitting diodes (OLEDs) typically creates significant barriers for hole injection [7]. Furthermore, the principal material in ITO, indium, is expensive with a cost of $565 per kilogram in 2010[8], is expected to climb to $1000 per kilogram[9], and prices as high as $3000 per kilogram are suggested by the Chinese press [9]. Moreover, ITO is typically deposited onto substrates through a sputtering process[10]. Sputtering is an inefficient process[11] which requires high vacuum[10] conditions thereby driving up manufacturing costs.

Transparent electrodes for flexible organic optoelectronic devices must possess high electrical conductivity coupled with high optical transparency, electrical stability after being flexed several times, resistance to mechanical fracture, and resistance to debonding from their substrates. Thus, requiring a replacement material to conventional indium tin oxide and requiring significant research on other potential candidates. However, flexible optoelectronic devices are advantageous over rigid optoelectronic devices in that they do not require costly high vacuum processing conditions, can be printed onto low-cost and light weight structures, are environmentally friendly via less material processing, and their flexible nature allows them to be implemented into novel applications. Examples of flexible organic optoelectronic devices include organic light emitting diodes (OLEDs) and organic photovoltaics (OPVs) as shown in Figure 1.1a and b ,respectively.

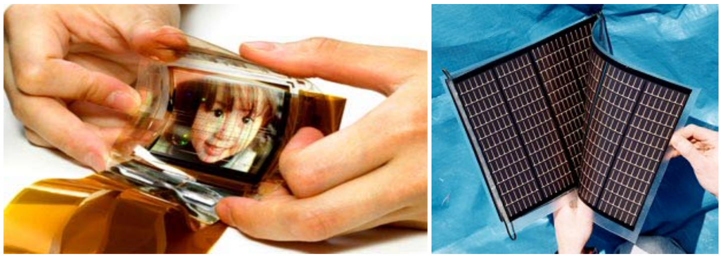

Figure 1.1 (a) Example of an organic light emitting diode (OLED) display[12]. (b) Example of an organic photovoltaic (OPV) device[13].

OLEDs and OPVs have inverse principles of operations, in that OLEDs consume power to emit light and OPVs absorb light to store energy for future power output. OLEDs can be used in applications ranging from lighting in flashlights to flat panel displays for televisions. Their flexible and lightweight nature allows them to be utilized in emerging technologies such as roll-up displays. Potentially low-cost OPVs are promising candidates as solar cells to meet the increasing energy demands, as their lightweight and flexible nature allows them to be incorporated into everyday products such as clothing, backpacks, and other wearable apparel.

Though flexible optoelectronic devices have advantages over traditional rigid optoelectronic devices, they are currently more expensive to manufacture and there are still many outstanding technical problems that still need to be resolved; most notably there is the need for a flexible transparent conductive electrode to replace ITO.

1.1.1 The Importance of Lighting Sources

Lighting sources are integral to society, however current technologies are not energy efficient and sustainable[14]. In literature it is typical to evaluate performance of lighting sources based on their luminous efficacy (lumens per watt). Historical and predicted luminous efficacies of light sources are presented in Figure 1.2. In Figure 1.2 it is shown that OLEDs are predicted to have significantly higher achievable luminous efficacies than traditional lighting sources (with the exception of LEDs) by 2020. Recently in 2010, General Electric developed a flexible white OLED with a 56 lumens per watt efficacy [15] which is consistent with the model shown in Figure 1.2.

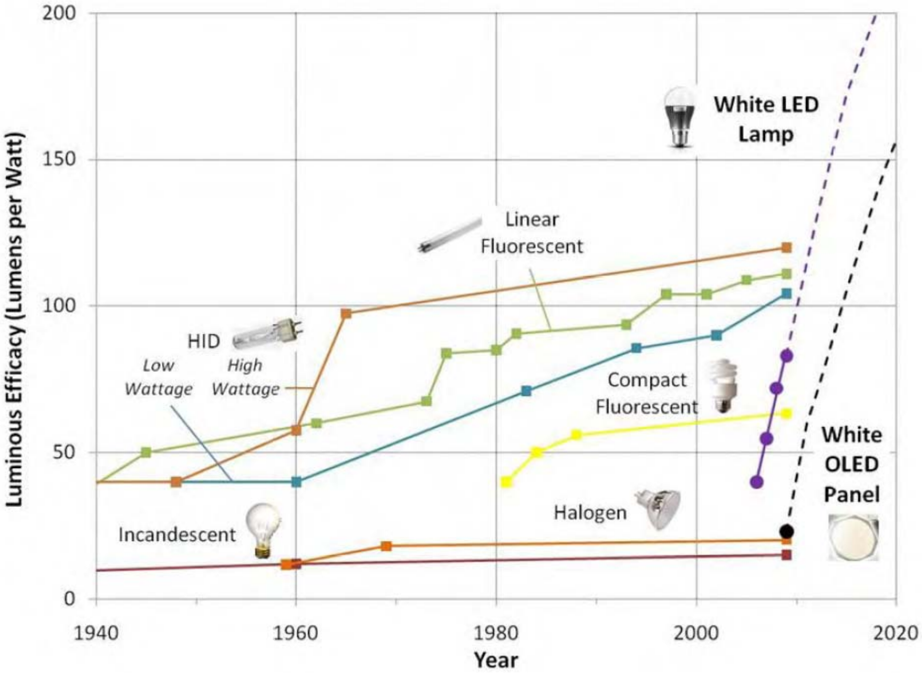

Figure 1.2 Luminous efficacy of light sources (Historical and Predicted). Taken from reference [14].

Currently organic light emitting diodes (OLEDs) are estimated to have maximum luminous efficacies of radiation of 350 lumens per watt [14]. The higher attainable lumens per watt efficacies for OLEDs allow for the possibility of more energy efficient lighting sources and displays than what is currently in the market. A white OLED panel is expected to have a cost of $6 per kilolumen by 2020[14]. While LEDs are expected to cost $1 per kilolumen[14].

Though OLEDs are more expensive than LEDs, OLEDs have a few advantages over LEDs. First, LEDs have narrow-band emissions which can emit light either in the ultraviolet, visible, or infrared regimes [14]. Thus in order for LEDs to produce white light for lighting applications, the LED's emission has to be converted into white light. This reduces luminous efficacy, requires more complicated design architectures, and complicates manufacturing processes [14]. While OLED devices have broad emission spectra, allowing for the possibility to tune emitted light and thereby making white light easier to produce. Furthermore, the device cost for OLEDs is expected to drop further in the future due to its ability of being printed onto low cost transparent substrates through an inkjet printing process [16]. This leads to more environmentally friendly processes through simpler manufacturing methods. Finally, the ability to tune emitted light removes the need for backlights in display technologies such as LCD and LED-LCD displays, resulting in more energy efficient displays.

1.1.2 The Importance of Solar Cells

In 2005 Nobel laureate Dr. Richard Smalley discussed what he coined the "Terawatt challenge"[17]. Smalley went onto say that in order to provide energy for 10 billion people in the world by 2050 that 60 terawatts of energy would need to produced or the equivalent of 900 million barrels of oil per day[17]. He called for the need of a "new oil" that was clean (little to no CO_2 emissions), cheap (pennies per watt), and abundant

[17]. Smalley suggested that solar power is the best sustainable energy source to meet the terawatt challenge[17] with an available resource of 125,000 terawatts per year[18].

To address the terawatt challenge Smalley suggested that photovoltaic devices need only achieve a 10% power conversion efficiency and placed in areas of high solar radiation[17]. Figure 1.3 presents reported power conversion efficiencies of solar cell technologies over time.

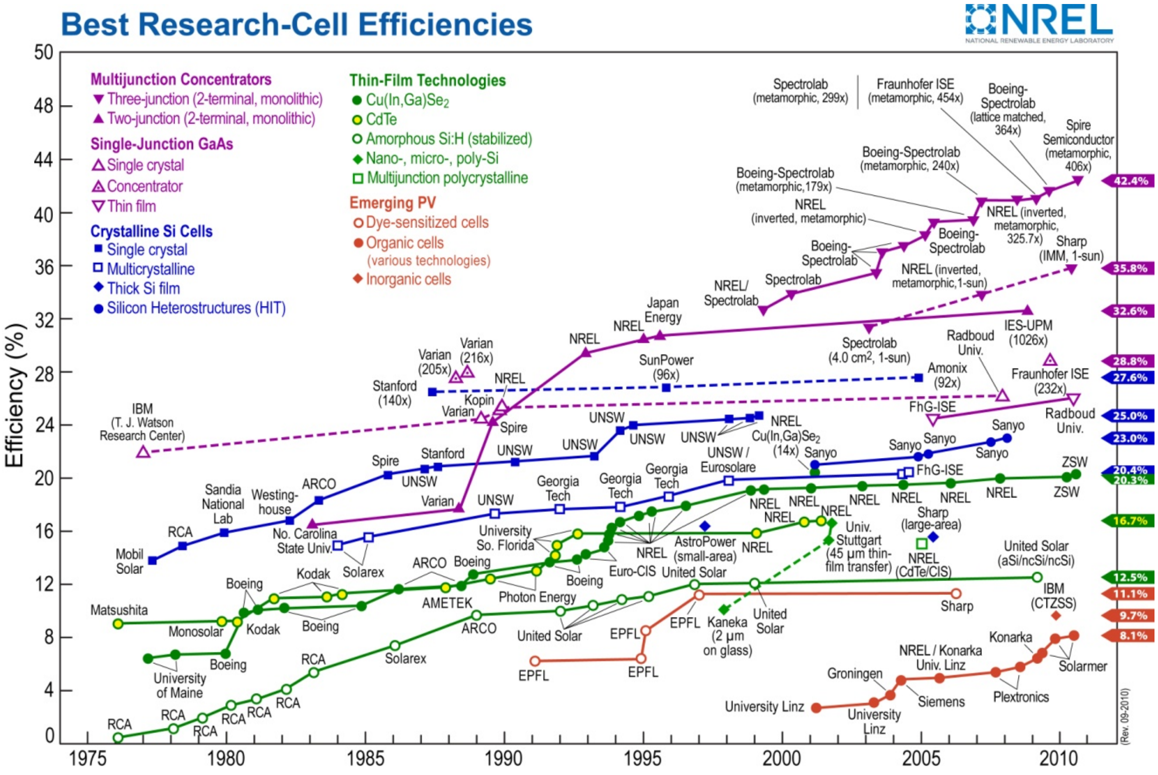

Figure 1.3 The progress of numerous solar cell technologies' efficiency over time. Taken from reference [19].

As can be seen in Figure 1.3 the technology to produce solar cells with 10% efficiency has already been realized. This makes solar cell technologies well suited to gather the required power to meet the terawatt challenge. However, the outstanding obstacle with solar technologies is cost. OPVs are advantageous in that they do not require costly high temperature vacuum processing, can be printed onto low cost and lightweight flexible substrates such as Poly(ethylene terephthalate) (PET). This allows OPVs to be manufactured at lower costs in the future through simpler manufacturing processing and less material utilization. Furthermore, OPV's lightweight and flexible structure allows them to be incorporated into wearable apparel, giving them the potential to be nearly ubiquitous in future societies. Moreover, organic photovoltaics have recently achieved power conversion efficiencies of 8.1%[19] with efficiencies expected to steadily increase with ongoing technological advancements. Therefore, OPVs are potential candidates to harness solar power to address the terawatt challenge by providing a means to obtain cheap, clean, and abundant energy.

1.1.3 Principles of Operation of Organic Optoelectronic Devices

In Figure 1.4 the typical architecture of an OLED is presented. In OLEDs, holes are injected into the transport layer through the positive electrode when a voltage is applied across it. Similarly, electrons are injected into the emissive layer through the negative electrode, when a voltage is applied. As the hole and electron drift to the transport and emissive heterojunction they combine to form an exciton that emits light in a process known as electroluminescence (EL), where thereafter light is emitted through the transparent positive electrode and transparent substrate.

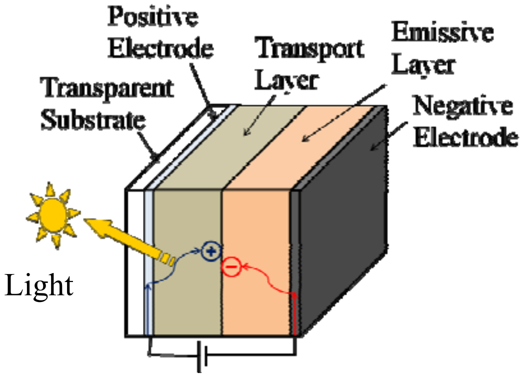

Figure 1.4 Typical organic light emitting diode architecture. Taken from reference [20].

A schematic of a typical architecture of an OPV is shown in Figure 1.5. In an OPV light in the form of photons enters the device, where it is transmitted through the transparent substrate and positive electrode. This photon is absorbed in the donor layer, where it generates an electron-hole pair, formally known as an exciton. This exciton is coulombically bound, a result of Coulomb's Law that states that opposite charges are attracted to each other, as it drifts to the acceptor/donor (A/D) heterojunction. When the exciton reaches the A/D heterojunction the exciton will dissociate, meaning that the electron and hole from the exciton are transferred to the acceptor and donor layer, respectively. This dissociation will only occur if the selected acceptor layer has an appropriate work function such that it would be energetically favorable for the exciton to dissociate[21]. After the exciton has successfully dissociated the electron and hole then diffuse to the negative and positive electrodes, respectively; where they are extracted for future power output [20].

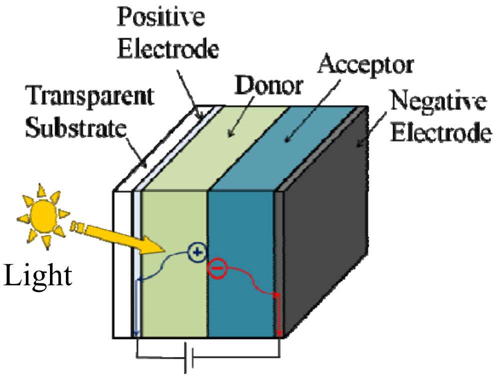

Figure 1.5 Typical organic photovoltaic architecture. Taken From Reference [20].

1.2 The Current Status of Transparent Conductive Oxides

Currently transparent electrodes for optoelectronic device are dominated by metal oxides where primarily indium tin oxide is the principal transparent electrode. Alternative metal oxide semiconductors include binary doped zinc oxide, binary doped tin oxide, and binary doped indium oxide films [22]. In Figure 1.6 the resistivities of zinc oxide, tin oxide, and indium oxide thin films over time are presented. Metal oxide semiconductors' electronic properties where initially quantified in literature in terms of resistivity as opposed to sheet resistance.

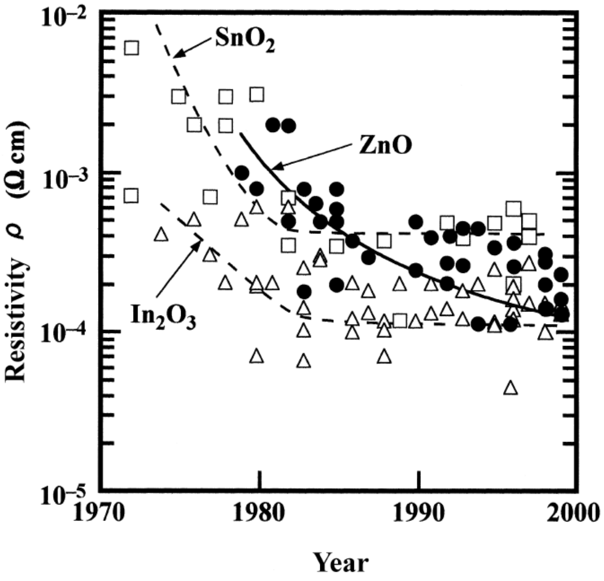

Figure 1.6 Reported resistivities of indium oxide, tin oxide, and zinc oxides thin film as transparent conducting oxides from 1970-2000. Taken from reference [22].

As can be seen in Figure 1.6 tin oxide films resistivity were generally too high to be implemented as transparent electrodes and indium oxides films suffered similar disadvantages as ITO, most notably where the principal material, indium, is expensive. Zinc oxide films offer competitive electronic properties, are more chemically stable, more abundant, and less expensive[10, 22]. Specifically aluminum zinc oxide has been shown to have comparable performance to ITO in OLEDs [23]. However, metal oxide semiconductors' inherent brittle nature makes them unsuitable for flexible organic optoelectronics. Furthermore, metal oxide semiconductors generally require high vacuum processing conditions which have high costs associated with, thereby reducing the feasibility of manufacturing lost cost optoelectronic devices.

1.3 Flexible Alternatives to Indium Tin Oxide

Flexible transparent conductive alternatives to ITO include conductive polymers such as PEDOT:PSS and carbon based nanomaterials including graphene and carbon nanotubes. PEDOT:PSS is advantageous over metal oxide semiconductors because it can be readily dispersed in water allowing for simpler manufacturing processes[24] to reduce costs for cheaper optoelectronic devices. However, PEDOT:PSS electronic properties are insufficient with state-of-the-art films exhibiting 350Ω/sq coupled with 80% optical transmittance compared to 10 Ω/sq with 80% transmittance for ITO.

Optically transparent carbon based nanomaterials (CBNs) including carbon nanotubes (CNTs) and graphene are promising candidates as transparent conductive electrodes (TCEs) due to their high electrical conductivity coupled with high optical transparency (see chapter 2), are robust materials that can be flexible several times with minimal deterioration in their electronic properties[5, 25-27], and can be solution processed with water.

In practice carbon nanotubes (CNTs) or single wall carbon nanotubes (SWNTs) are easily solution processed through the use of organic solvents or surfactants in DI water allowing SWNTs to be deposited onto transparent substrates through vacuum filtration[28], ultrasonic spray coating[29], dip coating[27], spin coating[30], and inkjet printing[31]. The ability to solution process SWNTs enables them to be deposited onto large areas at potentially lower costs than ITO through simpler manufacturing processes. Organic solvents that can disperse carbon nanotubes, most notably, N,N-dimethylformamide (DMF) and dimethyl pyrrolidone (NMP) [32], are highly flammable and toxic and thus dispersion of carbon nanotubes in water through the use of surfactants is generally preferred [20]. In Figure 1.7a and b SWNT powder and solution processed SWNT "ink" are presented, respectively.

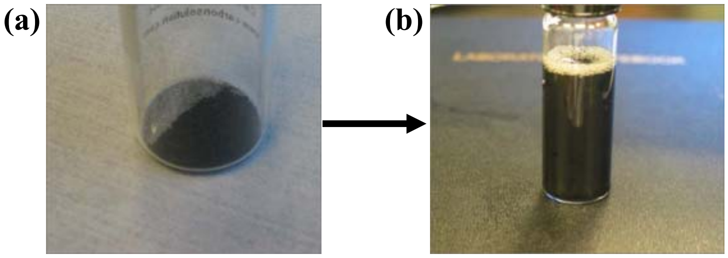

Figure 1.7 (a) P3-SWNT powder from Carbon Solutions. (b) Solution processed SWNT ink. Taken from reference [20].

Though surfactants are great for dispersing SWNTs, surfactants are electrically insulating, limit tube-to-tube contact, limit chemical doping, and increase optical absorption, thereby decreasing the overall performance of carbon based nanomaterial transparent electrodes. Fortunately, surfactants can be removed through nitric acid treatment and/or thermal treatment in an inert environment (e.g. argon). However, it needs to be determined how treatments to remove surfactants are connected to other electrical aspects; and if the removal of surfactants is beneficial or detrimental to SWNT electrodes. For this reason, the removal of surfactants through nitric acid treatment and annealing in inert argon environment are investigated in this work.

In practice large-area pristine graphene it is difficult to obtain and to deposit onto transparent substrates. Current techniques for synthesizing graphene include graphene oxide[33], exfoliated graphite via graphite intercalation compounds and thermal shock[34], density gradient ultracentrifuged graphene[35], and chemical vapor deposition grown graphene [36]. Currently as-synthesized graphene sheets are plagued by numerous defect sites that act as potential barriers that hinder charge transport. However, it has been recently shown that graphene SWNT composite electrodes can be used to dramatically improve the electrical performance of SWNT electrodes with minimal sacrifices in optical transmittances[25]. Therefore, large-area pristine graphene is not necessary to produce high performing transparent electrodes. As such carbon nanotube graphene composite transparent conductive electrodes are studied in this work as well.

1.4 Research Goals

Though carbon based nanomaterials are promising candidates as transparent electrodes, there are outstanding problems that need to be addressed before the fabrication of large scale (1cm^2) transparent electrodes that meet or exceed the minimum industry standard (MIS) of <100Ω/sq coupled with an optical transmittance >90% at a wavelength of 550 nm are realized. To this end, the goal of this thesis is to add to the fundamental understanding of the physics involved with the removal of surfactants for solution processed SWNT and graphene electrodes through thermal and chemical treatments, both at the nanoscale and at the macroscale; and to investigate the potential of graphene SWNT composites as high performing transparent electrodes. For carbon nanotube electrodes, solution processed arc discharge as-synthesized mixed SWNTs (~2/3 semiconducting and ~1/3 metallic), type-sorted metallic SWNTs, and type-sorted semiconducting SWNTs will be utilized for surfactant removal studies. For graphene electrodes, graphene oxide, ultracentrifuged graphene solutions, and chemical vapor deposition (CVD) grown graphene will be utilized. Graphene oxide and CVD grown graphene will be investigated with regards to their potential as viable sources of graphene for high performing large area composite transparent electrodes. In addition, carbon based nanomaterial electrodes will be characterized and analyzed with regards to their global and individual materials properties that comprise the nanotube and graphene networks.

The thesis format will be as follows: Chapter 2 will provide a literature review on carbon nanotube transparent electrodes, present the state of the art for CNT electrodes, and discuss relevant theory for electrical conduction in carbon nanotube electrodes. Chapter 3 will discuss the experimental methodology utilized in this work. Chapters 4-5 represent the research contribution from this work. Chapter 4 will investigate the removal of surfactants and the effects on the optoelectronic properties of SWNT electrodes. Chapter 5 will study carbon nanotube graphene composite electrodes and briefly present the state of the art in graphene and carbon nanotube graphene composites prior to presenting experimental results. Chapter 6 will discuss conclusions and future work. In particular:

- Chapter 4 will investigate the impact of surfactant removal on electrode performance at both the nanoscale and macroscale. The nanoscale impacts on electrode performance will be investigated through the use of conductive-tip atomic force microscopy measurements. At the macroscale the impact of surfactant removal on electrode performance will be investigated through the characterization of the optoelectronic properties (sheet resistance and optical transmittance). This chapter focuses on the impact of surfactant removal on single wall carbon nanotubes (SWNTs), with a slight deviation to investigate the removal of the surfactant sodium cholate with density gradient ultracentrifuged graphene.

- Chapter 5 will investigate the potential of graphene SWNT composite electrodes as high performing transparent electrodes. To this end, the optoelectronic properties and structural quality of as-made and annealed graphene oxide SWNT composites electrodes where characterized. Comparisons will be done with as-made and annealed SWNT electrodes to understand the individual effects on graphene oxide and SWNTs after thermal treatments at temperatures of 1000°C. Furthermore, the optoelectronic properties of a chemical vapor deposition grown graphene M-SWNT electrode will be characterized to investigate improvements in electrical performance associated with the composite electrode.
- Chapter 6 presents a summary of the research contributions, conclusions made, and discusses future work. Particularly, annealing studies of SWNTs in controlled oxygen environments are discussed as a potential method to simultaneously increase the optical transmittance, heal defects, and reduce the sheet resistance of metallic carbon nanotube electrodes.

CHAPTER 2 : ELECTRICAL CONDUCTION IN CARBON NANOTUBE TRANSPARENT ELECTRODES

2.1 Figures of Merit of Transparent Conductive Electrodes

There are two primary figures of merit used to characterize transparent electrodes, which include sheet resistance and optical transmittance at a wavelength of 550nm. A secondary figure of merit, specific for carbon nanotubes and graphene, is to evaluate the structural quality of carbon based nanomaterial transparent electrodes through the graphitic to defect intensity ratio (I_G/I_D) obtained from Raman spectroscopy.

2.1.1 Sheet Resistance and Optical Transmittance

The primary figures of merit, sheet resistance and transmittance are related to one another and for this reason they will be discussed jointly. For this discussion of sheet resistance (R_{sh}) and transmittance, the effects of chemical doping, removal of surfactants, healing of defects through thermal treatments, or the development of composite films is not yet considered.

To begin, the efficiency/efficacy of organic optoelectronic devices are heavily dependent on the ability of a transparent electrode to allow photons to be transmitted into/out of the device; and to simultaneously allow electrical current to conduct with minimal resistance to minimize resistive power losses[20]. The ability of a transparent electrode to allow photons to be transmitted through the device can be evaluated through optical transmittance measurements via UV-Vis-NIR spectroscopy; and the electrical resistance can be measured through the 2D sheet resistance via the transfer length method (TLM). For a rectangular sample the 2D sheet resistance is defined in equation 2.1, where R is the resistance between two contacts, of width, W, and at a length, L apart.

$$\boldsymbol{R}_{\mathbf{sh}} = \boldsymbol{R}\frac{\boldsymbol{W}}{\boldsymbol{L}} \tag{2.1}$$

In general to improve the electrical conductivity of thin film electrodes, it is necessary to increase the thickness to add percolative pathways through higher surface coverage, which consequently decreases the optical transparency of the film[20]. This behavior is illustrated in Figure 2.1 for mixed CNTs, where the sheet resistance in Ω/sq is plotted versus optical transparency at 520nm and the film thickness is given for selected points.

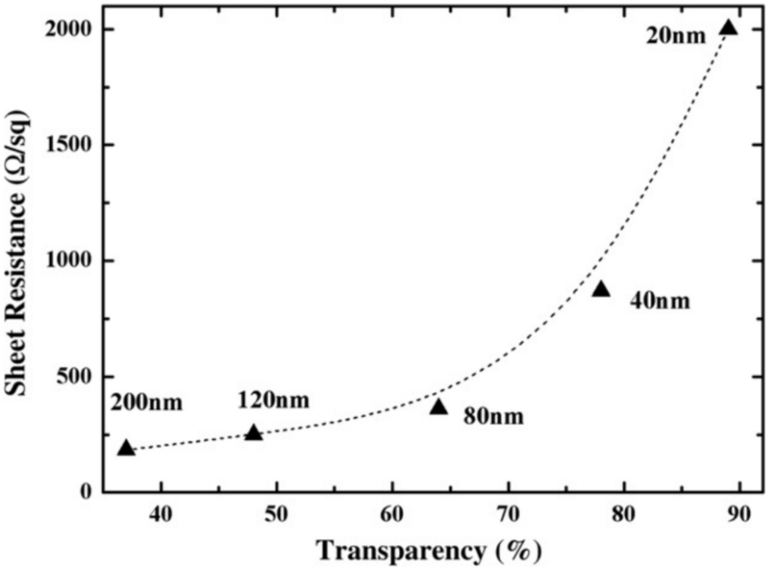

Figure 2.1 Correlation between mixed carbon nanotube electrode transparency (represented by the transmittance at 520nm) and sheet resistance. The line is only a guide to the eye. Taken from reference [37].

Referring to Figure 2.1 it is clear that as the optical transparency decreases the sheet resistance decreases as well. However, it is also apparent that the R_{sh} decreases at a lower rate as the films gets progressively darker, thus resulting in a tradeoff between R_{sh} and optical transmittance. The decrease in R_{sh} can be understood through percolation theory, where percolation in this context refers to the ability of a charge to conduct from one point to another. When there are insufficient conduction pathways or the so called "breaks" in the nanotube network (NTN), a potential barrier is formed. The potential barriers present from breaks in the NTN can be thought of as a resistance, as it reduces the energy of charged particles which in turn decreases the electrical conductivity of the

NTN. When a NTN has enough percolative paths for charges to travel through, it is said to have reached the percolation threshold[38]. This concept is illustrated in Figure 2.2, where in (a) the NTN has not reached the percolation threshold, (b) the NTN has reached the percolation threshold, and (c) the NTN is well above the percolation threshold.

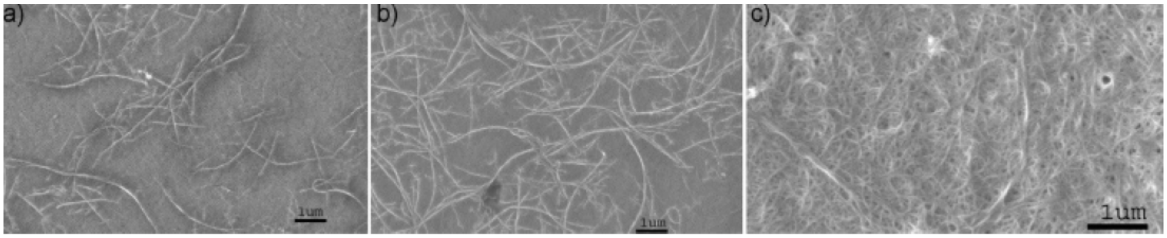

Figure 2.2 (a) SWNT network below the percolation with insufficient percolative conduction pathways. (b) SWNT network that has reached the percolation threshold. (c) SWNT network well above the percolation threshold, providing several percolation pathways. Taken from reference [38].

Due to the percolative nature of NTNs as was discussed above, R_{sh} varies inversely with surface film density. Furthermore, it is obvious that surface film density is directly proportional to film thickness. Therefore, it is expected for sheet resistance to vary inversely with film thickness. There is a rapid decrease in R_{sh} when increasing the film thicknesses from a highly optical transparent electrode, because of an increase in percolative pathways. After the percolation threshold has been reached there is a rapid decay in R_{sh} that eventually reaches a saturation point, as is apparent in Figure 2.1.

Per the above discussion, it should be noted that a direct comparison of R_{sh} at two different optical transmittances cannot be made and that it is important to always consider both sheet resistance and transparency when reading literature. For example, indium tin oxide has a R_{sh} of 100Ω/sq at 90% T and has a R_{sh} of 10Ω/sq at 80%T. This corresponds to a reduction in R_{sh} by a factor of 10 by simply reducing the optical transmittance. By comparison in Figure 2.1 a mixed CNT film produced by E. Koudoumas et al. only has a decrease in R_{sh} by a factor of ~2, when reducing the optical transmittance from 90% to 80%. Therefore, it is important to note that the rate at which the R_{sh} decreases as a function of transmittance varies depending on the material and its optical properties. In this case, CNTs and graphene are highly absorbing in the visible range with CNT films of 50nm have transmittances >70%[28] and graphene decreasing the transmittance by ~2.0% for every layer of graphene added (see chapter 5, Figure 5.10). Therefore, only a few layers of CNTs and graphene are necessary to drop the optical transmittance when compared to transparent conductive oxides like ITO that has ~93%T at 100nm film thickness[39].

Fortunately, it turns out that the transmittance can be related to R_{sh} through equation 2.2 [38] , where Z_0 is the impedance of free space, μ_0 is the permeability of free space, ϵ_o is the permittivity of free space, σ_{Op} is the optical conductivity, and σ_{DC} is the direct current conductivity. Equation 2.2 can be solved to determine the conductivity ratio as shown in equation 2.2. The conductivity ratio, $\sigma_{\mathrm{Op}}/\sigma_{\mathrm{DC}}$, is useful to quantify the optoelectronic properties of transparent electrodes. As a general rule of thumb a higher conductivity ratio corresponds to better optoelectronic properties.

$$\boldsymbol{T}=\left(1+\frac{\boldsymbol{Z_0}}{2\boldsymbol{R}_{\mathbf{sh}}}\frac{\boldsymbol{\sigma}_{\mathbf{Op}}}{\boldsymbol{\sigma}_{\mathbf{DC}}}\right)^{-2};\ \boldsymbol{Z_0}=\sqrt{\frac{\boldsymbol{\mu}_0}{\in_0}} \tag{2.2}$$

$$\frac{\boldsymbol{\sigma}_{\mathbf{DC}}}{\boldsymbol{\sigma}_{\mathbf{Op}}}=\frac{\boldsymbol{Z_0}}{2\boldsymbol{R}_{\mathbf{sh}}\left(\boldsymbol{T}^{-1/2}-1\right)} \tag{2.3}$$

2.1.2 Graphitic to Defect Intensity Ratio via Raman Spectroscopy

In CNTs and graphene there are three significant scattering modes that are present in the Raman spectrum including the D-band, G-band, 2D/G$^{'}$-band as is shown in Figure 2.3. These scattering modes generally appear at approximate wavenumber or Raman shift positions, but can and do vary slightly from sample to sample. The peak position also depends on the laser wavelength.

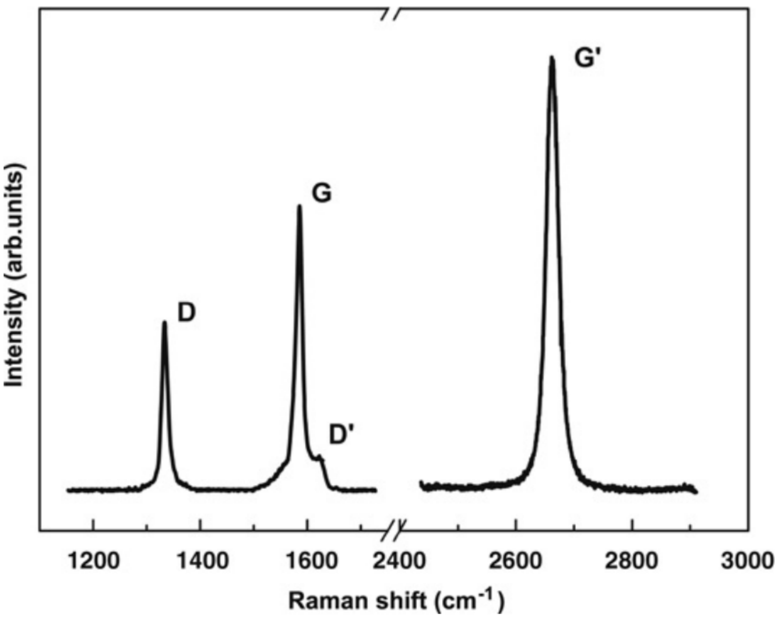

Figure 2.3 Raman spectra of graphene presenting the main intensity peaks, which include the D-band, the G-band, and the G'-band (commonly referred to as 2D-band). The laser excitation energy is 2.41eV, which corresponds to a laser wavelength of 514nm. Taken from reference [40].

The D-band occurs at ~1350 cm^{-1} and is generated from the scattering modes of structural defects in graphene. Therefore the higher the intensity of the D-band the more defects that are present. The G-band occurs at ~1585 cm^{-1} and is commonly referred to as the graphitic peak because this scattering mode is present in most carbon-based materials. Therefore, the ratio of the intensity of the G-band and D-band (I_G/I_D) is used to quantify the structural quality of graphene and CNTs. The last significant scattering band is the 2D-band, it is also commonly referred to as G'-band. The 2D-band is the second overtone of the defect band that occurs ~2720 cm^{-1} through a double resonance scattering process[41]. The 2D-band is useful to distinguish between the presences of graphene from that of graphite. In graphite there is a shoulder that is present at ~2698 cm^{-1} and for graphene the shoulder is not present (See Figure 3.19 in Chapter 3).

2.2 Single Wall Carbon Nanotube Solution Processing

Carbon nanotubes are primarily synthesized through the arc-discharge, laser-ablation, chemical vapor deposition (CVD), and high pressure carbon monoxide (HiPCO) methods. Typical batches of synthesized nanotubes are ~2/3 semiconducting and ~1/3 metallic and as such CNT films that have not been type sorted are referred to as mixed CNTs/SWNTs in this thesis. After the carbon nanotubes have been synthesized, they are then dispersed in a solvent, typically water, through the use of surfactants such as, sodium dodecyl sulfate (SDS) and sodium cholate (SC) with the aid of bath and/or probe sonication. This resulting carbon nanotube solution is often referred to as CNT ink.

The CNT ink is then used to produce optically transparent electrically conductive thin films through spin-coating, spray-coating, vacuum filtration, or ink-jet printing. The details of the SWNT solution fabrication are discussed more thoroughly in this section. However, each of the four CNT synthesizing methods produces CNTs with different tube diameters, tube lengths, CNT bundle diameters, and number of nanotube shells[42]. As a result the four synthesis methods have variations in the quality of nanotubes produced. Therefore it is important to understand which synthesis method produces the best quality CNTs.

Geng et al. used carbon nanotubes powders synthesized through the four main methods to evaluate the differences in the quality of the CNTs produced through each method. These CNT powders were dispersed in DI water with SDS and were subsequently spray coated onto PET films. The CNT films produced were characterized through sheet resistance and optical transmittance at a wavelength of 550nm. Geng et al. demonstrated that the arc discharge method is superior as is shown in Figure 2.4 [43]. Therefore only arc-discharge grown CNTs will be used and discussed in this work.

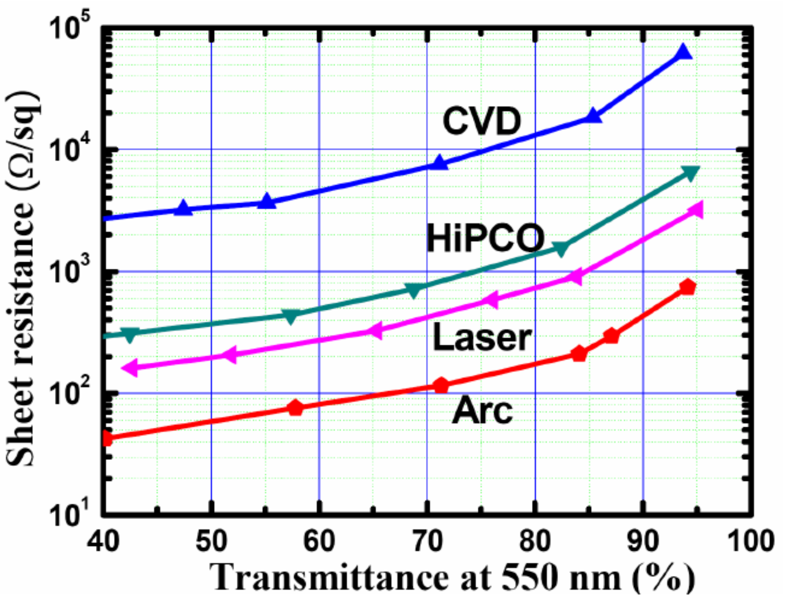

Figure 2.4 Sheet resistance as a function of transmittance for spray coated CNTs produced through the four main synthesis methods. Taken from reference [43].

2.2.1 Arc-Discharge Synthesized Carbon Nanotubes

In 1991 S. Iijima first synthesized carbon nanotubes through the use of the arc-discharge method, where he produced multi-walled carbon nanotubes ranging from 2 to 50 walls [44]. A schematic of the arc discharge method is shown in Figure 2.5. The arc-discharge method is performed in a reaction vessel that is filled with an inert gas, such as helium or argon, at a controlled pressure ranging from 100-500 torr [45]. Two graphitic rods are then placed inside the vessel were the smaller rod serves as the anode and the larger rod serves as the cathode. A potential is then applied across the graphitic rods and as the rods are pushed closer together to a distance of ~1mm, a current of ~100A passes through the rods creating a discharge that forms a plasma[45].

As the anode is vaporized by the plasma, carbon nanotubes along with amorphous carbon, C_{60}, and other graphitic nanoparticles are deposited on the cathode. Single wall carbon nanotubes (SWNTs) can be grown through the arc discharge method by boring a hole in the anode and filling it with pure powdered metals (Fe, Ni, or Co) and Graphite [46]. After the synthesis is done, the amorphous carbon, C_{60}, graphitic nanoparticles, and residual catalyst are removed through a purification process, typically involving acid treatments with nitric and sulfuric acid.

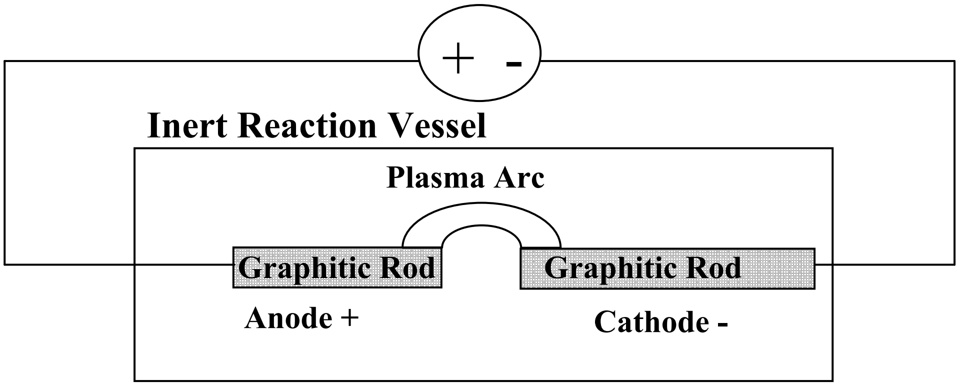

Figure 2.5 Schematic of Arc-Discharge Evaporation method to produce CNTs.

2.2.2 Dispersion of Carbon Nanotubes in Solution via Surfactants

Due to their chemical structure, pristine carbon nanotubes are non-polar and do not readily disperse in aqueous solutions. Furthermore, carbon nanotubes have a high affinity for each other, which makes it difficult to disperse them as individual tubes [47]. However, through bath and/or probe sonication carbon nanotubes can be dispersed through the use of organic solvents or through surfactants in aqueous solutions. Organic solvents that can disperse carbon nanotubes, most notably, N,N-dimethylformamide (DMF) and dimethyl pyrrolidone (NMP) [32], are highly flammable and toxic and thus dispersion of carbon nanotubes in water through the use of surfactants is generally preferred [20].

Typical surfactants that are used to disperse CNTs include sodium dodecyl sulfate (SDS)[48], sodium dodecylbenzene sulfonate (SDBS)[49], sodium cholate (SC)[50], and sodium carboxymethyl cellulose (CMC)[29]. CMC is typically used to fabricate CNT films through the use of the ultrasonic spray coating technique[29]. In this work, successful dispersion of SWNTs has been achieved through the use of SDS, SDBS, and SC, which are all anionic surfactants [51]. However, the vast majority of this work has used carbon nanotubes solutions dispersed through the use of SDS and SC. The surfactants SDS and SC were studied in particular because they are essential to type sort SWNTs by electronic type using the density gradient ultracentrifugation technique. SWNT solutions of homogenous electronic type are essential to realize the full potential of nanotube electrodes; as will be discussed later in this chapter. The chemical structure of SDS, SDBS, and SC are shown in Figure 2.6.

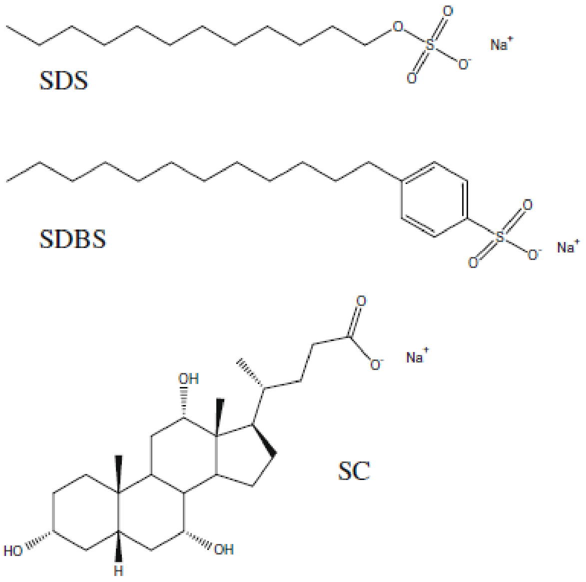

Figure 2.6 Chemical Structure of surfactants sodium dodecyl sulfate (SDS), sodium dodecylbenzene sulfonate (SDBS), and sodium cholate (SC). Adapted from reference[51].

Surfactants are generally organic amphiphilic compounds, which are compounds that have a hydrophobic tail and a hydrophilic head. Where the hydrophobic tail adsorbs on to the surface of the hydrophobic CNT and the hydrophilic head mixes with water to effectively disperse the CNTs with the aid of bath and/or probe sonication. The hydrophobic tail is generally neutral and the hydrophilic head may have a charge. In the case of the SDS, SDBS, and SC, the charge of the hydrophilic head can be determined by referring to the chemical structure of each compound in Figure 2.12. In each compound the Na$^+$ atom is attached to an O^{2-} atom, resulting in a net negative charge, thus the term anionic surfactants. The significance of this net negative charge is that it provides electrostatic repulsion in the carbon nanotubes and thereby counteracts the tendency of

CNTs to aggregate[47]. This allows these surfactants to provide SWNT solutions that are stable for time frames on the order of months. However, despite the solutions being stable the nanotubes will still aggregate with time which eventually leads to increases in nanotube bundle diameter. The larger nanotube bundle diameters negatively impacts the conductivity of SWNT electrodes.

Although surfactants are great for dispersing nanotubes, they are not easily removed from the nanotube electrodes. This is undesirable because surfactants are electrically insulating, limit chemical doping, and increase optical absorption thereby decreasing overall performance of TCE films. Methods to remove surfactants and the effects it has on SWNTs and graphene will be discussed thoroughly in Chapter 4.

2.2.3 State of the Art Mixed Carbon Nanotube Electrode Films

Using carbon based nanomaterials (CBNs) as transparent electrodes began with mixed SWNTs that consisted of batches of ~2/3 semiconducting and ~1/3 metallic nanotubes. Wu et al. first reported in 2004 a nitric acid treated mixed SWNT transparent electrode produced through the vacuum filtration method with a R_{sh} of 30Ω/sq with 70% optical transmittance in the visible range; this represents the state of the art for mixed SWNT films. Geng et al. reported in 2007 sheet resistances of ~40 Ω/sq and 70 Ω/sq at 70% and 80% transmittances, respectively[42]. Geng et al. also reported the performance of mixed CNT as-prepared and acid-treated films as a function of film thickness. The findings of Geng et al. along with reported values prior 2007 are plotted in Figure 2.7[42]. Geng et al. attribute the exceptional optoelectronic properties of the mixed SWNT electrodes to removal of surfactant as was demonstrated in their XPS scans and to densification of the films creating an increase in nanotube contacts [42].

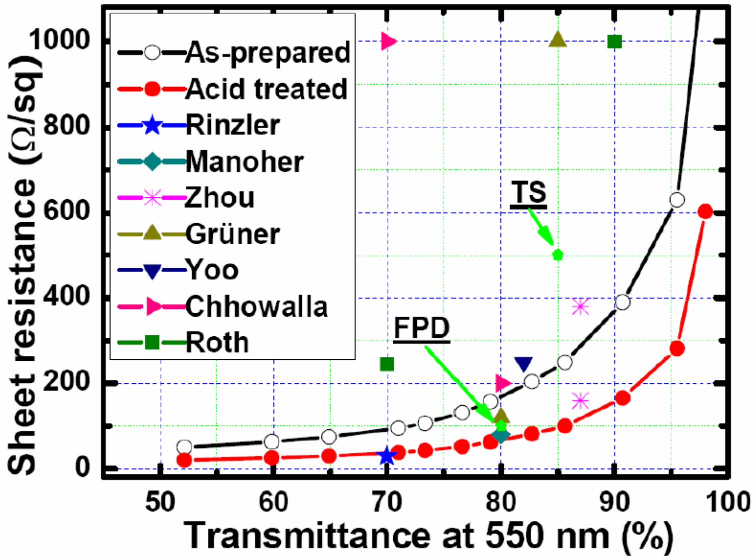

Figure 2.7 Previously reported values of sheet resistances of Mixed CNTs as a function of transmittance at 550nm. Geng et al. study for as-prepared and acid treated mixed CNTs for comparison. Requirements for touch screen (TS) and flat panel display (FPD) technologies are plotted as well. Taken from reference [42].

It is pointed out that Chhowalla [52, 53] and Grüner [38, 54] used two probe methods. While Geng et al. [42], Roth [55, 56], Rinzler [28], Yoo [57], Manohar [26], and Zhou [58] used four-point probe methods. While not invalidating their results, the two and four point probe measurement techniques are far less reliable and reproducible than the transfer length method (TLM). The details of the two probe, four-point probe can be found in appendix B; and the transfer length method will be discussed in Chapter 3.

In 2008, Jackson et al. using the TLM reported a value of 105Ω/sq with 80%T at 550nm for a mixed SWNT film that was doped with HNO_3 and subsequently doped with $SOCl_2$ [59]. Though the optoelectronic properties reported by Jackson et al. are less conductive than 70Ω/sq it is likely a more accurate measure of the state of the art for mixed CNT films, due to the use of a more reliable TLM measurement technique.

2.3 Type Sorted Carbon Nanotubes

To fully realize the electrical properties of carbon nanotubes, homogeneous CNT batches of one electronic type (i.e. metallic or semiconducting) are needed as Schottky barriers form at metallic-semiconducting nanotube heterojunctions. These Schottky barriers make it difficult for charges to conduct in nanotube networks and as a result the electrical performance, specifically sheet resistance, is negatively impacted. As synthesized carbon nanotubes are ~1/3 metallic and ~2/3 semiconducting; and methods to synthesize nanotubes of one electronic type have not yet been realized. As such intense research has been done in type sorting SWNTs including separation techniques such as selective destruction[60], selective chemistry[61], and density gradient ultracentrifugation[62]. Currently the most promising technique is density gradient ultracentrifugation (DGUC) and type sorted nanotubes are commercially available through the company Nanointegris.

By using combinations of the surfactants sodium dodecyl sulfate and sodium cholate SWNTs can be optimally sorted through the use of density gradients by exploiting differences in the mass per volume buoyant densities of SWNTs of different structures [62, 63]. As the nanotubes are ultracentrifuged, the centripetal forces cause the nanotubes to sediment to their respective buoyant densities. This process is illustrated in Figure 2.8

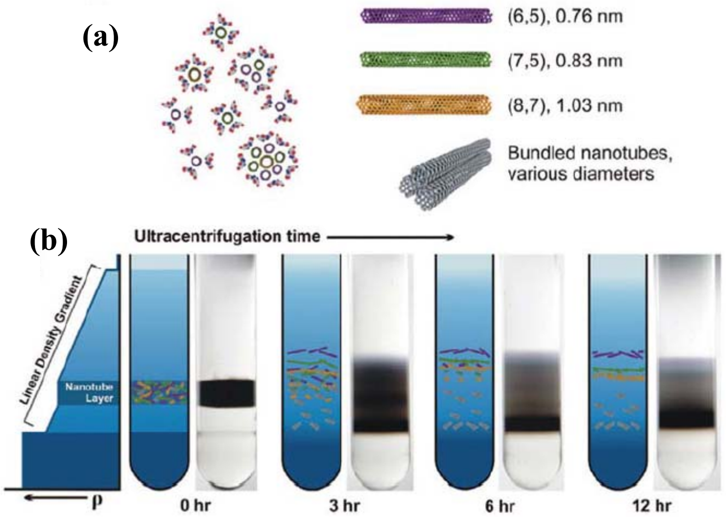

Figure 2.8 (a) Schematic of surfactant-encapsulated SWNTs. The chiral vector and diameters of three specific SWNTs are identified. (b) Schematics and photographs of an ultracentrifuge tube at four points in the DGU process. Taken from reference [63].

2.3.1 State of the Art Metallic and Semiconducting Nanotube Electrodes

Green et al. type sorted high pressure carbon monoxide (HiPCO) SWNTs and compared the optoelectronic properties of M-SWNT vs. unsorted SWNT in the visible and infrared ranges. The results of Green et al. are presented in Figure 2.9, where type sorted M-SWNTs showed an improvement in the inverse of the conductivity ratios, $\sigma_{\mathrm{OP}}/\sigma_{\mathrm{DC}}$, by factors in excess of 5.6 in the visible range and up to 10 in the infrared range[64]. Recently, Lu et al. reported a R_{sh} less than 100Ω/sq with 80% T at 550nm for arc-discharge type sorted M-SWNT [65].

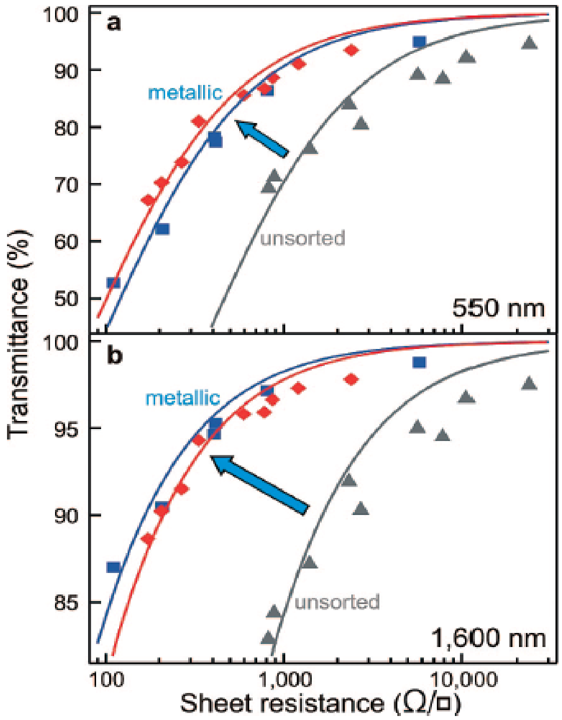

Figure 2.9 Comparison of optoelectronic properties of HiPCO sorted M-SWNT vs unsorted material SWNT in the visible and infrared range. Red diamonds and blue squares correspond to M-SWNTs with principal diameters of 0.9nm and 1.0nm, respectively. Taken from reference [64].

M-SWNTs are intuitively thought to have superior optoelectronic properties than Sc-SWNTs. However, Blackburn et al. reported values of 920Ω/sq and 180 Ω/sq for thionyl chloride doped 94% metallic and 94% semiconducting SWNTs films. The average transmittance was calculated for the range of 400nm-2000nm resulting in 80%T and 76%T for M-SWNT and Sc-SWNT, respectively[66]. Jackson et al. confirmed the results of Blackburn et al. by demonstrating a R_{sh} of 76 Ω/sq and 60 Ω/sq for M-SWNT and Sc-SWNT films, respectively, with 70% transmittances at 550nm [67].

The superior performance of highly doped Sc-SWNTs over M-SWNTs can be understood through the density of states for M-SWNT and Sc-SWNT (See Appendix A, Figure A.6). Hole doping with HNO_3 and $SOCl_2$ effectively shifts the Fermi-level in the valence band for Sc-SWNTs below the second van hove singularity(S_{22}), but only shifts the Fermi level just above the first van hove singularity (M_{11}) for M-SWNTs [66, 67].

The significance of this shift is that there is a larger density of electronic states near the Fermi level in the valence band for Sc-SWNT than M-SWNT. This concept is illustrated in Figure 2.10

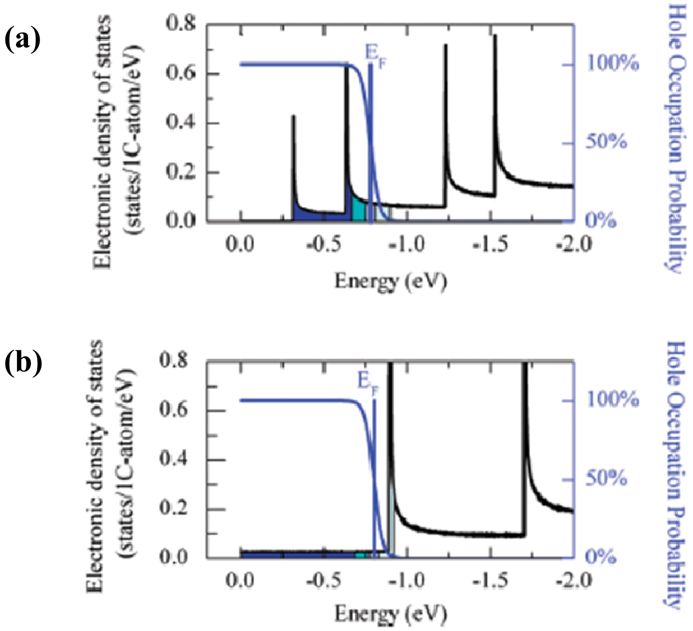

Figure 2.10 (a) (11,10) Sc-SWNT DOS after being doped with HNO_3 and $SOCl_2$. (b) (10,10) M-SWNT DOS after being doped with HNO_3 and $SOCl_2$. Taken from reference [67].

2.4 Doping of Carbon Nanotubes

Jackson et al. showed that CNTs can be optimally p-doped through intercalation and nucleophillic substitution of carboxylic acids with acyl chlorides via nitric acid and thionyl chloride treatment, respectively[59]. P-doping through intercalation and nucleophillic substitution of carboxylic acids with acyl chlorides is discussed in more detail below.

2.4.1 Doping through Intercalation via Nitric Acid Treatment

Bower et al. found an expansion in the inter-nanotube spacing by 1.85Å through the use of X-ray diffraction and nuclear magnetic resonance spectroscopy, which strongly suggests intercalation of the HNO_3 molecules in the SWNT bundles [68]. Furthermore, Bower et al. demonstrated that a HNO_3 molecule can easily nest in between SWNTs in their "Simple space filling model of the SWNT unit cell", as shown in Figure 2.11 [68]. Doping through intercalation has been shown to p-dope SWNT by effectively shifting the Fermi level downwards [69].

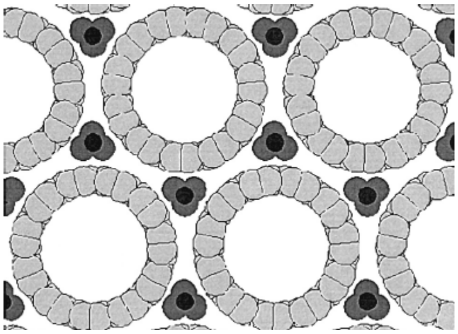

Figure 2.11 A simple space filling model of the SWNT unit cell, where an HNO_3 molecule can easily nest in between nanotubes at interstitial sites. Taken from reference [68]

2.4.2 Doping through Nucleophillic Substitution

Carbon nanotubes used in this work are bought from Carbon Solutions for mixed SWNTs and from Nanointegris for type sorted SWNTs. The nanotubes that are bought are functionalized with carboxylic acids at the tips of the CNTs and at defects sites through the use of strong oxidizing acids such as H_2SO_4 [70]. Jackson et al. used thionyl chloride ($SOCl_2$) to p-dope carbon nanotubes through nucleophillic substitution of carboxylic acid groups with acyl chlorides [59]. Nucleophillic substitution occurs since the acyl chlorides have an electronegativity of 3.16 which is higher than the electronegativity of the hydroxyl group which is 2.75. The process of nucleophillic substitution is shown in Figure 2.12. The more electronegative chlorine pulls more electrons than the hydroxyl group does, because it is more electronegative and as a result the CNT is hole-doped from the loss of the electrons in the valence band. This effectively shifts the Fermi level down. It is also possible to p-dope a CNTs even further through

Nucleophillic substitution by using a more electronegative chemical such as Fluorine with an electronegativity of 3.98.

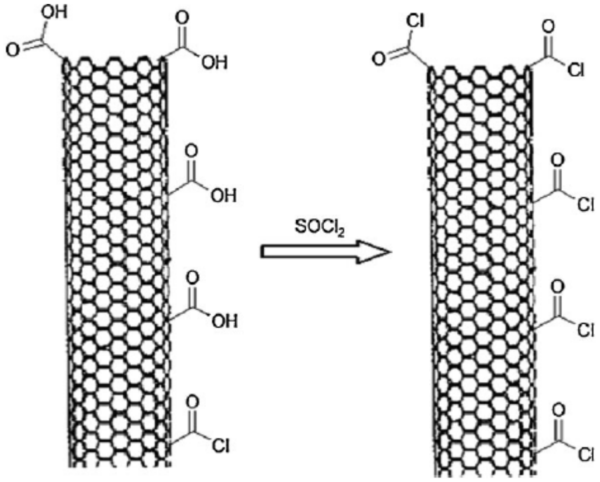

Figure 2.12 Nucleophillic substitution of carboxylic acid groups on the sidewalls and tips of the SWNT with acyl chlorides via chemical treatment with $SOCl_2$. Taken from reference [59].

2.5 Optoelectronic Properties of Carbon Based Nanomaterials

The figures of merit utilized to characterize transparent electrodes have been discussed, as well as how SWNTs are synthesized, solution processed, and doped. Moreover, the state-of-the-art carbon nanotube electrodes were presented as well. It is now of interest to understand how the material properties of carbon nanotubes (and graphene) contribute to their electronic performance. Then the next section will expand upon this knowledge and discuss electrical conduction in nanotube networks.

Graphene is a one-atom thick sheet of sp^2 bonded carbon atoms arranged in a honeycomb lattice structure[71, 72] and is the basic structural element for carbon allotropes including buckyballs[73], carbon nanotubes[44], and graphite[74] as is shown in Figure 2.13. Graphene and single walled carbon nanotubes (SWNTs) have been the topic of intense research, because of their remarkable electronic, optical, mechanical, and thermal properties[75]. Of these, the electronic properties have received the most attention with application towards next generation field effect transistors[76], RF devices[77], sensors[78, 79], and transparent electrodes[28].

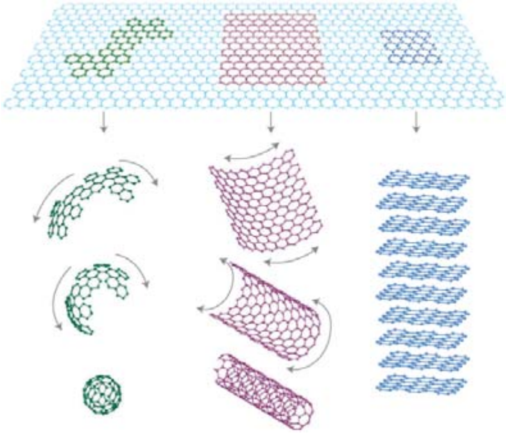

Figure 2.13 Graphene and its allotropes, including buckyballs, carbon nanotubes, and graphite. Taken from reference [74].

The electronic properties of graphene sheet and SWNTs, most notably include a mobility of charge carriers of ~200,000cm^{2}V^{-1}s^{-1} [80] and ~100,000cm^{2}V^{-1}s^{-1} [81], respectively. The carrier mobilities of common semiconductors include silicon with 1400cm^{2}V^{-1}s^{-1} and 480cm^{2}V^{-1}s^{-1} electron and hole mobilities, respectively[82]; Germanium at 3800cm^{2}V^{-1}s^{-1} and 1820cm^{2}V^{-1}s^{-1} electron and hole mobilities, respectively[83]; Gallium Arsenide with carrier mobilities of 7000-10,000cm^{2}V^{-1}s^{-1}[84]. Therefore, the charge carrier mobilities of graphene and SWNTs are relatively high.

The significance of the mobility of charge carriers, μ, is that it has a direct impact on the direct current conductivity, σ_{DC}. For n-doped graphene and SWNTs transparent electrodes σ_{DC} is determined by equation 2.4, where n is the charge carrier density, and e is the electron charge.

$$\boldsymbol{\sigma_{DC} = ne\mu} \tag{2.4}$$

To maximize the conductivity, the three individual components contributions to σ_{DC} are discussed. First, the electron charge is a universal constant that is common for all materials, the mobility of charge carriers is an intrinsic property of a material, and the charge carrier density can be increased via hole doping for graphene[2] and SWNTs [85].

Therefore, considering that the charge carrier density can be controlled via hole-doping (typically achieved via chemical doping) and that electron charge is constant, obtaining a material with the highest mobility of charge carriers is desirable to maximize electrical conductivity. However, chemical doping is not without its consequences as it introduces defects and thereby dramatically reduces the charge carrier mobility. As such a balance between the positive and negative aspects of doping need to be considered when discussing charge carrier mobility. Nonetheless, if care is taken high charge carrier mobilities are attainable[2]. Furthermore, the charge carrier mobility can be related to the primary figure of merit sheet resistance by considering the definition of R_{sh} as presented in equation 2.5, where ρ is the resistivity and t is the film thickness. Recalling that the σ_{DC} , is simply $1/\rho$, equation 2.5 can be rewritten to yield equation 2.6. Substitution of equation 2.4 into equation 2.6 yields equation 2.7. Therefore it is seen that the charge carrier mobility is inversely proportional to the sheet resistance. Thus, the relatively high mobility of charge carriers for graphene and SWNTs make it an attractive material for transparent electrode applications.

$$\boldsymbol{R_{\mathrm{sh}} = \frac{\rho}{t}} \tag{2.5}$$

$$\boldsymbol{R_{\mathrm{sh}} = \left(\sigma_{\mathrm{DC}} t\right)^{-1}} \tag{2.6}$$

$$\boldsymbol{R_{\mathrm{sh}} = \left(n e \mu\, t\right)^{-1}} \tag{2.7}$$

The electronic properties of carbon based nanomaterials have been considered, but in order for CBNs to qualify as viable transparent electrodes, their optical properties must be considered as well. The transmittance, T, of a thin film can be related by the optical conductivity, σ_{Op}, just as R_{sh} can be related to σ_{DC}, as is shown in equation 2.8 [2, 38]. Where the impedance of free space, Z_0, is related to the permeability of free space, μ_0, and the permittivity of free space, $\in_0$ as is also presented in equation 2.8. Combining equations 2.6 and 2.8 yields equation 2.9, where a figure of merit, the conductivity ratio

σ_{DC}/σ_{Op}, arises that correlates the transmittance and the sheet resistance. Equation 2.9 can be solved for in terms of the conductivity ratio as was presented in equation 2.3.

$$\boldsymbol{T} = \left(1 + \frac{\boldsymbol{Z_0}}{2\boldsymbol{R}_{\mathbf{sh}}}\boldsymbol{\sigma}_{\mathbf{Op}}\boldsymbol{t}\right)^{-2}; \boldsymbol{Z_0} = \sqrt{\frac{\boldsymbol{\mu_0}}{\in_0}} \tag{2.8}$$

$$\boldsymbol{T} = \left(1 + \frac{\boldsymbol{Z_0}}{2\boldsymbol{R}_{\mathbf{sh}}}\frac{\boldsymbol{\sigma}_{\mathbf{Op}}}{\boldsymbol{\sigma}_{\mathbf{DC}}}\right)^{-2} \tag{2.9}$$

The conductivity ratio is an overall evaluation of the optoelectronic properties of CBN electrodes and higher conductivity ratios represent better optoelectronic properties. The minimum industry standard presented in chapter 1, R_{sh} of 100Ω/sq coupled with 90% optical transparency, can be expressed as a conductivity ratio of ~35. At this point it is seen that the electronic properties of graphene (μ) are favorable over those of SWNTs. However, SWNTs have a maximum obtainable conductivity ratio of ~35, whereas graphene's as-made conductivity ratio is ~11[2]. This discrepancy can be understood by comparing the optical properties (i.e. σ_{Op}) of graphene and SWNTs, where the optical conductivities are 1.8 x 10^5 S/m [2] and 1.7 x 10^4 S/m [2], respectively. Graphene's high optical conductivity is the reason for its lower as-made conductivity ratio of ~11 than SWNTs. Though SWNTs have been shown to meet the minimum industry for transparent electrode adoption, it is far short of the more stringent optoelectronic properties required for flat panel display (R_{sh} of 10Ω/sq coupled with 85%T) corresponding to a conductivity ratio of 220[2]. However, De et al. showed that theoretically, highly doped graphene can have a conductivity ratio as high as 330, which is high enough for most transparent electrode applications [2].Therefore, the remarkable electronic properties of graphene and SWNTs allow these carbon based nanomaterials to be engineered as high performing transparent electrodes that in the future may meet or exceed the minimum industry standard and the more stringent standard for flat panel displays.

2.6 Interparticle and Intraparticle Resistances

The goal of this section is to give a brief introduction to the competing effects between interparticle resistances associated with the removal of insulating surfactants that effectively improve electrical conductivity; and the intraparticle resistances associated with the removal of surface function groups through thermal annealing that effectively degrade electrical conductivity. The total sum of the intraparticle and interparticle interactions gives rise to the global 2-dimensional sheet resistances, which are heavily utilized in this thesis to characterize electrical performance of electrodes. The concept of interparticle and intraparticle resistances is particularly useful for solution deposited carbon based nanomaterials (CBNs), which result in a morphology of randomly oriented conductive networks. It should be noted that in this work that solution processed CBN electrodes were vacuum filtered, this technique is discussed in section 3.3.

2.6.1 Interparticle Resistances of Carbon Nanotubes

Individual carbon nanotubes (CNTs) in solution processed CNT electrodes can be thought of as 1-dimensional “conducting sticks”[38] that form randomly oriented conductive networks, where contacts between tubes may or may not exist. In reality the nanotubes seen in scanning electron microscopy (SEM) or atomic force microscopy (AFM) images are nanotube bundles due to the individual nanotubes having high affinity for one another[47]. For simplicity any references made to nanotubes in a nanotube network in this thesis is referring to nanotube bundles.

Shown in Figure 2.14a is a picture of a vacuum filtered SWNT film. A zoomed SEM image of a nanotube network is shown in Figure 2.14b. It can be imagined that as the charge carrier conducts through the nanotube network it has an infinite number of pathways to conduct through. This concept is illustrated in Figure 2.14c. For example, a charge carrier starting at point A, is not limited to but for simplicity, can reach point B through either of the outlined paths 1 or 2.

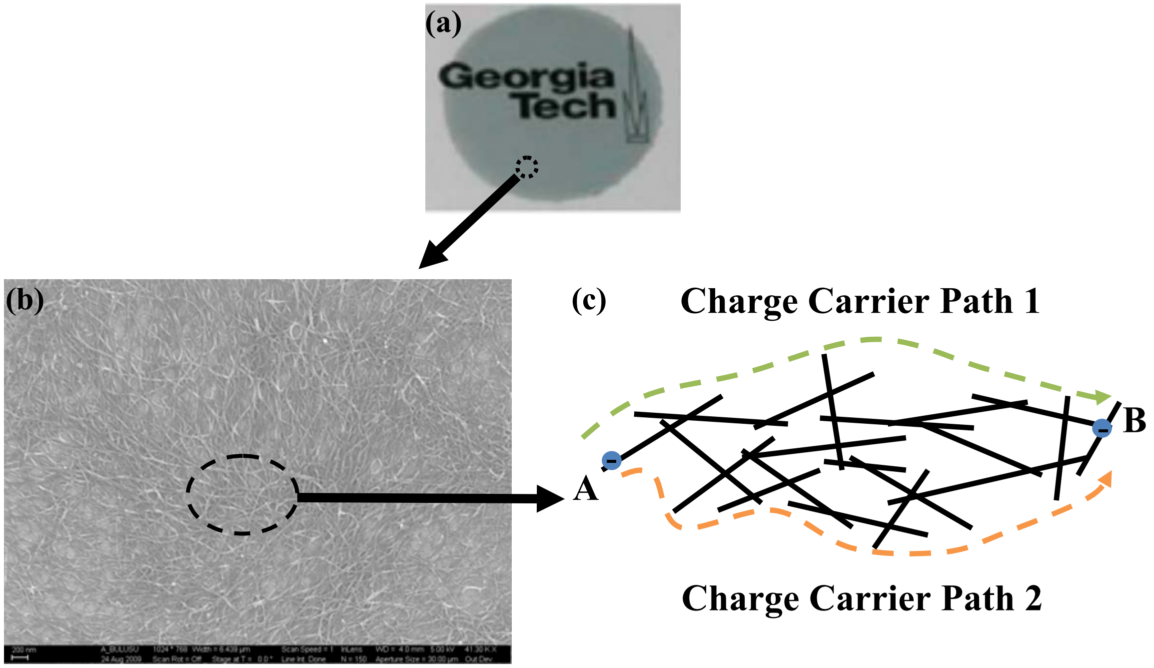

Figure 2.14 (a) Vacuum filtered SWNT on glass. The Georgia Tech emblem is presented behind the electrode to illustrate its transparency. Taken from reference [67] (b) SEM image of nanotube network at 41,300x magnification [86]. (c) SWNT network with continuous conduction pathway for electrons to travel through.

As the charge carrier travels from point A to B it must find nanotube intercalation pathways to conduct through to reach its destination at point B. The lack of nanotube intercalation pathways present a significant potential barrier that the charge must overcome to electrically conduct. Thereby increasing interparticle resistance and degrading the electrical conductivity of the nanotube network (NTN). Therefore, it is ideal for a nanotube network to have high enough surface coverage such that the percolation threshold has been reached, as was discussed in the section 2.1, to minimize interparticle resistances.

In nanotube networks (NTN) surfactants also contribute to interparticle resistance due to their insulating nature and by limiting nanotube-nanotube contact. However, surfactants are necessary to disperse nanotubes into water. A surfactant is an organic amphiphilic compound that has a hydrophobic tail and a hydrophilic head (See Section

2.4.2). As is demonstrated in Figure 2.15a the hydrophobic tail adsorbs onto the surface of the nanotube and the hydrophilic tail interacts with water molecules to disperse CNTs in water. As an example, the surfactant sodium dodecyl sulfate (SDS) typically adsorbs onto the nanotube in a structureless manner[47]. It can then be imagined that as a charge carrier travels through the CNT it has to "hop" to another CNT at the nanotube-nanotube contact as is presented in Figure 2.15b.

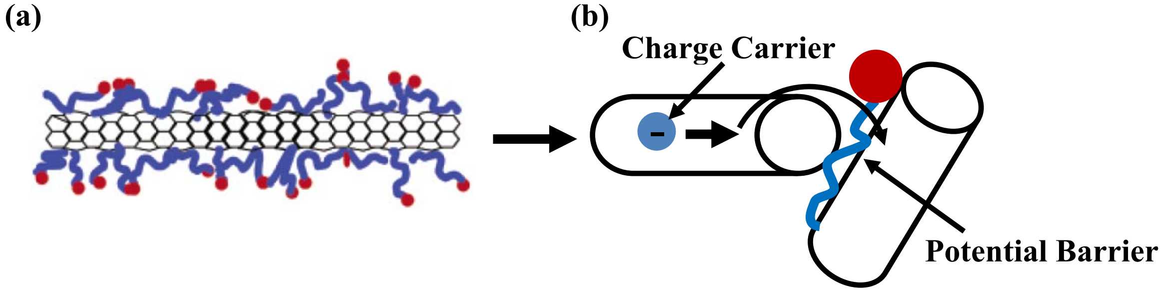

Figure 2.15 (a) Structureless surfactant adsorbed onto the surface of a carbon nanotube. Taken from reference [47]. (b) Schematic of a charge conducting through a nanotube and encountering surfactant that creates a potential barrier for the charge to hop onto the connecting nanotube.

The insulating surfactant presents a potential barrier that the charge carrier must overcome to conduct through the nanotube network. If the charge carrier in Figure 2.15b has sufficient energy to overcome the barrier it will "hop" over the barrier, resulting in a loss in energy. If the charge does not have enough energy to overcome the barrier, quantum mechanics predicts that the charge has a nonzero probability to pass through the barrier, or "tunnel" through it. This phenomena is known as tunneling, which also results in a loss in energy of the charged particle. In either case, the nanotube network will experience an increase in interparticle resistance. Therefore, it is desirable to remove insulating surfactants as will be investigated in chapter 4.

It also noted that carbon nanotubes are not all of the same electronic type [87]. CNTs can be either metallic or semiconducting depending on the wrap angle in which it is rolled (See Appendix A). Contact between carbon nanotubes of heterogeneous electronic type form potential barriers, formally known as Schottky barriers, φ_b, which are produced through a mismatch in work functions[20, 62]. These potential barriers again have a negative impact on the interparticle resistance.

As synthesized single wall carbon nanotubes (SWNTs) typically have a concentration of ~2/3 semiconducting single wall carbon nanotubes (Sc-SWNTs) and ~1/3 metallic single wall carbon nanotubes (M-SWNTs). Expanding upon Figure 2.14, the intrinsic optimal conduction pathway for a charge carrier to conduct through in the NTN would be through the metallic nanotubes (colored green) as shown in Figure 2.16. However, Sc-SWNTs can be p-doped through chemical treatment to exhibit metallic-like behavior[66]. This chemical doping adds highly conductive pathways for charge carriers to conduct through in the nanotube network thereby reducing interparticle resistance. In summary, to minimize interparticle resistances it is desirable to have sufficient surface area coverage in the NTN such that the percolation threshold has been reached; to remove insulating surfactants; to have nanotube networks of homogeneous electronic type; and to dope Sc-SWNT nanotube to have them exhibit metallic behavior to add highly conductive percolation pathways.

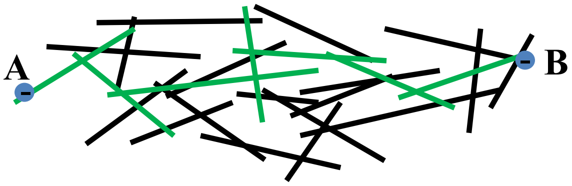

Figure 2.16 Schematic of optimal conduction pathway for a charge carrier to conduct through to reach point B when starting from point A.

2.6.2 Intraparticle Resistances of Carbon Nanotubes

The electronic properties of individual nanotubes are governed by the nanotubes electronic density of states. Examples of the metallic SWNT and semiconducting SWNT density of states are presented in Figure 2.17a and b, respectively. Where the intrinsic Fermi level, the energy level up to which the density of states are filled of charge carriers that are available for electrical conduction, intrinsically lies at 0eV. The singularity points in the DOS for both M-SWNT and Sc-SWNT are called van Hove singularities and the distance between mirror van hove singularities are called energy transitions M_{11}, M_{22}, S_{11}, S_{22}, and S_{33} see Figure A.6 in Appendix A.

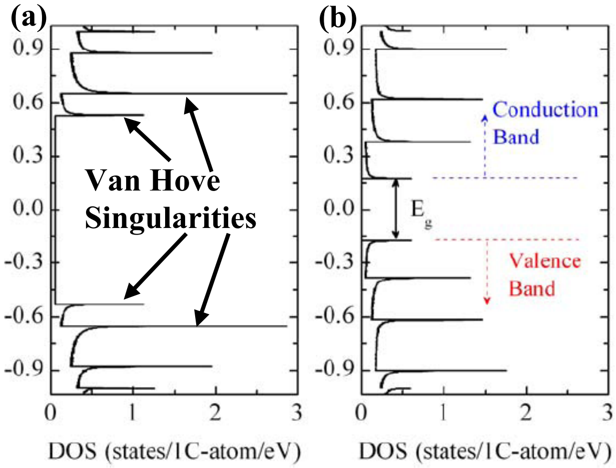

Figure 2.17(a) Electronic density of states of a (9,0) metallic SWNT. (b) Electronic density of states of a (10,0) semiconducting SWNT. Taken from reference [20].

The intraparticle resistance of individual carbon nanotubes is determined by equation 2.10. Where the charge carrier mobility, μ, is a material property that is dependent on structural quality of the individual nanotube and was discussed in the previous section; *e* is the electron charge which is a fixed constant; and finally the density of charge carriers, *n*, can be controlled via chemical doping.

$$\boldsymbol{R_{sh} = \frac{1}{ne\mu}} \tag{2.10}$$

As purchased SWNTs used in this work were functionalized with carboxylic acid groups or surface functional groups that were attached to the ends of nanotubes and at defect sites that p-dope SWNTs, see Figure 2.12. The carboxylic acids along with adsorbed oxygen dopants on the nanotubes effectively shift the Fermi level downwards from its intrinsic position in the SWNT density of states as presented in Figure 2.18. For a discussion on the structure of carbon nanotubes and the physics involved to give rise to the density of states please see Appendix A.

To begin Figure 2.18a and b presents the density of states of as-made semiconducting and metallic SWNTs. Where the Fermi level is below 0eV due to hole doping from surface functional groups and oxygen dopants. The grey areas in the density of states correspond to filled states and the white areas correspond to empty states. In order for a nanotube to conduct it has to travel from a filled state to an empty state. The as-made Sc-SWNT has relatively little empty states for charges to conduct through. Therefore, the majority of the charges will have to overcome an energy gap to reach the conduction band, where there are empty states for the charge carriers to conduct.

Hole doping is advantageous for Sc-SWNTs as it removes electrons in the valence band leaving more empty states for charges to conduct through as shown Figure 2.18c. Alternatively, p-doping can be thought of as increasing the density of charge carriers (n) in the individual nanotubes and thereby decreasing the intraparticle resistance defined in equation 2.10. This presents negligible resistance for charge carriers to conduct in the valence band of the Sc-SWNTs; until the empty states are filled again by conducting charge carriers. This limited zero resistance in the valence band for charge carriers is the reason why the semiconducting SWNTs can exhibit “metallic-like behavior” when doped to a high degree. By comparison it is seen in Figure 2.18d that M-SWNTs are not significantly impacted by hole-doping. However, p-doping (typically HNO_3) induces defects in carbon nanotubes, which negatively impacts charge carrier mobility (μ). To summarize, intra-nanotube resistance is dependent on the electronic type of the CNT, the extent to which it is doped, and the structural quality of nanotubes.

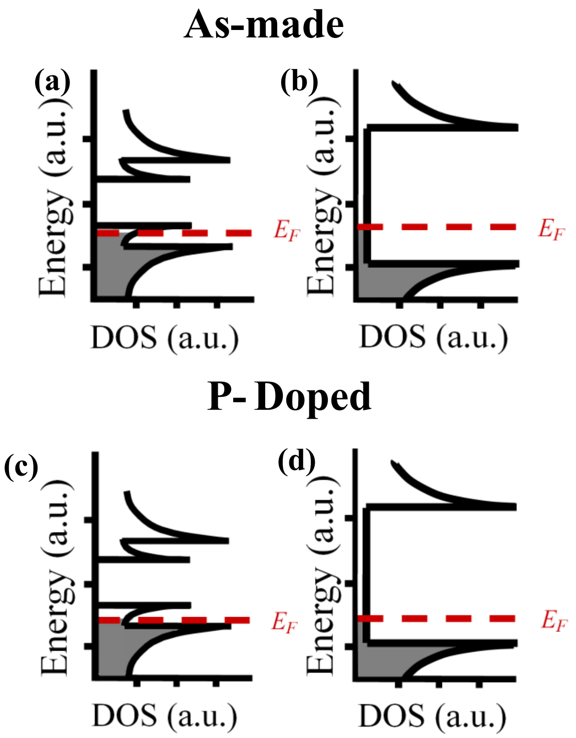

Figure 2.18 (a) Filled states in as-made Sc-SWNT density of states. (b) Filled States in as-made M-SWNT density of states. (c) Filled states in p-doped Sc-SWNT density of states. (d) Filled States in p-doped M-SWNT density of states. Adapted from reference [20].

2.6.3 Global 2D Sheet Resistance in Nanotube Networks

Sections 2.6.1 and 2.6.2 discussed interparticle and intraparticle resistances in nanotube networks (NTNs). This section aims to interconnect the two resistances discusses how they sum up to the global 2D sheet resistance, and to motivate why the removal of surfactants are important.

Currently carbon nanotube electrodes have inferior optoelectronic properties to indium tin oxide. However, with material optimization the optoelectronic properties of SWNTs can be significantly increased[38]. Overall conductance in CNT electrode is limited primarily by interparticle resistance which has been reported to be 4 orders of magnitude larger than intraparticle resistances[38]. The interparticle resistance that arises from the presence of insulating surfactants and Schottky barriers contribute to reducing carrier mobilities for individual nanotubes at 100,000cm^{2}V^{-1}s^{-1} to mobilities as low as 10-

100 $\mathrm{cm}^2\mathrm{V}^{-1}\mathrm{s}^{-1}$[38] for nanotube networks (NTNs). This dramatic decrease in charge carrier mobility has a direct impact on the sheet resistance of nanotube electrodes recall equation 2.7 ($\boldsymbol{R}_{\mathbf{sh}} = (\boldsymbol{ne\mu t})^{-1}$).

The presence of Schottky barriers can be lowered through type-sorting nanotubes, most notably through density gradient ultracentrifugation[62] with surfactants SDS and SC. Furthermore, the removal of surfactants in nanotube electrodes can significantly improve electrical conductivity, as the surfactants limit tube to tube contact and present potential barriers for charge carriers to overcome when conducting in the NTN.

Nitric acid has been shown to remove the surfactant sodium dodecyl sulfate (SDS), but does not completely remove the surfactant sodium cholate (see Chapter 4, section 4.3.2). However, nitric acid (HNO_3) treatment on SWNT transparent electrodes has been shown to p-dope SWNTs[42]. However, this doping process is not stable as the dopants naturally desorb from the nanotubes when exposed to air. Furthermore, treatment with concentrated nitric acid has been shown to damage carbon nanotubes by inducing defects. The introduction of defects negatively impacts the charge carrier mobility within nanotubes and thereby negatively impacting R_{sh}. In literature, it has been shown that the effects of nitric acid by p-doping overall positively affect the 2D sheet resistance, but it is of interest to determine if the sheet resistance can be further dropped by employing an annealing technique to remove the surfactant sodium cholate.

Annealing in an inert environment (e.g. argon) up to temperatures of 1000°C, have been shown in this work to effectively remove the surfactant SDS and SC to a relatively high degree. However, as purchased SWNTs used in this work were functionalized with carboxylic acid groups that were attached to the ends of nanotubes and at defect sites (see Figure 2.12). These carboxylic acid groups or surface functional groups p-dope or hole dope SWNTs. Through thermal annealing it is possible to remove surface functional groups and thereby shift the Fermi level back to its intrinsic position.

This effectively decreases the density of charge carriers in semiconducting SWNTs and thereby lowers the intraparticle resistance, but has a minimal impact on metallic SWNTs. This concept is illustrated in Figure 2.19. This brings rise to a competing effect in thermally annealed SWNT electrodes between decreases in interparticle resistances through the removal of insulating surfactants and increases in the intraparticle resistance caused by the removal of surface functional groups.

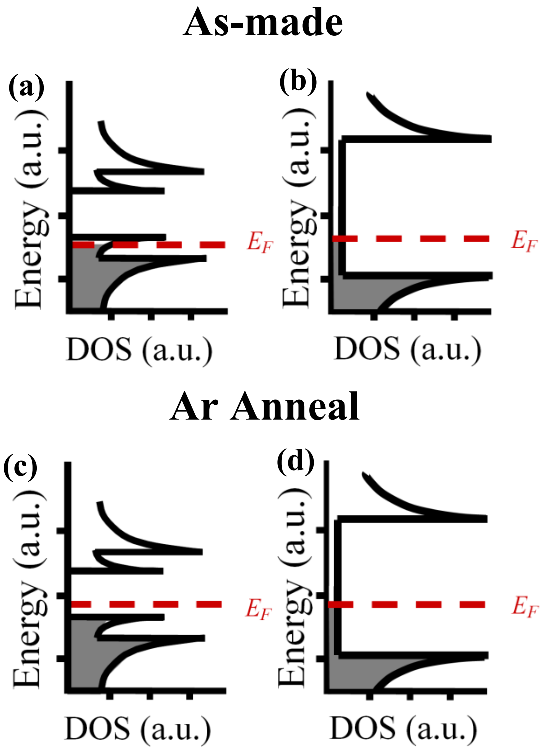

Figure 2.19 (a) Filled states in as-made Sc-SWNT density of states. (b) Filled States in as-made M-SWNT density of states. (c) Filled states in Ar anneal Sc-SWNT density of states. (d) Filled States in Ar anneal M-SWNT density of states.

It is expected that M-SWNTs will benefit more from thermal annealing as it is relatively insensitive to dedoping effects. While it is expected that Sc-SWNTs will be more sensitive to the removal of the surface functional groups. However, it is not know if the effect of surfactant removal will dominate over the removal of surface functional groups that are attached to the Sc-SWNTs.

2.7 Conclusion

This chapter conceptually discussed electrical conduction in carbon nanotube transparent conductive electrode that is needed for chapters 3 and 4. A theoretical discussion of the structure and development of the density of states of carbon nanotubes can be found in appendix A. The important topics covered in this chapter are summarized below.

Section 2.1 discussed the main figure of merits, used to characterize transparent electrodes produced in this work; which included sheet resistance, optical transmittance, and the graphitic to defect intensity ratio to assess structural quality of SWNTs and graphene. Section 2.2 discussed SWNT solution fabrication techniques and presented a literature review of the state-of-the-art electrodes for mixed SWNT films. Section 2.3 presented a literature review of the density gradient ultracentrifugation technique that is currently employed by vendor Nanointegris to produce type-sorted SWNTs. Furthermore, a literature review of the stat-of-the-art electrodes for M-SWNTs and Sc-SWNTs is presented. Section 2.4 discussed p-doping techniques, used to obtain state-of-the-art carbon nanotube electrodes. Techniques involving p-doping via HNO_3 and $SOCl_2$ treatment through intercalation of NO_3^- molecules at interstitial sites and nucleophilic substitution of hydroxyl groups with acyl groups on functionalized SWNTs, respectively, were discussed.

Section 2.5 introduced graphene and SWNTs and discussed the importance of its material properties, most notably the relatively high mobility of charge carriers of ~200,000$cm^{-2}V^{-1}s^{-1}$ [80] and ~100,000$cm^{-2}V^{-1}s^{-1}$ [81], respectively. Section 2.6 gave a brief introduction to the competing effects between interparticle resistances associated with the removal of insulating surfactants that effectively improve electrical conductivity; and the intraparticle resistances associated with the removal of surface function groups through thermal annealing that effectively degrade electrical conductivity. The total sum of the intraparticle and interparticle interactions give rise to the global 2-dimensional sheet resistances, which is heavily used in this thesis to characterize electrical performance of electrodes.

Up to this point the state-of the art for CBNs including mixed SWNTs, metallic SWNTs, and Sc-SWNTs that are known to the author have been presented. The state-of the-art-films for mixed SWNTs produced by Wu et al. is 30Ω/sq coupled with 70%T, which corresponds to a conductivity ratio of 32.2. The current state of the art for M-SWNTs electrodes was produced by Jackson et al. via p-doping with HNO_3 and subsequently with $SOCl_2$ doped yielding a conductivity ratio of 12.7 by having 76Ω/sq at 70%T. The state-of-the-art for Sc-SWNTs electrodes was also produced by Jackson et al. via p-doping with HNO_3 and subsequently with $SOCl_2$ doped yielding a conductivity ratio of 16.1 by having 60Ω/sq at 80%T.

Carbon nanotubes optoelectronics properties are currently inferior to indium tin oxide. Improving the optoelectronic properties of CNTs is an ongoing effort and currently graphene and CNT graphene composites are already offering electrodes with extremely competitive electronic properties. As a result, the goal of this thesis is not to produce CNT electrodes with high enough conductivity ratios to replace ITO. Rather, the goal of this thesis is to have a fundamental understanding of the physics involved with the removal of surfactants for solution processed SWNT (and graphene) electrodes, both at the nanoscale and at the macroscale, as will be discussed thoroughly in Chapter 4.

Following up the literature review presented in this chapter, chapter 3 will present the experimental methodology employed in this thesis. Chapter 4 will investigate the impact of surfactant removal on CNT electrode performance. Chapter 5 will present work done with graphene SWNT composites.

CHAPTER 3 : EXPERIMENTAL METHODOLOGY

3.1 Introduction

Chapter 2 discussed electrical conduction in carbon nanotube transparent conductive electrodes, provided a literature review for mixed SWNTs and type sorted SWNTs, and explained why surfactant removal may play a role in limiting electrical conduction. Chapter 3 proceeds with discussing the experimental methodology employed to fabricate and characterize carbon nanotube transparent electrodes and outlines experiments designed to investigate the removal of surfactants in chapter 4.

3.2 Solution Processed Carbon Nanomaterials

Solution processed carbon based nanomaterials used in this work include mixed SWNTs, metallic SWNTs (M-SWNTs), semiconducting SWNTs (Sc-SWNTs), and graphene. Each solution processed carbon based nanomaterial reveals their own individual bits of information to understand the impact of surfactant removal on CBNs as a whole. To begin a flowchart presenting the surfactants used to disperse each carbon based nanomaterial is presented in Figure 3.1.

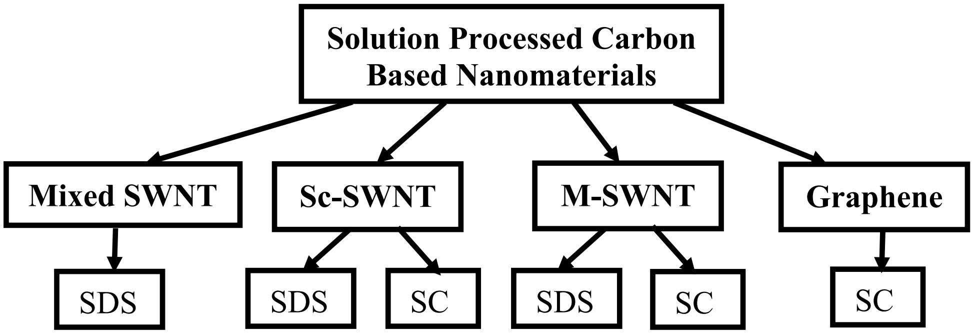

Figure 3.1 A flowchart of solution processed carbon based nanomaterials presenting the surfactants used to solution process the corresponding carbon based nanomaterials. Surfactants SDS and SC correspond to sodium dodecyl sulfate and sodium cholate, respectively. Mixed SWNTs correspond to as synthesized carbon nanotubes with ~2/3 semiconducting SWNTs (Sc-SWNTs) and ~1/3 metallic SWNTs (M-SWNTs).

3.2.1 Dispersion of Mixed Carbon Nanotubes

Prior to any experimental work being performed all glassware was thoroughly cleaned through subsequent rinsing with acetone, methanol, isopropanol alcohol, and deionized water which were followed by thorough drying with an air gun. To prepare Mixed SWNTs aqueous solutions, P3-SWNTs in powder form (arc discharge synthesized) were purchased from Carbon Solutions, Inc. The P3-SWNTs are purified with nitric acid and are highly functionalized with 4-6 atomic % carboxylic acid groups. The P3-SWNTs had catalyst impurity content between 5-10 weight % and a carbonaceous purity >90% (ratio of SWNTs to all carbonaceous materials). The mean length and diameter of the purchased P3-SWNTs are 1μm and 1.4 nm, respectively.

The purchased P3-SWNT powder (Figure 3.2a) was added to ~0.5% w/v aqueous solution of SDS, where typical concentrations of SWNTs were 0.55mg/ml. The SWNT solution was sonicated with a VWR 75 bath sonicator for 1 hour, operated at power level 5, resulting in an approximate sonication power of 45 Watts. The SWNT solution was centrifuged with a VWR Galaxy 16D Digital Microcentrifuge for 1 hour at 16,000 x g. The centrifugation process forced residual metal catalysts, impurities, and large undissolved SWNT aggregates to the bottom of the centrifuge tube. After the centrifugation process finished, the top ~75% of solution was carefully decanted and the bottom 25% was discarded. The new solution underwent an additional sonication and centrifugation step, were again only the top 75% of solution was used. The second sonication step was done to disperse any undissolved SWNT and to decrease the SWNT bundle size. The second centrifugation step was done to further remove residual impurities and large SWNT aggregates. The final SWNT solution is shown in Figure 3.2b

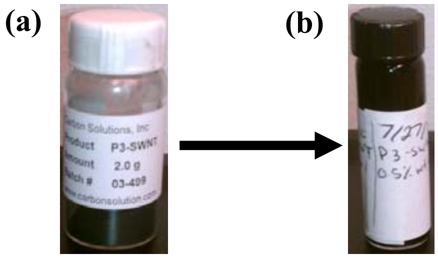

Figure 3.2 (a) P3-SWNT powder purchased from Carbon Solutions, Inc. (b) Dispersed P3-SWNT solution.

3.2.2 Metallic and Semiconducting SWNT Electrodes

Metallic and semiconducting SWNT electrodes were prepared from solutions purchased from Nanointegris. The M-SWNT and Sc-SWNT electrodes contained electronic type purity of >95% as specified by Nanointegris. For the M-SWNT solutions the remaining <4% corresponded to Sc-SWNTs and vice versa. The SWNT solutions purchased from Nanointegris had a mean diameter of 1.4nm and a mean length of ~1μm. The type sorted solution were vacuum filtered as will be explained in section 3.3. Examples of vacuum filtered Sc-SWNT and M-SWNT solutions are presented in Figure 3.3 b and d, respectively.

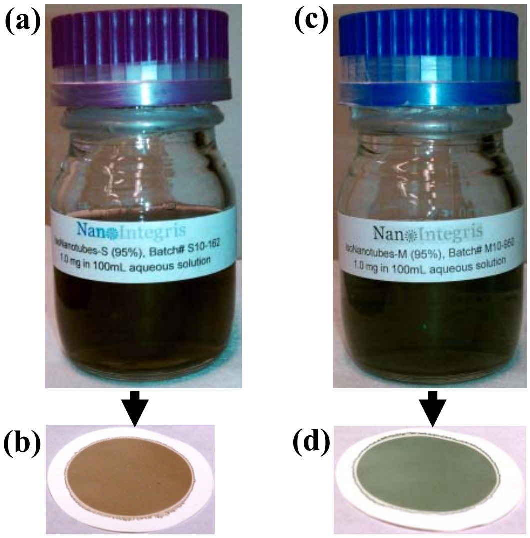

Figure 3.3 (a) Picture of type sorted >95% Sc-SWNT solution purchased from Nanointegris. (b) Vacuum filtered Sc-SWNT electrode. (c) Picture of type sorted >95% M-SWNT solution purchased from Nanointegris. (d) Vacuum filtered M-SWNT electrode.

3.2.3 Research Grade Graphene Puresheets Electrodes

Graphene puresheets research grade solution was purchased from Nanointegris. The graphene puresheets solution is specified by Nanointegris to have 27% single layer content, 48% double layer content, 20% triple layer content, and 5% four plus layer content. The average graphene flake size is specified to be 10,000nm^2. In Figure 3.4 a picture of the graphene puresheets solution utilized for this work. The graphene puresheets were vacuum filtered and an example of a vacuum filtered graphene puresheets electrode is presented in Figure 3.4b.

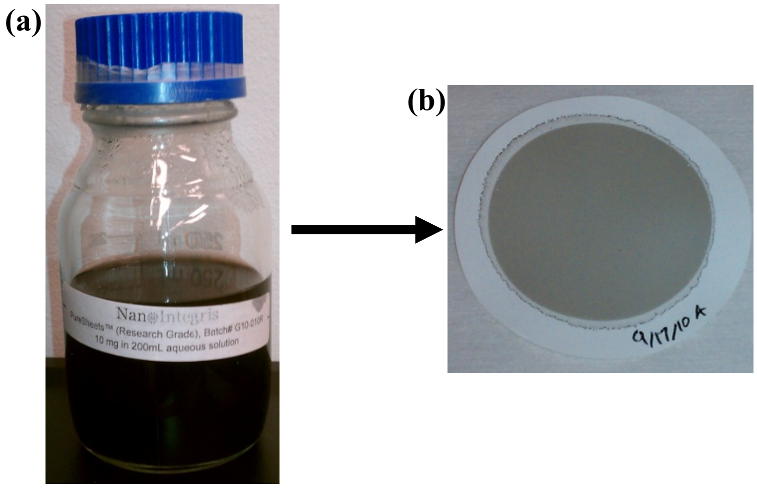

Figure 3.4 (a) Picture of Graphene Puresheets Research Grade solution purchased from Nanointegris. (b) Vacuum filtered Graphene Puresheets electrode.

3.3 Vacuum Filtration

Carbon nanotube transparent electrodes were first prepared by Wu et al. through the use of the vacuum filtration method[28], this vacuum filtration technique was later employed for other carbon based nanomaterials (CBNs) including graphene oxide and solution processed graphene. It should be noted that processing conditions and the presence of contaminants have a profound impact on the quality of the CBN electrodes produced. For a thorough discussion on this topic see Appendix C.

To prepare CBN transparent electrodes, first the processed CBN solution was diluted with 30ml of DI water. In a separate beaker, 1 ml of 0.5% w/v SDS in DI water was also diluted in 30ml of DI water. The diluted CBN solution and 0.5% w/v SDS in DI water were bath sonicated for 2 minutes at power level 5. A minimal sonication time was done to avoid structural damage to the carbon based nanomaterials. Next, a Millipore mixed cellulose ester (MCE) filter membrane was rinsed with 60ml of DI water. The

MCE filter membrane had a 47mm diameter and a pore size of 0.1µm. The rinsed MCE membrane was then placed on the center of the glass frit surface, see Figure 3.5a. Subsequently, the diluted 0.5% w/v SDS solution was vacuum filtered (vacuum powered via 1/8hp vacuum pump) through the top (shiny) face of the MCE membrane to prepare the membrane for filtration of the CBN solution (setup shown in Figure 3.5b). Afterwards, the diluted CBN solution was vacuum filtered through the MCE filter membrane to form a CBN thin film on top of the membrane (Figure 3.5c). Vacuum filtering through the bottom (dull) face or not preparing the membrane, resulted in a nonuniform, low quality CBN electrode.

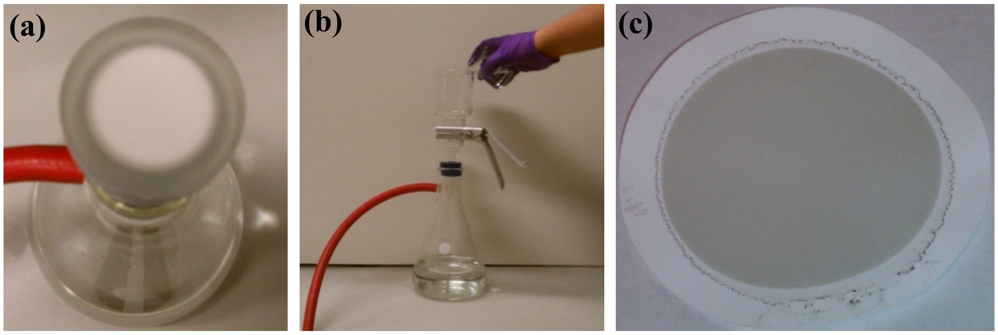

Figure 3.5 (a) Picture of vacuum filtration setup. (c) Glass frit where MCE membrane is placed on top of. (c) Vacuum filtered SWNT on MCE membrane.

The vacuum filtered CBN film was then heated at 70°C until dry (~10 minutes) and rinsed with 60ml of DI water to partially remove surfactants on CBN electrodes. It must be noted that the CBN electrode on the MCE membrane could only be rinsed after the film had completely dried. Rinsing prior to the CBN electrode completely drying would compromise the integrity of the film by creating splotches in the film. Allowing the film to completely dry allows time for the van der Waals forces to develop and bind together the CBN electrode network. The rinsed CBN film was placed on the center of the glass frit again and 60ml of DI water were vacuum filtered to further remove surfactants. The thoroughly rinsed CBN film was again heated at 70°C until dry.

3.3.1 Film Transfer Process

Due to the random morphology of CBN electrodes produced through the vacuum filtration technique, there is non-negligible variability from film to film. To minimize this variability, films were typically cut in half before or after being transferred. One half of the electrode was used as baseline to compare against the other half.

To begin transferring the CBN film from the MCE membrane to a transparent substrate, the CBN film was first thoroughly cleaned with IPA to remove dust particles or possible contaminants from the lab. The wet CBN film was then carefully placed on top of a clean transparent substrate, typically glass, quartz, or fused silica. The wet CBN electrode on the transparent substrate was again thoroughly soaked with IPA and firmly pressed onto the transparent substrate to promote adhesion, as shown in Figure 3.6a. The well adhered CBN film, while still wet, was swiftly placed on top of an acetone vapor bath to begin dissolution of the membrane, as shown in Figure 3.6b. Once the MCE membrane became transparent the CBN film was placed at a 45° angle face up in an acetone bath for ~7 minutes (Figure 3.6c), removed vertically, and placed on top of a hot plate at 60°C for ~5 minutes to promote adhesion.

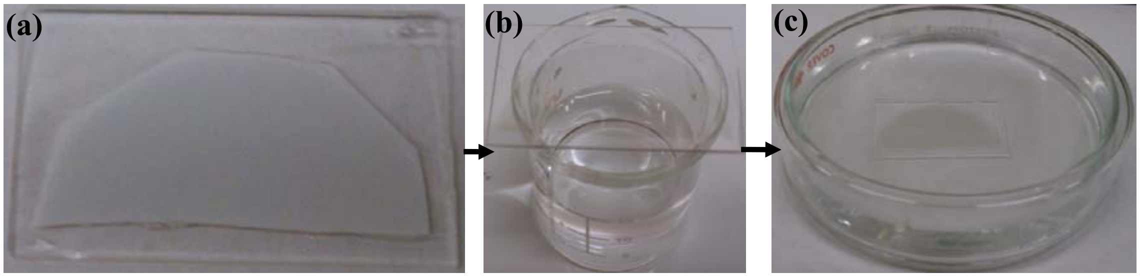

Figure 3.6 (a) SWNT electrode wetted with isopropanol alcohol on top of quartz. (b) SWNT electrode placed on top of acetone vapor bath to dissolve MCE membrane. (c) SWNT electrode placed in acetone bath to dissolve MCE membrane.

The SWNT film was removed vertically and inserted at a 45° angle to minimize buoyancy forces applied onto the SWNT film during immersion. Not removing the

SWNT film vertically or inserting the SWNT film vertically resulted in the film lifting off the substrate. Next, the SWNT film on the transparent substrate was placed in 4 sequential one hour acetone baths to fully dissolve the MCE membrane. After the SWNT film was removed for the first three acetone baths, the films were allowed to air dry completely before placing it into the next acetone bath. Not allowing the films to air dry completely before placing it into the next acetone caused the wet portions of the electrode to lift off the transparent substrate during immersion. Finally, after the last acetone bath immersion time finished, the films were carefully and slowly dried with an air or nitrogen gun.

After the transparent electrodes were produced the optoelectronic properties and structural quality were characterized. Section 3.4 discusses a primary figure of merit, sheet resistance, R_{sh}, and the transfer length method (TLM) used to measure it. Section 3.4 discusses optical transmittance and ultraviolet visible near-infrared spectroscopy technique used to characterize it. Section 3.5 discusses how Raman spectroscopy was utilized to characterize structural quality of carbon nanotubes and graphene.

3.4 Sheet Resistance and Contact Resistance

Sheet resistance, R_{sh}, is the 2D analog of bulk resistance, R, which was used to measure the resistance of thin films which are approximately uniform in thickness. Recall the equation of bulk resistance as shown in equation 3.1. The geometry of a simple rectangular thin film is shown in Figure 3.7. The cross-sectional area, A_c, is defined in equation 3.2 as is clear from Figure 3.7. By combining equations 3.1, 3.2 and rearranging yields equation 3.3, where R_{sh} is defined as the resistivity, ρ, divided by the film thickness, t. It can easily be seen that equation 3.3 is equivalent to equation 2.1 presented in Chapter 2 to define R_{sh}.

$$\boldsymbol{R = \rho \frac{L}{A_c}} \tag{3.1}$$

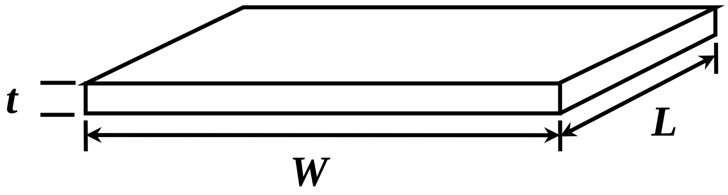

Figure 3.7 Geometry of a rectangular thin film with uniform thickness.

$$A_c = Wt \tag{3.2}$$

$$R = \frac{\rho}{t}\frac{L}{W} = R_{sh}\frac{L}{W} \tag{3.3}$$

The next concept of importance is contact resistance. Vacuum filtered graphene and SWNT films have an inherent surface roughness attributed with them. When contact is made between the probe and the transparent electrode, there will only be specific points that will make contact. This effect is pronounced in thin films as the lack of complete surface coverage reduces the number of contact points. When compared to bulk films were there is almost full surface coverage and this contribution is therefore typically neglected. Thus, there is a non-negligible contact resistance that is present when contact is made with CBN thin films.

In this work it was found that SWNT films that have desirable transparency are typically around 30nm thick. A 50nm SWNT film was reported to have a transmittance >70% [28], which is consistent with observations of the thickness of SWNTs done in this work. Specifically for SWNTs the transparency in the thin films is due to voids caused by a lack of complete surface coverage, this is evident even in a 150nm thick SWNT film as shown in the 1.5μm x 1.5 μm AFM scan in Figure 3.8.

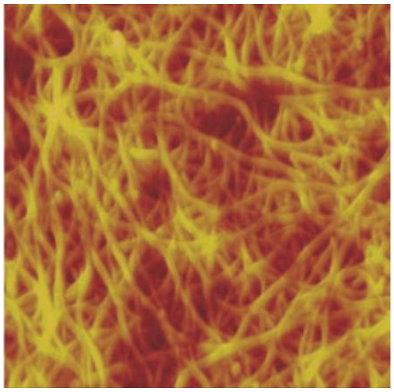

Figure 3.8 1.5µm x 1.5µm AFM scan of a 150nm thick Mixed SWNT film. Taken from reference [28].

In this thesis it was decided to utilize the transfer length method because of its repeatability, its ability to accurately determine sheet resistance and contact resistance, and ability to detect nonuniformities in the film. Other methods such as the two point and the four point probe methods were determined not to be suitable for the experiments conducted. A thorough discussion on the two point and four point probe methods along with the reasons as to why they were not employed can be found in Appendix B.

3.4.1 Transfer Length Method

The transfer length method (TLM) originally proposed by Shockley[88], is an extension of the transmission line method, that allows for the determination of contact resistance and avoids the use of geometrical correction factors to calculate the sheet resistance of electrodes. In the transfer length method, metallic fingers or contact pads are deposited on the transparent electrode to make better contact between the CBN electrode and the electrical probe. A schematic of the transfer length method is presented in Figure 3.9a. In the transfer length method the contact resistance refers to the resistance occurring at the metal/electrode interface arising from work function differences between the metal and the semiconductor(transparent electrode)[89] as described by Berger. In addition, not all of the current traveling through the electrode with resistance, R_{sh}, transfers through the contact resistance at the edge of contact pad; instead some of the current passes through the contact resistance and some of the current continues to travel laterally through the electrode at each point[90]. This forms contact resistance branches where the contact resistances are in series with the sheet resistance as shown in Figure 3.9b.

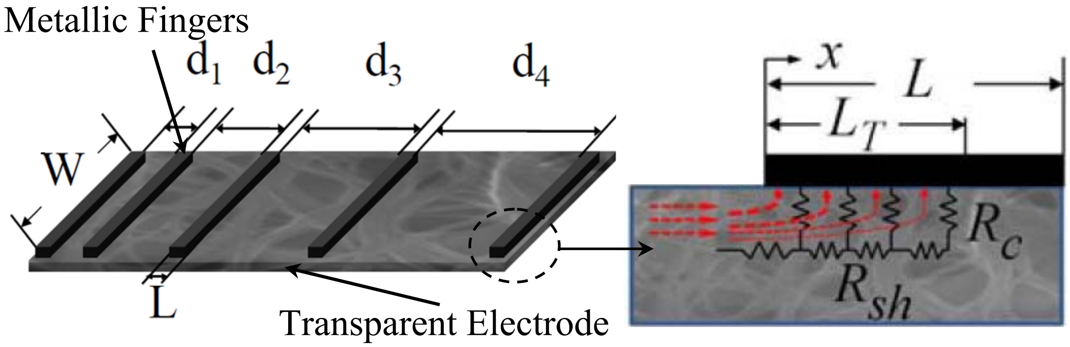

Figure 3.9 (a) Schematic of the transfer length method used to measure sheet resistance. (b) Schematic diagram of metallic contact/electrode interface with circuit model that includes resistance and flow of current. Figures a and b were taken from reference [91].

Per the discussion above contact resistance, R_c, is intrinsically dependent on the contact area and geometry. Therefore, it is of common practice to present a specific contact resistance, ρ_c (defined in equation 3.4), where the specific contact resistance is a convenient parameter to compare with contacts of varying sizes.

$$\boldsymbol{\rho_c = R_c A_s} \tag{3.4}$$

The TLM's ability to determine the sheet resistance of a transparent electrode is based on the concept of the transfer length L_T, which is described by Oussalah et al., as the characteristic length from the edge of the contact at which 1/e of the current has conducted from the semiconductor to the contact[92]. The transfer length is related to the specific contact resistance as determined by equation 3.12[90].

$$\boldsymbol{L_T = \sqrt{\frac{\rho_c}{R_{sh}}}} \tag{3.5}$$

The total resistance measured by making contact with silver metallic fingers at varying contact spacings, d_i , is governed by the equation 3.6[93, 94]. Through this method the resistance as function of d_i can be plotted and the sheet resistance can be approximated through a least squares linear fit[93], as shown in Figure 3.10.

$$R_T = 2R_c + \frac{R_{sh}}{W} d_i \tag{3.6}$$

The least squares linear fit is beneficial as any non-uniformities present in the electrode will not exhibit ohmic contact and give a relatively low R^2 value. Any TLM measurements made that did not exhibit linear behavior were considered invalid.

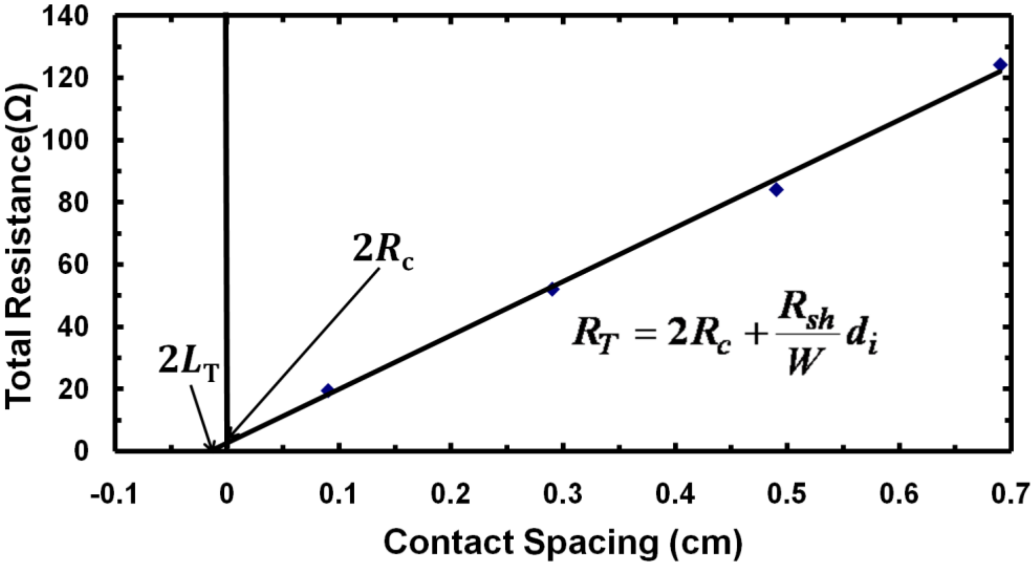

Figure 3.10 Sample plot obtained from the transfer length method of total resistance versus contact spacings. The contact resistance and transfer length are pointed out to demonstrate how they can be extracted via TLM.

In Figure 3.10 it is seen that the transfer length is dependent on how the contact resistance compares to the sheet resistance. As is the case in Figure 3.10, the sheet resistance is large in comparison to the contact resistance resulting in a small transfer length such that most of the current travels near the edge of the metal contact. The opposite is true, if the contact resistance is large when compared to the sheet resistance then there will be a relatively large transfer length such that most of the current does not travel near the edge of the contact. It is important to note that the transfer length can never exceed the length of the contact pad, *L*, as shown in Figure 3.9b. Furthermore, due to the number of contact resistance branches produced underneath the electrode metal contact, the contact resistance can be thought of as the equivalent resistance of an addition length of electrode material[90]. In fact, the contact resistance can be expressed as a function of L_T, L, R_{sh}, and W as presented in equation 3.7[89]. Furthermore if $L>2L_T$, then equation 3.15 can be simplified into equation 3.8.

$$R_c = \frac{R_{sh} L_T}{W} \coth\left(\frac{L}{L_T}\right) \tag{3.7}$$

$$R_c = \frac{R_{sh} L_T}{W} \tag{3.8}$$

The importance of the transfer length and specific contact resistance can be understood when considering the resistive power losses arising from the sheet resistance of transparent electrodes. As is the case with silicon based photovoltaics the addition of a metallic grid is often incorporated to reduce resistive power losses. Similarly, for organic photovoltaics Jackson et al. [20, 91] proposed the incorporation of a metallic grid to reduce resistive power losses by using SWNT films as transparent electrode as shown in Figure 3.11. Where the idea of using SWNT electrodes can be extended to the use of carbon based nanomaterial electrodes.

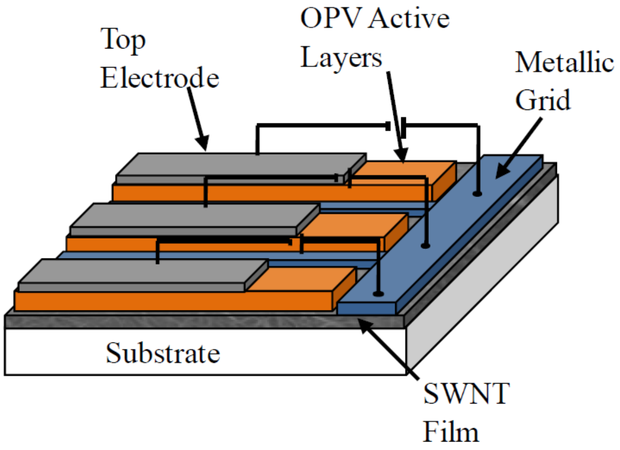

Figure 3.11 Organic photovoltaic architecture proposed by R. Jackson for incorporating metallic grids to reduce resistive power losses. Taken from reference [20].

Jackson et al. estimated the resistive power losses in the proposed organic photovoltaic architecture in Figure 3.11 to be governed by equation 3.8[20, 91]; where, the metallic finger separation, *d* was chosen to be 0.4cm to minimize resistive power losses due to the sheet resistance of SWNT electrodes. Thus, knowledge of the specific contact resistance and transfer length can be valuable parameters to be aware of when designing organic photovoltaic devices.

$$\boldsymbol{p}_{\mathbf{loss}} = \frac{\boldsymbol{Jd\rho}_{\mathbf{c}}}{\boldsymbol{VL}_{\mathbf{T}}} \tag{3.9}$$

Due to time constraints along with specific contact resistances and transfer lengths having large variances to the point that it follows a log-normal distribution, instead of a Gaussian distribution as shown by Jackson[20], R_c and L_T were not considered in this work.

3.4.2 Transfer Length Method Experimental Procedures

In this work, metallic fingers (e.g. silver) were deposited onto the transparent electrode via electron beam (E-beam) vapor deposition with the use of shadow masks. Silver was chosen as the contact metal because its work function (4.73eV)[95] is close to that of Sc-SWNTs (4.6eV) [20], M-SWNTs (4.5eV) [20], mixed SWNTs (4.3eV) [20] and graphene (4.66eV)[96], such that ohmic contact is made. However, it should be noted that the work function of SWNTs and graphene can be tuned by doping and annealing processes. Jackson[20] showed that the work function of nanotubes with a 1.4 nm mean diameter can be shifted as low as 4.0eV and as high as 5.0eV[20]. However, in all cases ohmic contact was made successfully for all SWNT and graphene films. Similarly for graphene it has been shown that its work function can also be shifted by up to ~0.5eV via chemical doping[97].

The shadow mask defined metallic finger spacings of d_1, d_2, d_3, and d_4 at 0.09cm, 0.29cm,0.49 cm, 0.69cm, respectively. The width and length of the metallic fingers are 1 cm and 0.1 cm, respectively. The shadow masks were created using cellulose acetate sheets or "transparency slides" and were cut using a Universal Laser Systems M360 laser cutter interfaced with AutoCAD2009.

It should be noted that if sheet resistance measurements are made directly after deposition of the silver lines the current traveling through the transparent electrode will spread as shown in Figure 3.12a. Therefore, the transparent electrode has to be "mesa etched" as shown in Figure 3.12 b so that current does not spread. In this work, the sides of the CBN electrodes that were not desired for TLM measurements were simply scraped away with a razor blade since the films are extremely thin as shown in Figure 3.12c.

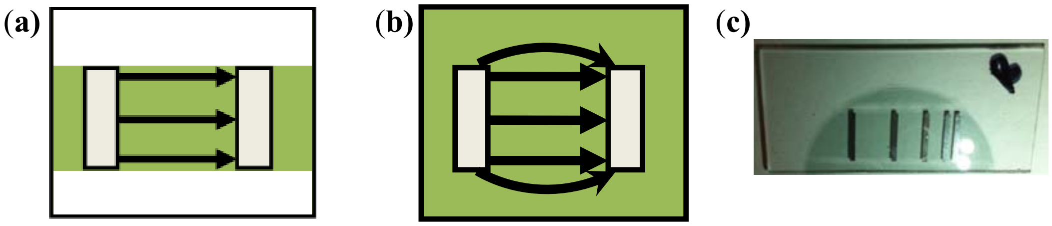

Figure 3.12 (a) Non mesa etched transparent electrode film that has current spreading contributing to experimental error. (b) Mesa etched transparent electrode that does not experience current spreading thus resulting in more accurate measurements. (c) Example of mesa etched as made M-SWNT electrode with silver contact fingers deposited.

3.5 Ultraviolet-Visible-Near-Infrared Spectroscopy

Optical transmittance of CBN transparent electrodes was measured through ultraviolet-visible-near-infrared (UV-Vis-NIR) spectroscopy. In UV-Vis-NIR spectroscopy a detector measures the intensity of light, I, after it has passed through a sample and compares it with the initial intensity of light, I_0, before it passed through the sample. The ratio I/I_0 is known as the optical transmittance of the sample and typically presented as $\%T$.

Generally a reference sample is used to account for a slight lost in intensity of light due to the sample holder or the transparent substrate, which is typically glass, quartz, or fused silica. In this case, the intensity measured after light has passed through the transparent substrate is taken as the initial intensity I_o. UV-Vis-NIR spectra are typically presented as optical transmittance as a function of wavelength. Where the wavelength of light can easily be extracted from the equation for energy of a photon as shown in equation 3.10, where $\hbar$ is the reduced Planck's constant, ω is the angular frequency, c is the speed of light, and λ is the wavelength

$$\varepsilon = \hbar\omega = \hbar\frac{2\pi c}{\lambda} \tag{3.10}$$

In this work a Cary 5E UV-Vis-NIR dual-beam spectrophotometer was utilized to measure the optical transmittance of transparent electrodes. Measurements were taken in at least 3 different points per sample, where typically two or more measurements would trace almost exactly the same plot. A representative plot that best represented (usually one of the traced plots) the collected data is presented in this thesis. A sample UV-Vis-NIR plot with data for an as-made M-SWNT film and a HNO_3 Doped M-SWNT film are presented in Figure 3.13.

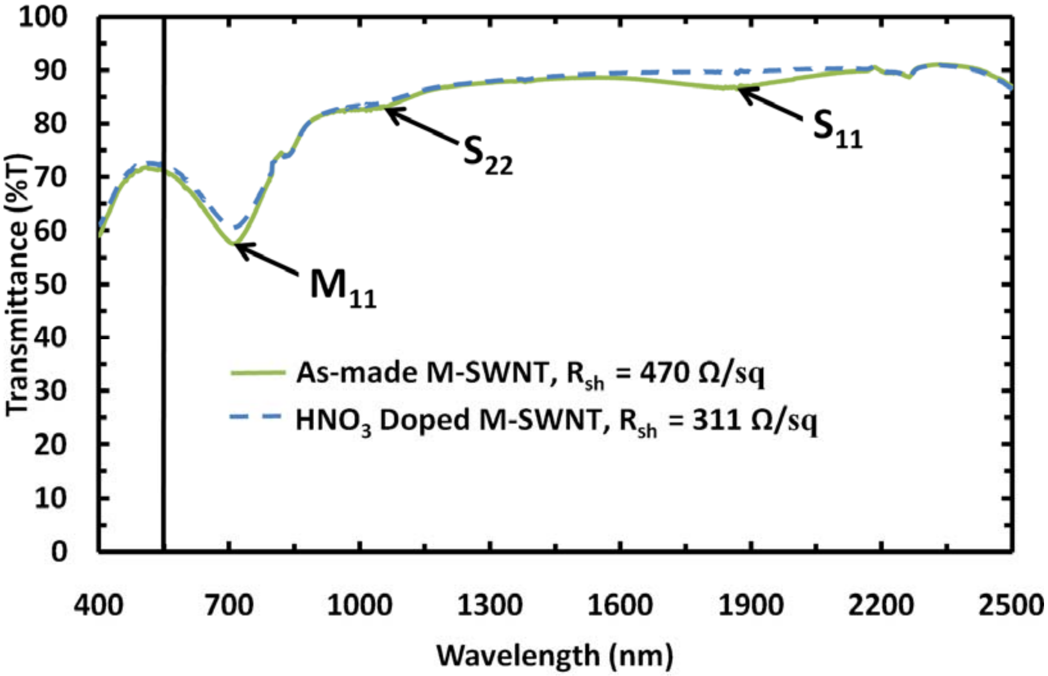

Figure 3.13 Sample UV-Vis plot of As Made and HNO_3 Doped Metallic SWNT films that were processed from the same MCE membrane with R_{sh}. The S_{11}, S_{22}, and M_{11} energy bands are pointed out in the plot, along with 550nm wavelength mark that is used for determining the representative transmittance[86].

In the UV-Vis-NIR spectra shown above the S_{11}, S_{22}, and M_{11} absorption peaks are readily seen and labeled. The energy transition peaks S_{11}, S_{22}, and the M_{11} were briefly discussed in Chapter 2; in section 2.6. Recall Figure A.6 where the DOS for Sc-SWNT and M-SWNT were presented. The reason that the Sc-SWNT absorption peaks, S_{11} and S_{22} and are present in the spectra of the M-SWNT electrode is due to the solution from which these films are processed not having 100% electronic type purity. Rather the M-SWNT solutions bought from Nanointegris have a purity of >95% and vice versa, as specified by the manufacturer.

To understand the absorption peaks observed in the UV-Vis-NIR spectra, a simple energy band structure diagram for a semiconductor is shown in Figure 3.14. Where the Fermi energy, E_f, is assumed to be at zero or exactly at the midpoint between the energy of the conduction band, E_c, and the energy of the valence band, E_v. The remaining variables are the separation energy, E_s, the energy gap, E_g, the electron affinity, χ, and the work function, Φ.

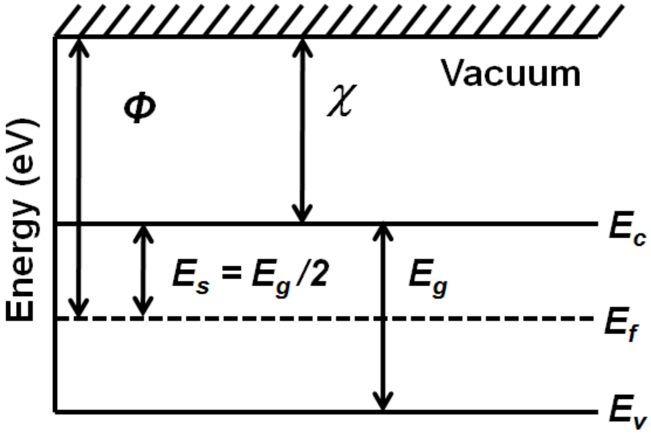

Figure 3.14 Energy band structure diagram for a semiconductor.

Recalling the density of states for both Sc-SWNT and M-SWNT (Figure A.6), the energy of the absorption peaks is equivalent to determining the energy gap and “pseudo” energy gap between mirror van Hove singularities for Sc-SWNT and M-SWNT, respectively. Fortunately, the separation energy for each absorption peak for both metallic and semiconducting nanotubes as a function of nanotube diameter in angstroms, Å, has been calculated and can be obtained from the so called Kataura plots [98].

From the manufacturer (Nanointegris) specifications the average tube diameter for arc-discharge Sc-SWNTs and M-SWNTs is 1.4 nm. Then by referring to the Kataura plot[98] the theoretical energy separation of the S_{11}, S_{22}, and M_{11} absorption peaks are 0.3eV, 0.6eV, and 0.9eV, respectively. Therefore, the energy gap (twice the energy separation) is 0.6eV, 1.2eV, and 1.8eV for the S_{11}, S_{22}, and M_{11} energy transitions, respectively. Comparing this with the observed absorption peak maximums in Figure 3.13 occurring at approximately at 710 nm, 1030nm, and 1900nm for the M_{11}, S_{22}, S_{11} energy transitions, respectively. Using equation 3.10 to determine the photon energies of light occurring at the specified wavelengths, the resulting energy transitions are 1.75eV, 1.20eV, and 0.65eV for the M_{11}, S_{11}, and S_{22} absorption peaks, respectively. Therefore, the observed absorption peak maximum positions are in good agreement with the theoretical peak positions.

Another interesting observation of the UV-Vis-NIR spectra shown in Figure 3.13 is that for the HNO_3 doped M-SWNT sample the S_{11} absorption peak appears to be "bleached" away. This phenomenon can be understood by again referring to the density of states of Sc-SWNT and M-SWNT (see Figure 2.18a and b) the Fermi level is assumed to be slightly below zero as is the actual case in nanotubes due to chemisorbed functional groups and unintentional doping as described by Jackson[20]. Unintentional doping occurs when oxygen from air interacts with CNT to p-dope them. Recalling that HNO_3 p-dopes CNTs through intercalation or simply put it withdraws electrons in the valence band, causing the Fermi level to shift downwards as shown in Figure 2.18c and d. The Fermi level shift due to HNO_3 effectively removes the S_{11} energy transition between the first mirror van Hove singularities in Sc-SWNTs. However, the Fermi level shift due to HNO_3 for M-SWNT only partially "bleaches" the M_{11} absorption peak.

Similarly, it can be shown that the removal of oxygen dopants and surface functional groups through thermal annealing effectively shifts the Fermi level back to zero and thereby maximizes the absorption peak (see Figure 2.19). This is easily noted in the UV-VIS NIR spectra as shown in Figure 3.15.

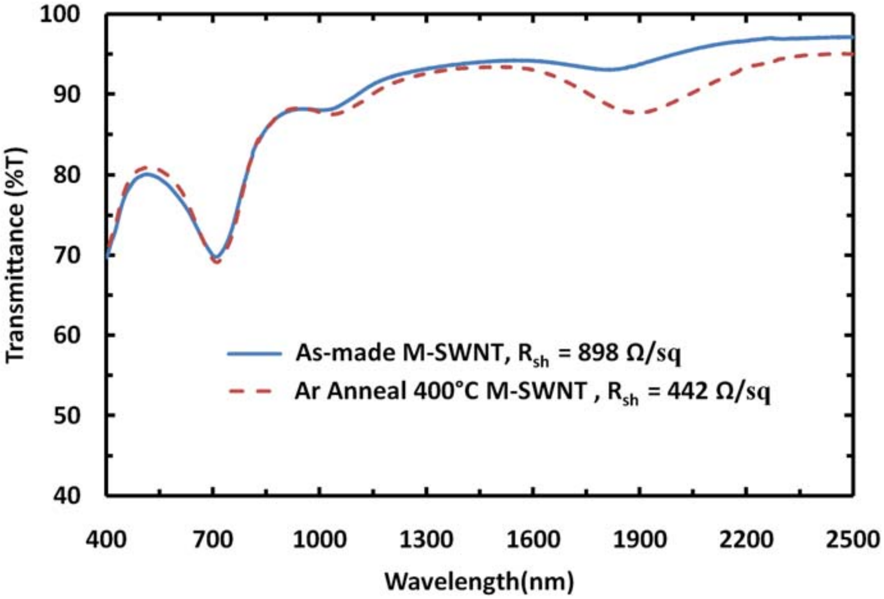

Figure 3.15 UV Vis NIR spectra of As-made M-SWNT and Ar Anneal M-SWNT. The S_{11} peak has noticeably intensified due to the removal of surface functional groups shifting the Fermi level back to zero.

Finally, it should be noted that since graphene is a so called zero band gap semiconductor, as can be noted by the DOS of graphene presented in Figure A.2, there are no absorption peaks present in the UV-Vis-NIR spectra for as-made or HNO_3 Doped graphene films as shown in Figure 3.16.

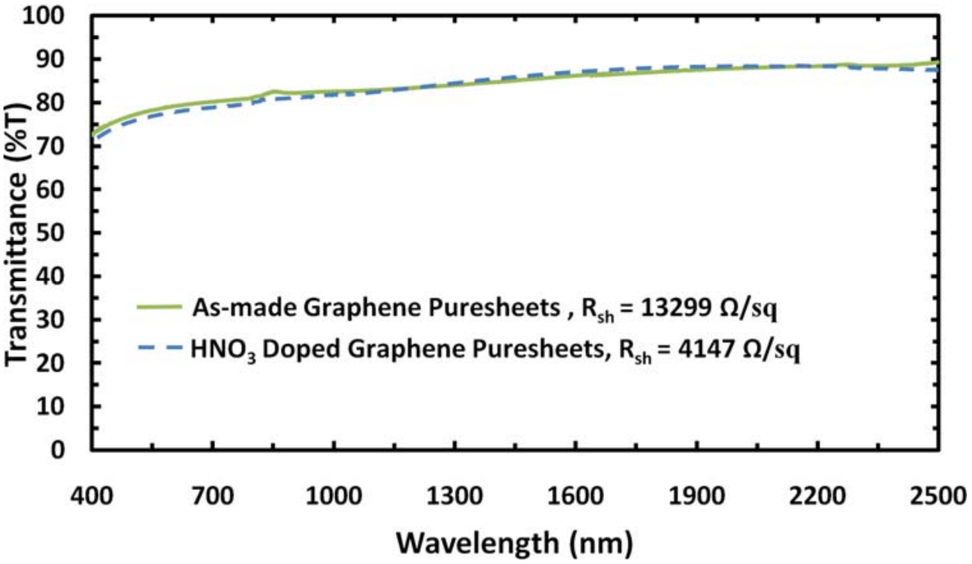

Figure 3.16 UV-Vis-NIR spectra of as-made GPS and HNO_3 doped GPS electrodes. As is apparent in the plot there are no visible absorption peaks

3.6 Raman Spectroscopy

To assess the structural quality of carbon based nanomaterial transparent electrodes, Raman spectroscopy was utilized. Raman spectroscopy is a powerful tool based on the inelastic scattering of light that is used to characterize aspects of the zone center optical phonons in a material. Such measurements can reveal the presence of defects, strain, temperature, composition, and some structural aspects of materials. Measurements were taken by irradiating the samples with a laser source and measuring the shift in the energy of scattered photons from the sample surface. The change in energy of the scattered photons was measured using a combination of a Rayleigh filter, spectrometer, and a detector. The principle of operation of Raman Spectroscopy is briefly explained below.

The radiation from the laser in the form of photons has energy, ε_i, when incident on the surface of a material, were it is transmitted, reflected, or absorbed. Specifically the photons that are absorbed by an electron or phonon (significantly less likely) are only considered in Raman spectroscopy. The absorbing particle at ground state with energy ε_g

is then promoted to an excited virtual energy state, ε_v. Upon relaxation of the absorbing particle back to ground state, a photon is re-emitted with a phonon energy of ε_i or ε_f, where ($\varepsilon_f \neq \varepsilon_i$). In the former case a photon is re-emitted with energy $\varepsilon_i = \varepsilon_v - \varepsilon_g$, or in other words the re-emitted photon's energy is equal to the energy of the initial phonon from the laser in a process known as elastic or Rayleigh scattering. In the more interesting latter case, the change in energy of the re-emitted photon is due to the excited particle absorbing or emitting an additional energy carrier. This event causes the excited particle to move to a secondary virtual energy state ε_{2v}, where the re-emitted phonon has energy $\varepsilon_f = \varepsilon_{2v} - \varepsilon_g$. This phenomenon is known as inelastic scattering or the Raman effect [99]. Inelastic scattering of a phonon has a probability of 1:10,000,000 and as such the elastically scattered photons are filtered out in measurements.

The change in energy of the photon in inelastic scattering can be equivalently described as the change in angular frequency of the photon. This equivalency becomes clear by recalling that the photon energy is $\varepsilon = \hbar\omega$, where $\hbar$ is Planck's constant and therefore the photon energy is directly proportional to the photon frequency. In Raman scattering the incident photon frequency ω_i is shifted by the optical phonon frequency ω_p known as the Raman shift. The intensity of the Raman signal at a given Raman shift is proportional to the number of phonons present at frequency ω_p to participate in the scattering process, which is material dependent[100]. Measured resonant peaks are well established for each specific material; this makes Raman spectroscopy a valuable tool to determine the presence of a material and associated defects present with it.

A Renishaw Invia Raman Microscope with a 488 nm Ar^+ laser was used in this work as pictured in Figure 3.17. Measurements were taken with 10mW laser power and measured at in at least 3 different spots per sample.

Figure 3.17 Renishaw Invia Raman Microscope with a 488 nm Ar^{+} laser. Taken from reference [99].

A sample Raman plot obtained from measuring graphene grown on nickel via CVD is shown in Figure 3.18. In graphene and CNTs there are three significant scattering modes that are present in the Raman spectrum including the D-band, G-band, 2D/G$^{'}$-band. These scattering modes generally appear at approximate wavenumbers, but can and do vary slightly from sample to sample. The peak position also depends on the laser wavelength.

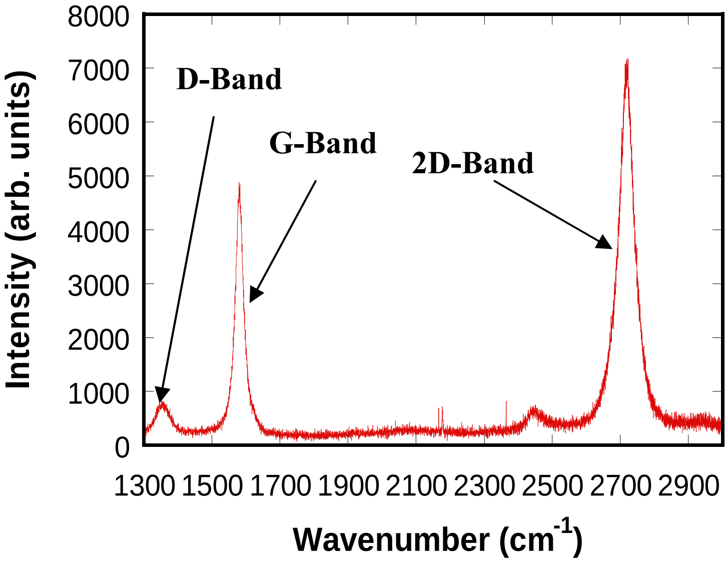

Figure 3.18 (a) Raman spectroscopy measurement of graphene grown on nickel via CVD.

The D-band occurs at ~1350 cm^{-1} and is generated from the scattering modes of structural defects in graphene. Therefore, the higher the intensity of the D-band the more defects that are present. The G-band occurs at ~1585 cm^{-1} and is commonly referred to as the graphitic peak because this scattering mode is present in most carbon-based materials. Therefore, the ratio of the intensity of the G-band and D-band (I_G/I_D) is used to quantify the structural quality of graphene and CNTs. The last significant scattering band is the 2D-band, it is also commonly referred to as G'-band. The 2D-band is the second overtone of the defect band that occurs at ~2720 cm^{-1} through a double resonance scattering process[41]. The 2D-band is useful to distinguish between the presences of graphene from that of graphite. In graphite there is a shoulder that is present at ~2698 cm^{-1} and for graphene the shoulder is not present[101], this concept is presented in Figure 3.19. The intensity ratio of I_{2D}/I_G band is used to quantify the numbers of layers in graphite. In CVD graphene an I_{2D}/I_G of 2 or higher usually corresponds to single layer graphene.

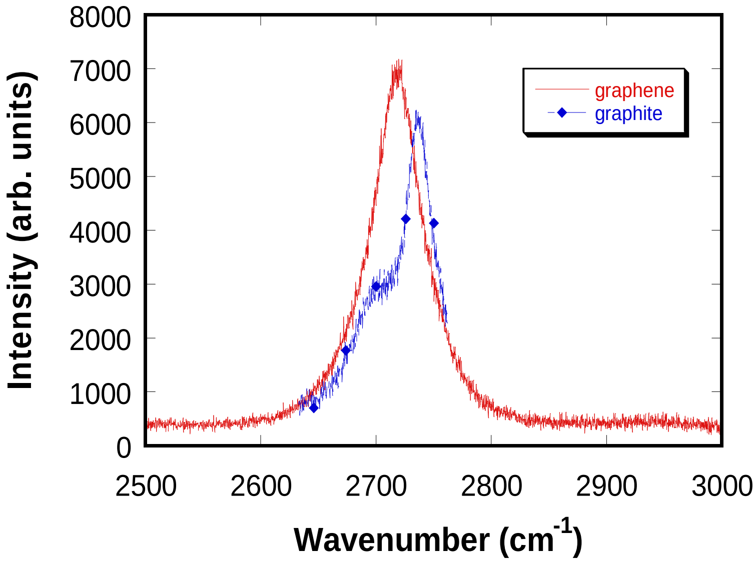

Figure 3.19 Raman measurements comparing the 2D peak's of a graphene and graphite sample.

3.7 Conductive-Tip Atomic Force Microscopy Methodology

To measure local electrical conductivity of nanotube networks a conductive-tip atomic force microscopy (C-AFM) tool was utilized. The principal of operation of C-AFM is to apply a voltage through a conductive tip that is being raster scanned for a small area, on the order of microns. As the conductive tip comes into contact with the sample, a current in response to the applied voltage is measured. After the scan has completed, an electrical current map for the local area that was scanned is produced. This electrical conductivity map is useful to determine the electrically active uniformity and the extent of electrical activity in the material.

As-made M-SWNT and Sc-SWNT electrodes were initially shipped to the Dr. Neal Armstrong research group at the University of Arizona and conductive-tip atomic force microscopy (C-AFM) measurements were performed by Gordon MacDonald. On a later date a trip was made to the University of Arizona to investigate the "electrical conductivity maps" of SWNT electrodes for dedoped SWNT electrodes, equivalent to as-made electrodes with surfactants removed to a high degree, and HNO_3 doped SWNT electrodes.

Prior to traveling the University of Arizona the SWNT electrodes were deposited onto glass and were cut in half with a Universal Laser System M-360 laser cutter. Where one half was treated with nitric acid and then dedoped by annealing on top of a covered hot plate at 200°C overnight and the other half was left as prepared. The prepared SWNT electrodes were exposed to air for at least six days prior to be measured with the C-AFM instrument at the University of Arizona by Gordon MacDonald. The electrodes were exposed to air for at least 6 days prior to be measured so that the electronic properties of the electrodes could have enough time to stabilize as was shown by Jackson[20]. Where, Jackson demonstrated that it takes ~150 hours for SWNTs to stabilize from unintentional doping from exposure to air via oxygen adsorption.

To minimize experimental error 200nm of silver metallic fingers were deposited, via electron-beam (e-beam) vapor deposition, on SWNT electrodes prior to being measured with the C-AFM instrument. Measurements were taken ~500nm away from the Ag electrode tip to avoid contact with residually diffused Ag nanoparticles. This was done to reduce error due to shorts in the electronic pathways of the nanotube networks caused by insufficient conductive intercalation pathways from the lack of metallic SWNTs.

First, silver metallic fingers were deposited on the dedoped SWNT electrodes, while the as-made SWNT (other half) electrode was doped with HNO_3. C-AFM measurements were then initially performed on the dedoped SWNT electrodes. Afterwards, 200nm of silver was deposited on the doped SWNT electrode and then the doped SWNT electrode was measured with the C-AFM instrument in the afternoon (~4-5 hours after being doped).

3.8 Surfactant Removal and Detection Techniques

This section presents techniques employed to remove the surfactants sodium dodecyl sulfate (SDS) and sodium cholate (SC); along with the detection of surfactants via x-ray photoelectron spectroscopy (XPS). Primarily nitric acid treatments and thermal treatments in inert argon environments were utilized for surfactant removal.

3.8.1 Nitric Acid Doping of Carbon Based Nanomaterials

15.8M nitric acid was purchased from Fisher Scientific for the purpose of doping CBN electrodes. First, the CBN electrode was annealed at 90°C for 10 minute to remove residual adsorbed oxygen for a more efficient doping treatment. Next, the CBN electrode was given ~10 minutes to cool to room temperature. Failure to allow the CBN electrode to cool would result in the CBN electrode lifting off, when treated with HNO_3. The next step was to measure 50ml of HNO_3 in a clean beaker. Then the 50ml of HNO_3 was carefully poured into a Petri dish. The CBN electrode was then carefully inserted at a ~45° angle into the HNO_3 bath with acid proof Waf-O-Grip tweezers. The CBN electrode was left in the HNO_3 bath for 45 minutes to dope. Afterwards, the CBN electrode was carefully removed with the acid proof tweezers and was slowly dried with a nitrogen gun. It is emphasized that the CBN electrode had to be handled very carefully, because any abrupt movements would easily cause the electrode to crack or to partially lift off. Finally, the CBN electrode was placed on top of a hot plate at 80°C for 2 minutes to evaporate any residual HNO_3 molecules and to prevent the electrode from becoming “foggy”; which would skew UV-Vis-NIR measurements.

3.8.2 Annealing Experimental Procedures

Annealing studies were performed using a Thermo Fisher Scientific Thermolyne 59300 High Temperature Tube Furnace connected to a Franklin Electric vacuum pump with 1.5hp, voltage rating of 115/208V and model # 1201006405. The pressure was monitored with a Duniway Stockroom Corp. Digital Thermocouple readout, Model #DTC-531-115-BX. The digital thermocouple readout was capable of measuring pressures within the 2mTorr to 2Torr range. Furthermore, a foreline trap manufactured by Key High Vacuum Products Inc. with model # LNT-6-150-K was used to cool down, with liquid nitrogen, heated Ar before it was exhausted into the vacuum pump. This was done specifically to help extend the lifetime of the vacuum pump and had no impact on the annealing experiments.

A picture of the vacuum annealing setup is shown below in Figure 3.20, where the top portion of the annealing setup consisting of the furnace, the pressure meter and the foreline trap are shown in Figure 3.20a and the connected vacuum pump is shown Figure 3.20b. In all of the annealing experiments presented in chapter 4 and 5, 500 standard cubic centimeters per minute (SCCM) of Ar were flowed through the quartz tube. Furthermore, the quartz tube was inserted two inches away from the vacuum seal as shown in Figure 3.20 and all samples were placed 15 inches from the right tip of the quartz tube. This was done to ensure consistent thermal conditions for all annealed samples. The time was measured one hour from when the furnace temperature readout displayed the desired temperature with a timer. After the annealing time had expired, the quartz tube was pulled out to expose the annealed CBN electrode to room temperature, where the sample was cooled to room temperature over a period of ~20 minutes.

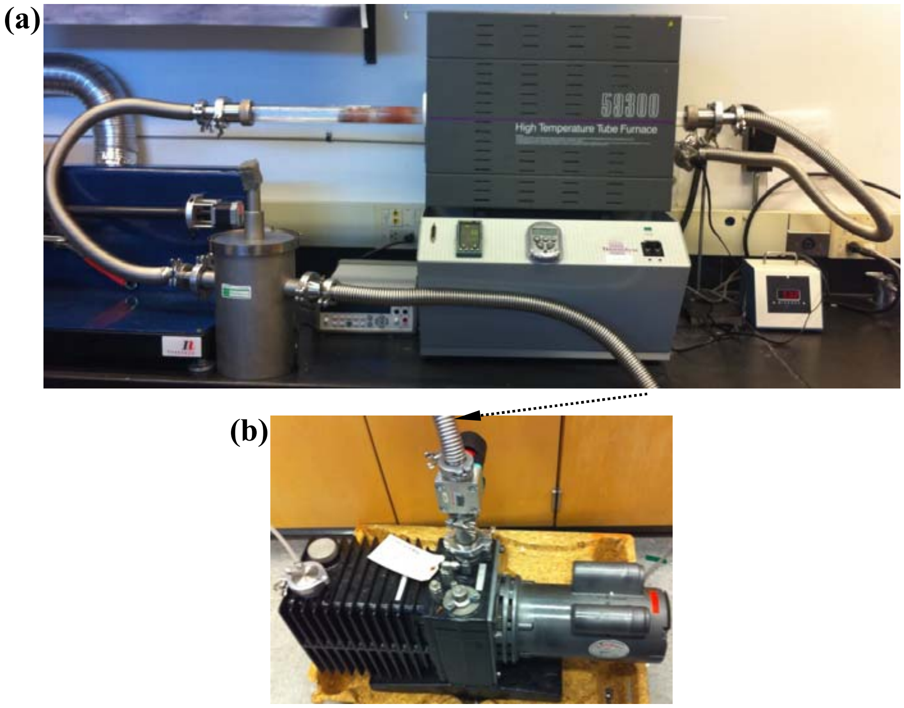

Figure 3.20 (a) Thermo Fisher Scientific Thermolyne 59300 High Temperature Tube Furnace. (b) Franklin Electric Vacuum pump, 1.5hp, 115/208V, model # 1201006405.

3.8.3 Detection of Sodium via X-Ray Photoelectron Spectroscopy

To ensure the complete removal of surfactants SDS and SC, X-ray photoelectron spectroscopy (XPS) studies were performed. XPS is a quantitative spectroscopy technique used to measure the elemental composition of samples. In a primitive sense, the principle of operation of XPS is to bombard a sample with X-rays at varying energies, where the kinetic energies of the electrons escaping from the top 1 to 10nm of the material are measured with a detector. As most elements and compounds have well documented binding energies, the element or compound to which the detected emitted electron belonged to can be readily determined. As the surfactants SDS and SC are organic compounds, the only distinguishable element that can indicate the removal of the surfactant is sodium (please refer to Figure 2.6). As such the XPS plots presented in this work will only correspond to the Na 1s core peak, because this study is only interested in the removal of surfactants. Furthermore, to minimize experimental error, XPS scans were done on at least 3 spots on each sample, were all of the measured spots had to yield consistent results in order to be accepted and presented in this work. All XPS measurements were performed by Dr. Anuradha Bulusu[102], with a Thermo K-Alpha XPS system with a detection limit of ~0.1 atomic percentage, on samples prepared by the author. XPS spectra indicating the presence or absence of surfactant through examination of the Na 1s core peak are shown in Figure 3.21a and b, respectively.

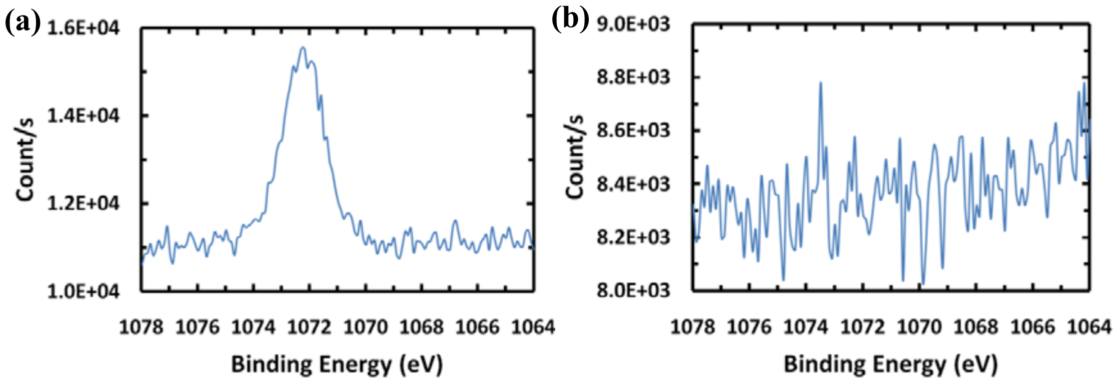

Figure 3.21 (a) XPS spectra of well defined Na 1s peak indicating the presence of the surfactant SDS for an as-made mixed SWNT film. (b) XPS spectra of a non-existent Na 1s peak for an HNO_3 dedoped mixed SWNT film indicating the absence or removal of the surfactant SDS[102].

It should be noted that the Na 1s core peak for sodium cholate is not easily detected via XPS and as such an indirect approach through comparison of sheet resistances is employed to track SC's removal. The removal of the surfactant sodium cholate will be explained in more detail in chapter 4.

3.8.4 Experimental Overview

The impact of surfactants was first investigated with a C-AFM instrument (all measurements were taken by Gordon MacDonald at the University of Arizona) to determine the extent to which insulating surfactants SDS and SC degraded the electrical performance of SWNT electrodes at the nanoscale. For the C-AFM measurements the electrical conductivity maps were compared for as-made, dedoped, and HNO_3 doped metallic (and semiconducting) SWNT electrodes.

Afterwards the removal of the surfactants was investigated via XPS measurements to detect the removal of the Na 1s core peak from sodium containing surfactants SDS and SC (recall Figure 2.6). As-made, HNO_3 doped, and Ar annealed carbon based nanomaterial electrodes were utilized to track the presence and the removal of the Na 1s core peak. It is pointed out that mixed SWNTs were dispersed with only the surfactant SDS; M-SWNTs and Sc-SWNT were dispersed by Nanointegris with surfactant ratios of SDS to SC of 3:2 and 1:4[62], respectively; and graphene puresheets(GPS) were dispersed solely with the surfactant SC. For a summary of this see Figure 3.1. The identification of what surfactants each of the CBN solutions were dispersed with is crucial for the discussion of the removal of surfactants in Chapter 4.

3.9 Conclusions

This chapter discussed the relevant fabrication and characterization techniques need for the discussions in Chapter 4 and 5. The important topics covered in this chapter are summarized below.

Section 3.1 discussed the dispersion of Mixed SWNTs in aqueous solutions through the use of the surfactant SDS and bath sonication. With the exception of graphene oxide, all other CBN solutions used in this work were bought in solution form from Nanointegris who supplied M-SWNTs, Sc-SWNTs, and graphene puresheets. The dispersion of graphene oxide is left for Chapter 5. Section 3.3 discussed the Vacuum filtration technique and the process to transfer films to substrates, which were utilized to fabricate CBN electrodes in this work.

Section 3.4 explained sheet resistance and contact resistance and discussed the transfer length method (TLM). The reliability of the transfer length method was discussed. Section 3.5 discussed the principle of operation of UV-Vis-NIR spectroscopy and the presence of the S_{11}, S_{22}, and M_{11} absorption peaks in the spectra. A validation that the absorption peaks present in the spectra were in fact S_{11} , S_{22}, and M_{11} was done through the use of the Katuara plots[98] and the equation of the energy of a photon. Section 3.6 presented the principle of operation of Raman spectroscopy and discussed how graphene and SWNTs main resonant peaks, G-band, D-band, and 2D-band were helpful in evaluating the quality of the CBN electrodes produced. The intensity ratio I_G/I_D was presented to qualitatively evaluate the structural quality of CBN electrodes by comparing the intensity of the graphitic peaks against the defect peaks.

Section 3.7 discussed the experimental methodology used to characterize SWNT electrodes with a conductive-tip atomic force microscopy tool. Section 3.8 discussed surfactant removal and detection techniques. In particular, the experimental procedure used to dope CBN electrodes with nitric acid and thermal treatments in Ar environments to remove surfactants were presented. Finally, the use of x-ray photoelectron spectroscopy to detect surfactants was explained.

The upcoming chapters 4 and 5 represent the research contribution in this work. Chapter 4 begins by investigating the impact of surfactants on electrode performance. Chapter 4 follows up by determining the effectiveness of chemical and thermal treatments in removing insulating surfactants. Will use UV-Vis-NIR spectroscopy heavily to qualitatively describe what is happening to the SWNT electrodes after thermal annealing and chemical doping processes. Thereafter, chapter 4 continues with a discussion of the effects of annealing on the optoelectronic properties on mixed SWNTs, Sc-SWNTs, and M-SWNTs. Chapter 5 presents work done on graphene SWNT composites; and discusses how the I_G/I_D was found to be useful in describing what occurred when samples were annealed to 1000°C with a suspected slight oxygen leak that made the SWNTs and reduced GO SWNT electrodes more transparent.

CHAPTER 4 : IMPACT OF SURFACTANT REMOVAL ON ELECTRODE PERFORMANCE

4.1 Introduction

In this chapter the impact of surfactant removal on electrode performance is investigated. The surfactant sodium dodecyl sulfate (SDS) is known to be completely removed through nitric acid treatment[42]. However, methods to remove the surfactant sodium cholate (SC) adsorbed onto the surface of carbon based nanomaterials are not as clear in literature.

Knowing that the surfactant SDS is removed through nitric acid treatment, the extent to which the insulating surfactant sodium dodecyl sulfate (SDS) degrades the electronic performance of SWNT electrodes was investigated. This was done through C-AFM measurements, by comparing the electrical conductivity maps of as-made, nitric acid doped, and dedoped SWNT electrodes.

Chapter 4 continues by determining the optimal method to remove the surfactant sodium cholate (SC), either through nitric acid treatment or thermal treatment in an Ar environment. It was determined that the presence of the Na 1s core peak via XPS from sodium cholate could not be detected. To remedy this, the removal of surfactant SC was inferred through comparisons of the sheet resistances of as-made, HNO_3 doped, and Ar annealed graphene puresheets electrodes; as the removal of the surfactant would present noticeable improvements in sheet resistance. Furthermore, the graphene puresheets electrodes (to the knowledge of the author) were not reported to be functionalized and therefore dedoping effects through thermal annealing were considered to be negligible. Thus, allowing the removal of the surfactant SC to be inferred.

It was determined that the surfactant SC is more effectively removed through thermal treatments at 1000°C in an Ar environment. Furthermore, it was determined that the surfactant SDS was also completely removed through thermal treatments at 1000°C in an Ar environment. Thus, the remainder of this chapter is dedicated to studying the behavior of carbon based nanomaterials in response to thermal treatments from temperatures of 400°C to 1000°C.

The concept of the competing effects between interparticle resistances and intraparticle resistances for thermally treated electrodes discussed in section 2.6; was utilized heavily to understand the impact of surfactant removal. The effects of annealing in an Ar environment as a function of temperature were investigated for M-SWNTs, mixed SWNTs, and Sc-SWNTs. For the annealing studies the removal of surface functional groups was heavily investigated through UV-Vis-NIR spectroscopy measurements by observing changes in the S_{11} and S_{22} absorption peaks. The S_{11} and S_{22} absorption peaks were present in varying degrees in the UV-Vis-NIR spectra of M-SWNTs, mixed SWNTs, and Sc-SWNTs due to concentrations of Sc-SWNTs of <5%, ~67%, and >95%, respectively. Finally, the healing of defects in the annealed carbon based nanomaterial electrodes was not considered due to Raman spectroscopy measurements yielding no increases in the I_G/I_D; for samples annealed in Ar environments up to temperatures of 1000°C.

4.2 Impact of Surfactants on CNT Networks by C-AFM Analysis

Electrically insulating surfactants are necessary for dispersing SWNTs in DI water for the purpose of fabricating macroscopically uniform films through various deposition techniques including vacuum filtration, ultrasonic spray coating, spin coating, and ink jet printing. However, surfactants are not easily removed and remain adsorbed on the surface of SWNT electrodes, even after being thoroughly rinsed with DI water. The insulating surfactants that remains adsorbed on SWNT electrodes limit nanotube-nanotube contact, degrade electrical conductivity, and contribute to increased surface roughness. An example of a 50μm x 50μm AFM scan of an as-made M-SWNT electrode film is presented in Figure 4.1. Where numerous tall "islands" are present that may be partially due the presence of surfactants, organic buildup, and dust. This makes it difficult to perform C-AFM measure of as-made samples.

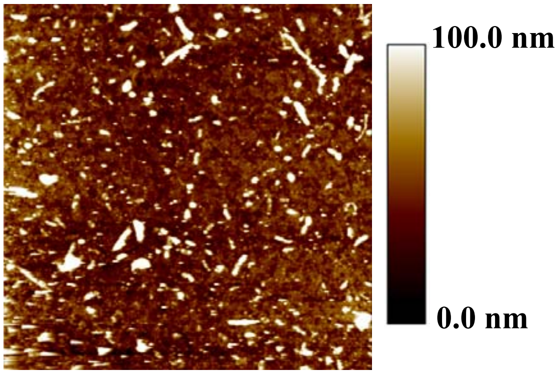

Figure 4.1 50µm x 50µm AFM scan of an as-made metallic SWNT electrode. Image taken in collaboration with the Dr. Neal Armstrong research group at the University of Arizona.

Besides contributing to the surface roughness of randomly oriented nanotube networks and increasing sheet resistance; surfactants negatively impact the electrical performance at the nanoscale. To illustrate this point, conductive tip atomic force microscopy (C-AFM) scans were performed on the as-made M-SWNT and Sc-SWNT electrodes as shown in Figure 4.2b and d, respectively. Furthermore, the corresponding tapping mode scan for an as-made M-SWNT and Sc-SWNT electrode are presented in Figure 4.2a and c, respectively.

As can be seen in Figure 4.2 the as-made M-SWNT and Sc-SWNT films have relatively few electrically active spots and a much larger proportion of electrically inactive or "dead" spots. The significance of these dead spots, which are largely due to the presence of insulating surfactants, is that they present potential barriers for charge carriers conducting through the nanotube network. This ultimately has a negative impact on the electrical properties of the nanotube network at both the nanoscale and macroscale. At the macroscale the sheet resistance suffers as a result of the insulating surfactants hindering electrical conduction by increasing interparticle resistances. At the nanoscale these electrically inactive dead spots are detrimental to the performance of organic electronics such as, OPVs and OLEDs.

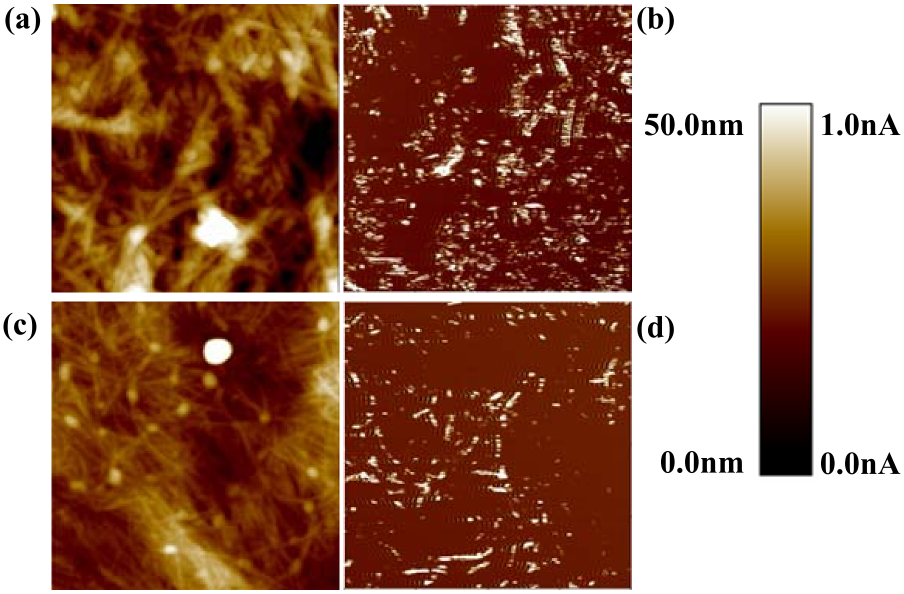

Figure 4.2 (a) 1µm x 1µm AFM scan of as-made metallic SWNT film in Tapping Mode. (b) C-AFM scan of As-made Metallic SWNT film. (c) 1µm x 1µm AFM scan of As-made Semiconducting SWNT film in Tapping Mode. (d) C-AFM scan of As-made Semiconducting SWNT film. +10mV bias was used. Images taken in collaboration with the Dr. Neal Armstrong research group at the University of Arizona.

For OPVs the electrically dead spots may decrease the power conversion efficiency of OPVs, by hindering charge carrier transport via "redirection" of charge carriers at the nanoscale. This concept can be better understood by recalling the principle of operation of an OPV (Figure 1.5). If a hole, from a successfully dissociated exciton at the acceptor/donor heterojunction, diffusing to the positive electrode encounters a dead spot it would be redirected to an active area. This redirection of holes increases its recombination probability in the donor layer, which would reduce the overall power conversion efficiency.

Similarly it can be argued that for OLEDs, when a voltage is applied across the device, the electrically inactive dead spots will hinder the injection of holes through the

SWNT positive transparent electrode into the transport layer. The decrease in efficiency of injecting holes into the transport layer would likely decrease the recombination probability (i.e. light generated through electroluminescence or the generation of excitons that emit light in the form of photons) at the transport and emissive heterojunction. This would require more power input to achieve comparable light output for the same SWNT electrode with surfactants completely removed. In other words, it would reduce the lumens per watt efficacy.

Therefore, surfactants contribute to the surface roughness of TCE films and negatively impact the electrical conductivity at the macroscopic scale and nanoscale, due to their insulating nature and forcing charge carriers to be "redirected", respectively. Fortunately, surfactants can be removed through chemical treatment and/or thermal treatment, as will be discussed in the remainder of this chapter.

4.2.1 Post Acid Treatment C-AFM Analysis

Recalling Figure 4.2 where it was shown that surfactants contributed to electrically inactive "dead spots" due to their insulating nature. Nitric acid treatment has been shown to remove the surfactant SDS and to densify films to create more nanotube contacts[42]. As a result of 15.8M Nitric acid treatment for 45 minutes the nanoscopic electrical properties of as-made M-SWNT and Sc-SWNT films were dramatically improved as is shown in Figure 4.3 and Figure 4.4, respectively. In Figure 4.3b and d the increase in electrical activity for the doped and dedoped M-SWNT electrodes is immediately apparent, with peaks in current rising from 1.0nA for the as-made case to 100nA for the doped and dedoped samples. Closer inspection of Figure 4.3b and d demonstrates that the nanoscopic electrical conductivity of the doped and dedoped M-SWNT electrodes are comparable. However, for unknown reasons at the time this thesis was written the dedoped electrode is noticeably more electrically active. Further research needs to be performed to determine the specific cause.

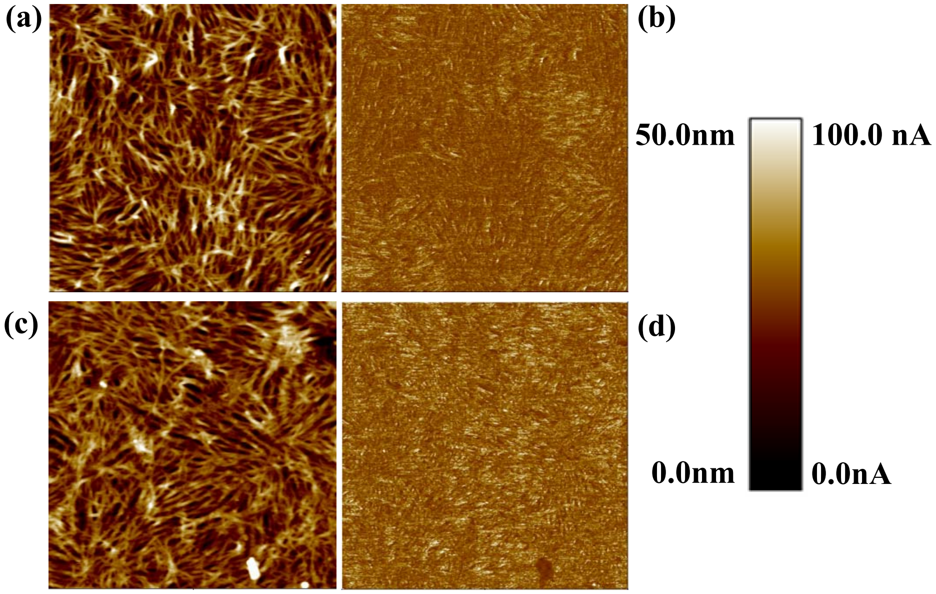

Figure 4.3 (a) 1μm x 1μm AFM scan of nitric acid doped metallic SWNT Film in tapping mode. (b) C-AFM scan of nitric acid doped metallic SWNT film on same spot as tapping mode. (c) 1μm x 1μm AFM scan of dedoped metallic SWNT Film in tapping mode. (d) C-AFM scan of dedoped metallic SWNT film on same spot as tapping mode. +10mV bias has been used. Images taken in collaboration with the Dr. Neal Armstrong research group at the University of Arizona.

The semiconducting SWNT electrodes also exhibited a dramatic increase in nanoscopic electrical conductivity after 15.8M nitric acid treatment for 45 minutes as shown in Figure 4.4. However, the Sc-SWNT electrode's nanoscopic electrical conductivity is inferior to that of the M-SWNT electrodes. This suggests that the Sc-SWNT electrodes need to be p-doped further through thionyl chloride ($SOCl_2$) treatment, in order to have comparable or superior electrical conductivity than M-SWNT electrodes as suggested by Jackson et al. and Blackburn et al. [66, 67]. In this work, p-doping through $SOCl_2$ treatment was not conducted due to limited access to laboratories that are adequately equipped to allow usage and storage of the chemical. As such C-AFM studies for M-SWNT and Sc-SWNT doped with HNO_3 and $SOCl_2$ is left for future work.

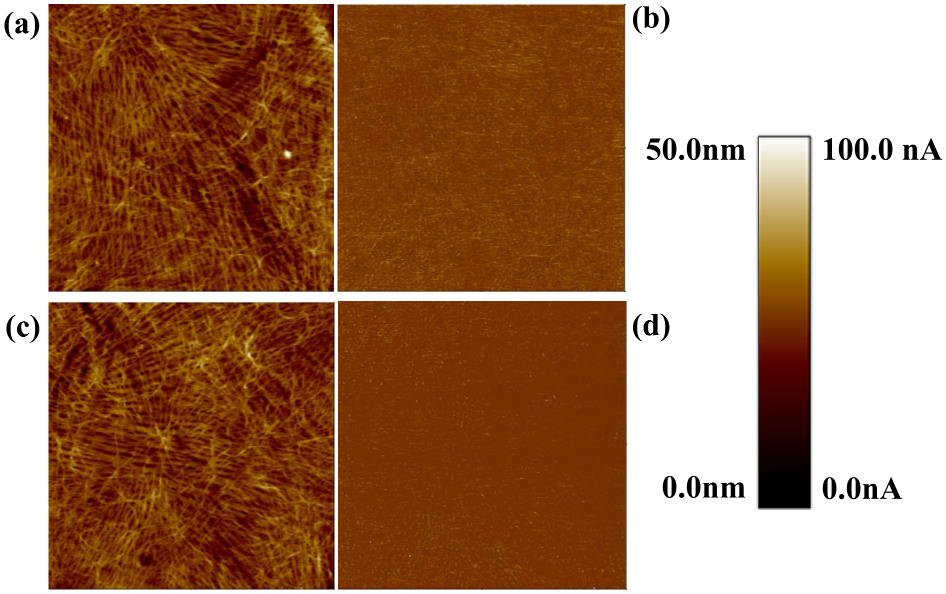

Figure 4.4 (a) 1µm x 1µm AFM scan of nitric acid doped semiconducting SWNT film in tapping mode. (b) C-AFM scan of nitric acid doped semiconducting SWNT film on same spot as tapping mode. (c) 1µm x 1µm AFM scan of dedoped semiconducting SWNT Film in tapping mode. (d) C-AFM scan of dedoped semiconducting SWNT film on same spot as tapping mode. +10mV bias has been used. Images taken in collaboration with the Dr. Neal Armstrong research group at the University of Arizona.

4.3 Assessment of Surfactant Removal

To ensure the complete removal of surfactants SDS and SC, X-ray photoelectron spectroscopy (XPS) studies were performed. For information on XPS please review section 3.8.3.

4.3.1 Removal of Surfactant Sodium Dodecyl Sulfate

The removal of the surfactant SDS was first investigated by comparing an as-made mixed SWNT film (dispersed only with SDS), that had been thoroughly rinsed with DI water and a HNO_3 dedoped mixed SWNT film (both films were fabricated via the vacuum filtration method). Mixed SWNTs were chosen for this study because they are the only carbon based nanomaterial that the surfactant used for solution processing can be chosen by the author. The other solutions were already dispersed in surfactants predetermined by vendor Nanointegris.

It is well known that rinsing SDS dispersed SWNT films with DI water can help remove the surfactant. However, it is not definitively certain whether the SDS is completely removed. Thus, to test this hypothesis the as-made film that has been thoroughly rinsed with DI water will be characterized for the presence of the surfactant via XPS. Furthermore, as it has already been shown that the use of HNO_3 is effective in removing SDS [42], this experiment will be useful in showing the validity of this approach. The results of this experiment are shown in Figure 4.5a and b. Where the XPS spectra obtained from the as-made and HNO_3 dedoped mixed SWNT films strongly suggest the presence of SDS and the removal of SDS, respectively.

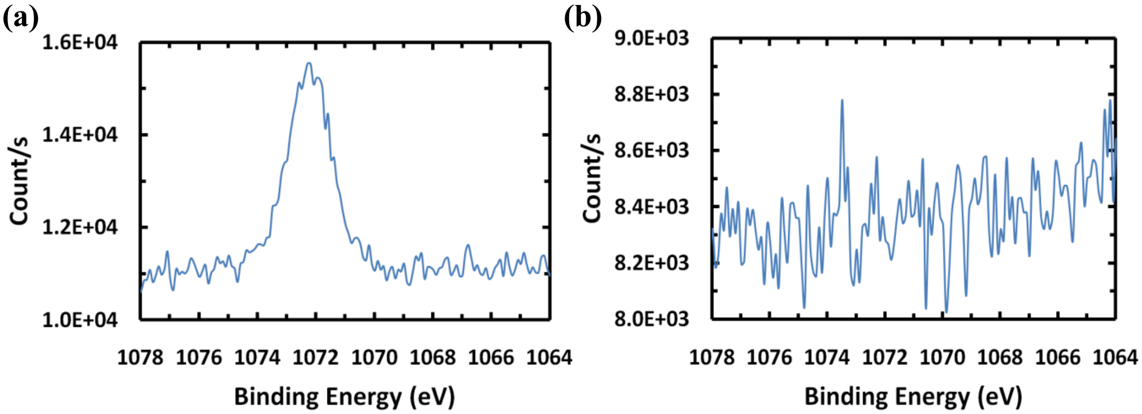

Figure 4.5 (a) XPS spectra of Na 1s peak for as-made mixed SWNT film that has been thoroughly rinsed with water. (b) XPS spectra of Na 1s peak for HNO_3 dedoped mixed SWNT film. The removal of the Na 1s core peak is a clear indication of the removal of the surfactant SDS[102].

The removal of SDS has been demonstrated and is in agreement with literature[42]. It is of interest to determine if thermal annealing in an inert environment such as Ar is also effective in removing this surfactant. For the next experiment an as-made M-SWNT thoroughly rinsed with DI water and an M-SWNT film annealed in an

Ar environment at 1000°C for 1 hour are characterized with XPS. The difference in this scenario is that M-SWNTs are dispersed using both SDS and SC by vendor Nanointegris. Inspection of the XPS spectra of the as-made and Ar annealed sample in Figure 4.6, suggests that both surfactants have been removed. Although, this assumption turns out to be very likely true, as will be demonstrated later in this chapter, the ability of the XPS tool to detect Na in sodium cholate has not yet been demonstrated. Without demonstrating that the XPS tool can detect Na from SC it cannot yet be concluded that the surfactant SC was in fact removed. Thus, it can only be concluded at this point that SDS has been removed through annealing in an Ar environment at 1000°C.

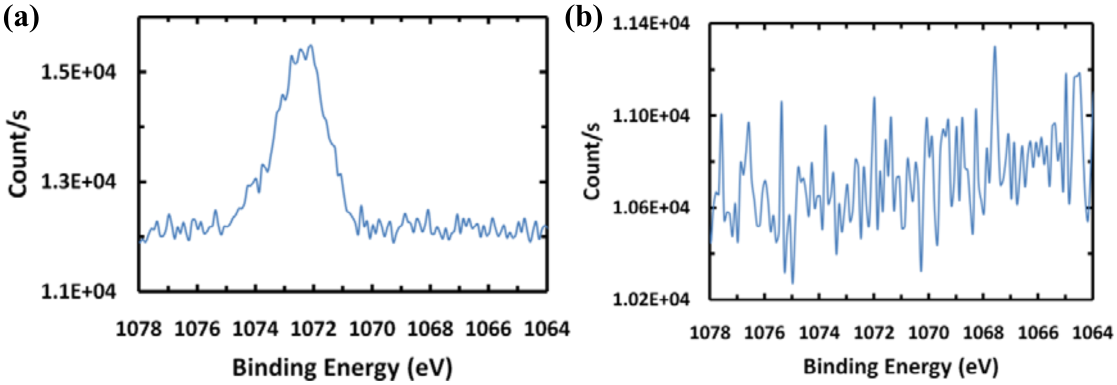

Figure 4.6 (a) XPS spectra of Na 1s peak for as-made M-SWNT film. (b) XPS spectra of Na 1s peak for M-SWNT film annealed at 1000°C in an Ar environment [102].

4.3.2 Removal of Sodium Dodecyl Sulfate as a Function of Temperature

In order to better understand the affects of annealing on SWNT electrodes, the removal of surfactant SDS as a function of temperature was investigated through XPS. For the as-made M-SWNT sample a very low average atomic percentage of Na is detected at 0.37%[102]. This low atomic percentage is within the detection limits of the Thermo K-Alpha XPS, so it is safe to assume that surfactants are still present on the thoroughly rinsed electrodes. Furthermore, type-sorted SWNTs are reported to be dispersed in a 3:2 and 1:4 ratio of SDS to SC for M-SWNT and Sc-SWNT solutions, respectively[62]. The detection of Na in XPS scans is suspected to be solely due to the presence of SDS, as discussed earlier it has been observed in literature that the Na 1s core peak for SC is not detectable through XPS[103].

For the 400°C Ar annealed sample out of three XPS scans only one scan detected Na at an atomic percentage of 0.14[102]. For the 600°C and 1000°C Ar annealed samples, the Na 1s core peak was not detected in any of the XPS scans[102]. This suggests that at 400°C the surfactant SDS is removed to a high degree but not entirely as the Na 1s core peak was detected in at least one XPS measurement. At 600°C and a 1000°C it can be said the surfactant SDS has been removed to an extremely high degree, if not completely removed. From this XPS study it is clearly seen that as the annealing temperature is increased the amount of the surfactant, SDS, which is removed increases as well. It is suspected that SDS is fully removed at annealing temperature of 600°C.

4.3.3 Removal of Surfactant Sodium Cholate

To determine if the Na 1s core peak in the surfactant sodium cholate can be detected with the XPS tool, an as-made graphene puresheets(GPS) film, dispersed only with SC, was scanned at multiple spots. Surprisingly, the result shown in Figure 4.7 is that Na 1s core peak was not detected in the XPS spectra. However, it is highly likely that the surfactant is still present on the GPS film as no treatment other than thoroughly rinsing with DI water has been performed to remove the surfactant. This assumption is supported by the study of Frank et al.[103], where it was suspected that SC was present on their throroughly rinsed electrodes, even though the presence of Na was not detected in their XPS scans. Currently the reason as to why the Na 1 s core peaks are not detectable through XPS is unclear.

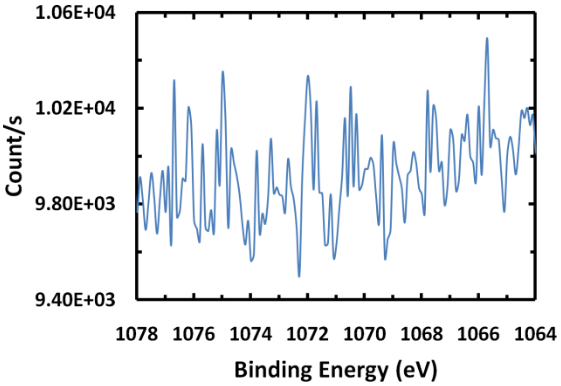

Figure 4.7 XPS spectra of Na 1s peak for graphene pure sheets film. The sodium peak was not detected by the XPS tool for reasons that are currently unknown [102].

Although the Na 1 s core peaks for SC cannot be directly detected through XPS it is still possible to determine the removal of the surfactant sodium cholate indirectly through comparisons of the sheet resistances of as-made, Ar annealed, and HNO_3 doped graphene puresheets (GPS) electrodes. Sheet resistance can give clear indications of the removal of SC because the surfactant is electrically insulating and therefore if the surfactant is removed there should be a noticeable decrease in the sheet resistance of the electrode. Furthermore, the GPS have not been functionalized and therefore should not be heavily doped. However, unintentional doping through exposure to air cannot be completely ruled out, but are considered to have minimal impact on the conductivity of the GPS electrodes when compared to the impact of the removal of surfactants. Moreover, annealing of the GPS electrodes should not shift the Fermi level significantly, because there are no carboxylic functional groups present to dedope the electrodes. As a result it can be inferred that the change in R_{sh} can be used to qualitatively evaluate the extent to which the SC has been removed for Ar annealed films. However, chemically treating graphene with HNO_3 has been shown to p-dope graphene[5]. As a result more caution will need to be taken to evaluate if the surfactant SC has been removed.

To begin the investigation of the removal of the surfactant sodium cholate, an as-made graphene puresheets (GPS), an HNO_3 doped GPS, and an Ar anneal 1000°C GPS transparent electrodes were prepared. The samples were processed from the same solution graphene puresheets research grade batch G10-010R, same vacuum filtration setup (new glass frit), and DI water with resistivity ~16.0MΩ-cm. The sheet resistance and transmittance of each sample was measured and the results are presented in Table 4.1. The results of this experiment suggest that annealing in an Ar environment at 1000°C is the most effective method to remove the surfactant SC. Although it is not currently known if the decrease in R_{sh} for HNO_3 treated GPS electrode is solely due to p-doping or due to removal of the surfactant SC. Further research needs to be conducted to determine this. It is suggested that it may be possible to maximize the conductivity of GPS electrode by annealing in Ar 1000°C followed up by doping in HNO_3.

Table 4.1 Comparison of optoelectronic properties of research grade graphene puresheets.

Graphene Puresheets Research Grade		
Treatment	**R_{sh}**	**Transmittance**
As-Made	13,299Ω/sq	78%T
15.8M HNO_3 **45 minute**	4,148Ω/sq	76%T
Ar Anneal 1000°C **1 hour**	2,416Ω/sq	76%T

It should also be noted that there is a slight drop in transmittance for the annealed and nitric acid doped samples. Although, further research needs to be conducted, this might suggest that densification has occurred due to remnant surfactants between graphene sheets being removed; thereby creating greater overlap between "graphene islands". This would then decrease the transmittance slightly, due to the increase in overlap between graphene sheets. Furthermore, the increase in overlap between graphene sheets would result in more intercalation pathways for current to conduct through. This along with the removal of SC, may have both contributed to the significant drop in sheet resistance observed for the GPS electrodes.

4.3.4 Removal of Sodium Cholate as a Function of Temperature

It has been determined that annealing in an Ar environment at 1000°C for 1 hour is effective at removing the surfactant sodium cholate (SC). The next natural question that arises is whether or not SC can be removed at lower temperatures. Therefore another experiment was conducted by comparing the optoelectronic properties of GPS electrodes annealed in Ar for 1 hour at 600°C and 1000°C. The results are compared in Table 4.2. It is interesting to note the R_{sh} obtained for the Ar Annealed at 1000°C is comparable to that obtained in the previous experiment as presented in Table 4.1. This validates the result obtained previously. However, it should be noted that the transmittance is ~1% less than obtained in the previous experiment. This is suggested to possibly be within the resolution of the instrument, caused by insufficient baseline runs, or dust particles collecting on the electrode that block light as UV-Vis-NIR measurements were not taken in a cleanroom.

Table 4.2 Comparison of optoelectronic properties of research grade graphene puresheets Ar anneal.

Treatment	R_{sh}	**Transmittance**
Ar Anneal 600°C 1 hour	4,654Ω/sq	76%T
Ar Anneal 1000°C 1 hour	2,376Ω/sq	75%T

4.4 Motivation for Annealing Studies

The removal of surfactants has been investigated and it is now of interest to investigate how SWNTs are affected by thermal annealing treatments. It has been shown that thermal treatments are more effective at removing surfactants than nitric acid treatment. However, annealing at temperatures up to 1000°C is likely to remove surface functional groups, including COOH groups that p-dope SWNTs. Therefore, even though the removal of surfactants will effectively improve the conductivity of the SWNTs, the removal of surface functional groups will effectively decrease its conductivity as was discussed in section 2.6. Thus, there is a competing effect between the removal of surfactants and surface functional groups.

It is interesting to investigate if there is an optimal annealing temperature and to determine if the surfactants SDS and SC can be removed to a satisfactory degree at lower temperatures. Furthermore, investigations of healing defects, which is readily determined by the I_G/I_D ratio, at temperatures up to 1000°C in an inert environment , was concluded to not apply within this temperature range. The results of the Raman spectroscopy measurements concluded that there was no increase in the I_G/I_D; thus, suggesting that defects were not healed. This finding is consistent with literature that suggests that temperatures of 1600°C[104], 1700°C[105] and above are needed to heal defects. For this reason, healing of defects is not considered to any extent in the following discussion.

This annealing study was not performed on the graphene puresheets as it was not specified to be functionalized and thus it was only of interest to investigate the removal of surfactant SC for the GPS electrodes. Also it is important to note that while the importance of this study can be questioned on the grounds that conductive plastic substrates needed for organic electronics cannot survive such high temperature; this concern can be remedied with a technique known as Rapid Thermal Annealing (RTA).

RTA can heat CBN electrodes at high temperatures for a sufficiently short time period such that the plastic substrate will be left unharmed. RTA studies are left for future work.

4.5 Effects of Annealing of Metallic Carbon Nanotube Networks

It was shown by Jackson[20] that annealing SWNTs in vacuum at 200°C overnight would dedope SWNTs. This fact was apparent in Jackson's UV-Vis-NIR spectra that showed an increase in the intensity of the absorption peaks, most notably the S_{11} and S_{22} absorption peaks. This increase in intensity of the absorption peaks is due to the removal of surface functional groups that p-dope SWNTs. The removal of surface functional groups injects electrons back into the density of states, thereby effectively shifting the Fermi level up and intensifying the S_{11} and S_{22} absorption peaks. This concept was thoroughly explained in section 3.5. Similarly, annealing in an inert environment such as Ar should have a similar effect on the absorption peaks. However, it is not know if annealing at higher temperatures will cause an even greater increase in the intensity of the absorption peaks.

To begin this study, two M-SWNT films were vacuum filtered and were labeled as film A and B. Film A was cut in half and the halves were labeled A1 and A2, were they were transferred onto quartz. Film A1 was left as made and film A2 was annealed in an Ar environment at 400°C for 1 hour. Film B was also cut in half, were the halves B1 and B2 were annealed at 600°C and 1000°C in an Ar environment for 1 hour, respectively. Furthermore, the furnace's pressure was monitored to ensure that air leaks were minimized during the annealing process. The results of the experiment are presented in Figure 4.8. Careful inspection of the UV-Vis-NIR spectra for films A2, B1, and B2 in Figure 4.8, clearly shows that there is not a noticeable increase in the intensity of the S_{11} and S_{22} absorption peaks.

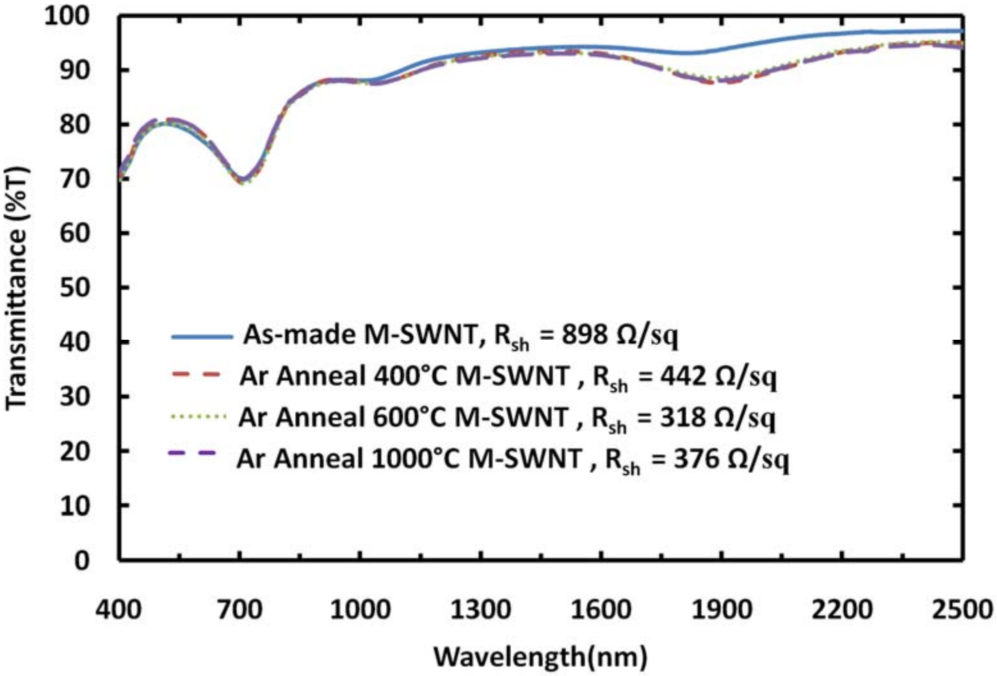

Figure 4.8 UV-Vis-NIR spectra for as-made, Ar anneal 400°C, Ar anneal 600°C, and Ar anneal 1000°C Metallic SWNT electrodes. Sheet resistance for each sample is presented as well.

It is pointed out that the fabricated M-SWNT electrodes have Sc-SWNT absorption peaks present in its UV-Vis-NIR spectra because of Sc-SWNT concentration are <5% in solution, as specified by Nanointegris. Inspecting Figure 4.8 it is easily seen that the M_{11} absorption peak is not sensitive to the removal of surface functional groups, this can be understood by recalling the DOS for M-SWNTs. On the other hand the S_{11} and S_{22} absorption peaks are much more sensitive to the detection of dedoping via the removal of surface functional groups. However, shifts in the absorption peaks observed in the UV-Vis-NIR spectra are not easily detected with M-SWNT electrodes. It is suggested that mixed SWNTs and Sc-SWNTs will be more sensitive to the affects of dedoping as they have higher concentrations of semiconducting nanotubes. Annealing studies for mixed SWNT and Sc-SWNT electrodes will be presented in the next sections.

It is interesting to note that Jackson[20], reported an increase in R_{sh} for a M-SWNT film with ~77% transmittance from 212Ω/sq for an as-made sample to 306Ω/sq for the 200°C annealed sample. Whereas an M-SWNT electrode annealed in an Ar environment at 400°C for 1 hour effectively halves its sheet resistance. Further inspection shows that the 600°C Ar annealed sample experienced an even further decrease in R_{sh} and that the 1000°C Ar annealed sample surprisingly experienced an increase in R_{sh}. Also there was no noticeable change in the transmittance of the four samples. While the results obtained seem at odds with Jackson's work they are in fact not.

The increase in R_{sh} for Jackson's vacuum annealed study is due to the removal of oxygen p-dopants adsorbed onto the surface of the nanotubes. This results in an intensification of the S_{11} absorption peak due to the injection of electrons back into the valence band, thus increasing the number of states available to participate in absorption at the S_{11} peak. Therefore, the number of charge carriers that need to overcome the S_{11} bandgap increases, resulting in a net decrease in conductivity.

In Jackson's study it is presumed that the removal of surface functional groups is dominant over the removal of surfactants. Whereas, the reduction in R_{sh} for the 400°C Ar annealed sample is likely attributed to the removal of surfactants to some degree, dominating over the affect of partially removing surface functional groups and oxygen dopants. This data suggests that at 400°C the surfactants are partially removed and at 600°C the surfactants are removed to a high degree, which is consistent with the study performed in section 4.3.2 and 4.3.4. Furthermore, it is suspected that residual surface functional groups that were not removed after annealing at 600°C were further removed through annealing at 1000°C in Ar for 1 hour. However, the sheet resistance increases for the 1000°C Ar annealed M-SWNT electrode, implying that the removal of surface functional groups may be dominating over the removal of surfactants.

The results obtained for the 400°C and 600°C Ar annealed samples were logical. However, the results obtained for the 1000°C Ar annealed samples need to be reproduced to verify this observation. To this end the experiment was repeated for the 600°C and 1000°C Ar annealed scenarios. The results obtained for the M-SWNT annealing study as a function of temperature are presented in Figure 4.9. It is evident from Figure 4.9 that the results obtained for the 600°C and 1000°C Ar annealed samples are consistent and repeatable.

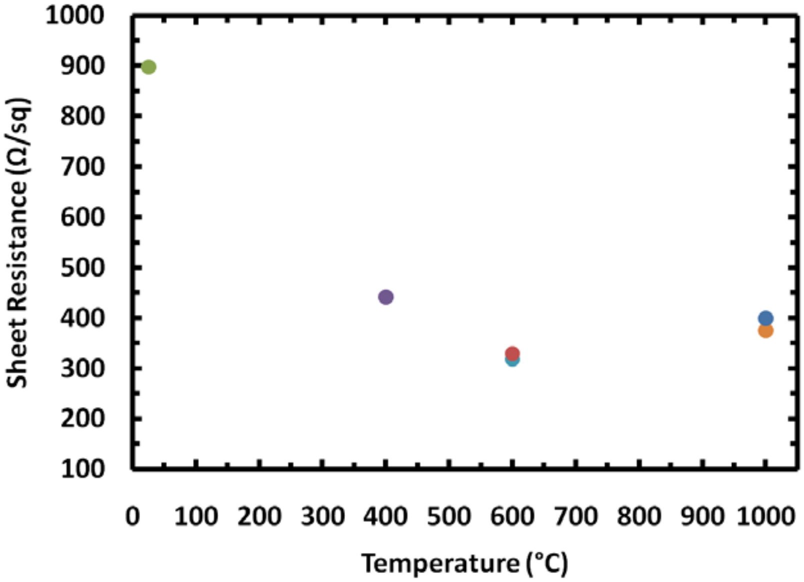

Figure 4.9 Sheet resistance as a function of temperature for M-SWNT electrodes.

4.6 Effects of Annealing of Mixed Carbon Nanotube Networks

To investigate how mixed SWNTs dispersed only with SDS in DI water behave as a function of temperature, two mixed SWNT films labeled A and B were each cut in half and processed in the same manner as described in section 4.6. The results of the first trial are shown in Table 4.3.

For the Ar anneal 400°C mixed SWNT electrode there is a drastic increase in the sheet resistance when compared to the as-made mixed SWNT electrode. Where in this case the intensification of the S_{11} absorption peak reduces the number of available charge carriers for electrical conduction to a heavy degree and dominates over the removal of surfactants, thereby increasing sheet resistance (R_{sh}). Next, for the Ar anneal 600°C mixed SWNT electrode the sheet resistance drops. Thus, implying that the removal of the surfactant SDS is dominant over the removal of surface functional groups for the Ar anneal 600°C mixed SWNT electrode. Finally, for the Ar anneal 1000°C mixed SWNT electrode the sheet resistance slightly increases, which is likely due to the nanotubes being heavily dedoped.

It is noted that the R_{sh} values obtained for the mixed SWNTs are relatively high and the reason why was investigated (see Appendix C). It was found that the nanotubes that were used to prepare the mixed SWNT solution had aggregated to a significant degree while in powder form. Furthermore, XPS analysis also revealed that Fluorine contaminants from Nanointegris' solution had propagated to this solution through the glassware, despite all the glassware thoroughly being cleaned. XPS measurements found that the Fluorine peaks were still present on SWNT electrodes even after annealing at 1000°C in Ar. This strongly suggests that the Fluorine contaminants had formed C-F bonds with the nanotubes most likely through nucleophillic substitution as the electronegativity of Fluorine is 4.0, which is higher than that of the hydroxyl groups at 2.75. The attached Fluorine groups are believed to be the reason as to why the mixed SWNTs were not as heavily dedoped as expected, since the mixed SWNTs should be much more sensitive to dedoping than the M-SWNTs.

Table 4.3 Sheet resistance for mixed SWNT electrodes as a function of temperature.

Treatment	R_{sh} (Ω/sq)
As Made	3,930
Ar Anneal 400°C	5,799
Ar Anneal 600°C	3,982
Ar Anneal 1000°C	4,099

Due to the fear of the Fluorine contaminants and aggregation of the nanotubes skewing results obtained, the experiment was conducted again with a newer P3-SWNT Batch# 03-499 nanotube powder. The UV Vis NIR spectra with corresponding R_{sh} data obtained as a function of temperature are presented in Figure 4.10. The mixed SWNTs behaved in the same manner as in the previous run and a higher increase in R_{sh}, believed to be caused by heavy dedoping, from annealing at 600°C to 1000°C is observed, as expected.

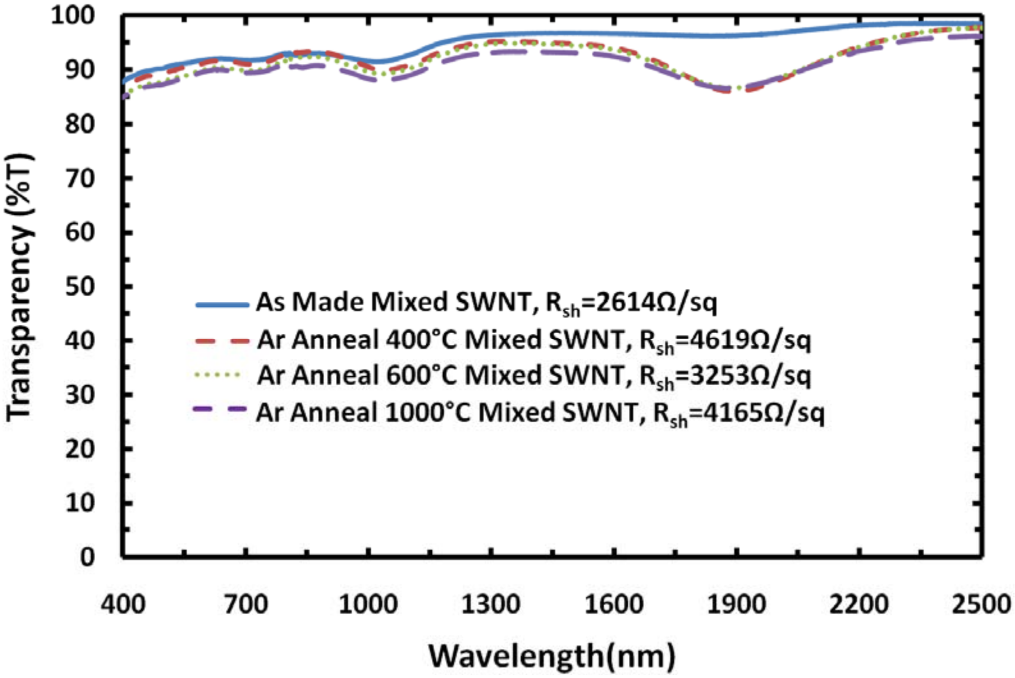

Figure 4.10 UV-Vis-NIR spectra for as-made, Ar anneal 400°C, Ar anneal 600°C, and Ar anneal 1000°C mixed SWNT electrodes. Sheet resistance for each sample is presented as well.

Closer inspection of Figure 4.10 demonstrates that even though it is difficult to distinguish between the intensities in the S_{11} absorption peak between the annealed samples; the S_{22} peak for 1000°C Ar annealed sample is slightly more intense than the other annealed samples. The observation of a more intense S_{22} absorption peak for a 1000°C Ar annealed mixed SWNT, suggests that the driving factor that is causing the nanotube electrodes' R_{sh} to increase from annealing from 600°C to 1000°C is due to heavy dedoping of the nanotubes, as hypothesized. However, the difference in the intensity of the S_{22} absorption peak in the mixed SWNTs is not obvious and can be argued to be due to experimental error or beyond the resolution of the Cary UV-Vis-NIR spectrophotometer. To clear any doubt, an annealing study for Sc-SWNT nanotubes was conducted as it is argued that Sc-SWNT will be much more sensitive to dedoping than the Mixed-SWNTs, because of its higher concentration of Sc-SWNTs. Therefore, validating evidence of heavy dedoping should be present in the UV-Vis-NIR spectra of the Sc-SWNT electrodes.

4.7 Effects of Annealing of Semiconducting Carbon Nanotube Networks

In this section the annealing effects on Sc-SWNTs were investigated and the results obtained in this section were utilized to tie together the observations from section 4.3 and 4.4. The goal of this section is to prove the hypothesis of heavy dedoping of functionalized SWNTs at 1000°C. To this end attention, is focused on the UV-Vis-NIR spectra of Sc-SWNT electrodes annealed in Ar at 600°C and 1000°C as is shown in Figure 4.11, where these two films came from the same membrane. In Figure 4.11, there is a clear shift in the S_{22} absorption peak and a less subtle shift in S_{11} absorption peak for the 1000°C Ar anneal electrode over the 1000°C Ar anneal electrode.

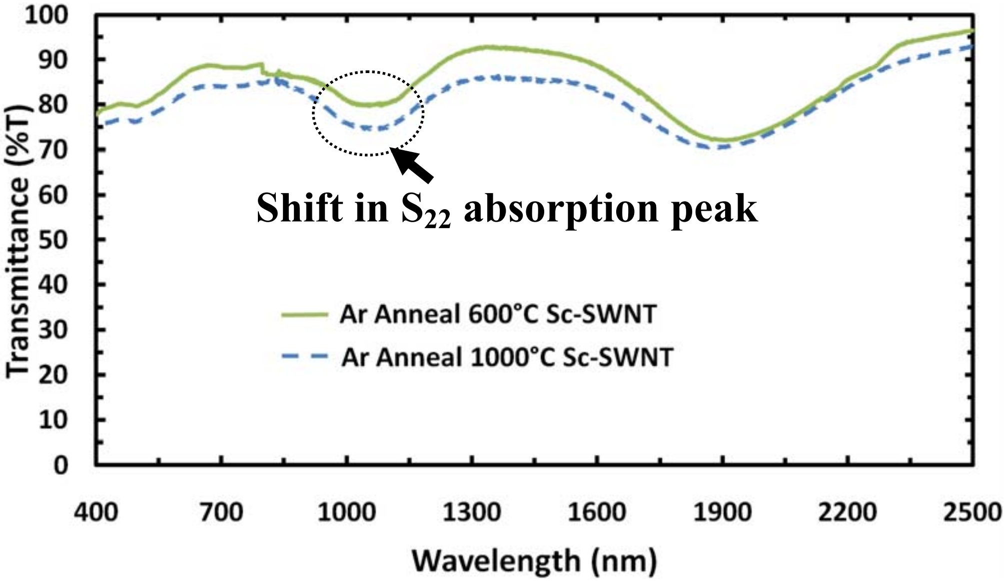

Figure 4.11 UV-Vis-NIR spectra of Ar anneal 600°C and Ar anneal 1000°C semiconducting SWNTs electrodes. There is a clear shift or intensification in the S_{22} absorption peak and a subtle shift in the S_{11} absorption peak.

It could be argued that the films are not exactly the same as the UV-Vis-NIR spectra do not overlap in the visible range (400-700nm) as the M-SWNTs did in Figure 4.8. However, this concern can be remedied by referring back to the Kataura plot [98]. Recalling that the arc-discharge SWNTs used in this work have a mean diameter of 1.4nm, the energy separation for the S_{33} absorption peak can be estimated. There is however a spread in the data points for the S_{33} absorption peak in the Kataura plot, so the energy separation will be assumed to be at the center of the spread of data points. This corresponds to an energy separation of 1.15eV or an energy gap of 2.3eV. Using equation 3.1 to solve for the theoretical wavelength at which the S_{33} absorption peak should present yields equation 4.1 or a wavelength of 539.1nm.

$$\lambda_{S_{33}} = \frac{2\pi\hbar c}{\varepsilon_{S_{33}}} = \mathbf{539.1nm} \tag{4.1}$$

Careful inspection of Figure 4.11 does show that there is an absorption peak present at ~530nm as suggested by theory. Therefore, if there is a shift in the S_{22}

absorption peak due to heavy dedoping there should be also a shift in the S_{33} absorption peak, which there is. However, the shift in the S_{33} absorption peak is not desired as it decreases the transmittance at the 550nm wavelength benchmark.

The study of sheet resistance as a function of temperature for Sc-SWNTs, as was done for M-SWNTs and mixed SWNTs, is presented in Table 4.4**.** The results of the Sc-SWNT annealing are very similar to those obtained for mixed SWNTs, which is expected as mixed SWNTs have ~2/3 Sc-SWNTs. However, the key difference here between the Sc-SWNTs and mixed SWNTs is that the R_{sh} of the Sc-SWNTs is much more sensitive to the removal of surface functional groups, as is expected due to the higher >95% concentration of Sc-SWNTs.

Table 4.4 Sheet resistance for semiconducting SWNT electrodes as a function of temperature.

Treatment	**R_{sh} (Ω/sq)**
As Made	1,933
Ar Anneal 400°C	4,850
Ar Anneal 600°C	3,608
Ar Anneal 1000°C	4,746

It was observed that removing surfactants through thermal annealing for Sc-SWNT electrodes comes at a price, with a drastic increase in R_{sh}. However, it can be argued that if in fact the annealed Sc-SWNT electrodes were dedoped, then they should be capable of being ‘unintentionally” doped; through oxygen dopants adsorbing on the surface of the nanotubes via exposure to air. To investigate if it is possible to redope the nanotubes after annealing, the Ar anneal 600°C and 1000°C Sc-SWNT electrodes were measured after 10 days of exposure to air. An exposure to air for 10 days was chosen as it was shown by Jackson that it takes~150 hours or 6 days for nanotubes to stabilize from unintentional doping. The results are presented in Table 4.5, were after a 10 day exposure to air, a drop in R_{sh} to 36.3% and 29.6% of its original value were observed for the Ar anneal 600°C and Ar anneal 1000°C Sc-SWNT electrodes, respectively.

Table 4.5 Sheet resistance of Ar anneal 600°C and 1000°C semiconducting SWNT electrodes after annealing and post annealing 10 day exposure to air.

Treatment	**After Annealing R_{sh} (Ω/sq)**	**10 Day Exposure to Air R_{sh} (Ω/sq)**
Ar Anneal 600°C	3608	1310
Ar Anneal 1000°C	4746	1404

It is suggested that the Ar anneal 1000°C SWNT electrode recovered its conductivity at a faster rate than the Ar anneal 600°C electrode, because of the greater extent to which the surfactant SC was removed. However, it appears that the recovery in conductivity after annealing at 1000°C for 1 hour is limited, possibly due to potentially irreversible effects of the removal of surface functional groups through exposure to air alone. It is important to note that the R_{sh} for the Ar anneal 600°C and 1000°C Sc-SWNT electrodes exposed to air for 10 days are superior to the as-made Sc-SWNT electrode. This suggests that the negative annealing effects can be remedied through exposure to air and raises the question if it is possible to refunctionalize the carbon nanotubes with carboxylic acid groups. In this regards, due to time constraints a thorough study on the refunctionalization of the nanotubes was not performed in this work and is left as future work (see Chapter 6).

The last topic to be covered in this chapter is to answer if it is better to directly dope as-made Sc-SWNTs with HNO_3 or if it is better to completely remove surfactants by annealing in Ar at 1000°C followed by doping in HNO_3. The results of this study are presented in Figure 4.12 and conclude that Sc-SWNT electrodes are better off to be directly doped with HNO_3 after preparation.

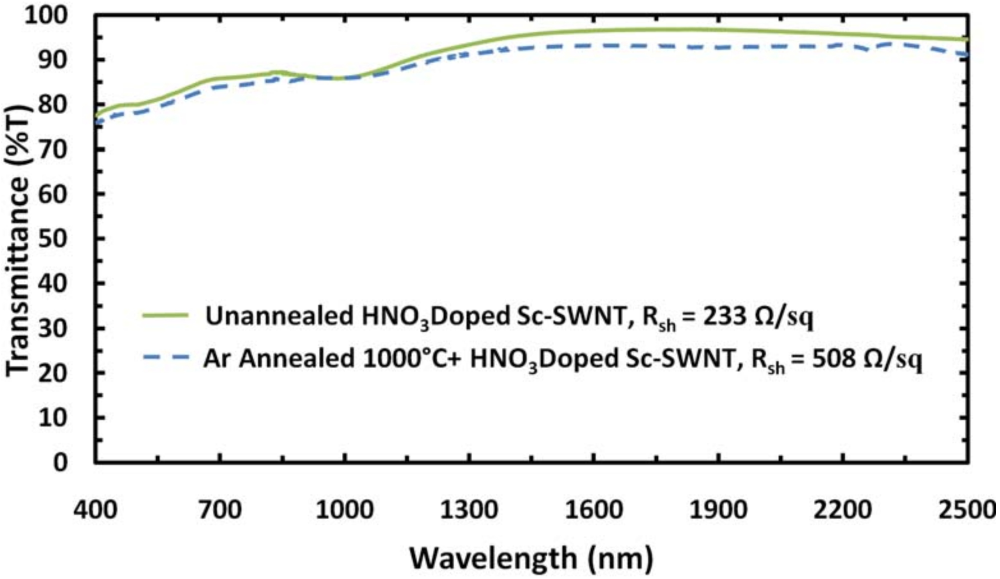

Figure 4.12 UV-Vis-NIR spectra of unannealed HNO_3 doped Sc-SWNT and Ar annealed 1000°C + HNO_3 doped Sc-SWNT electrodes. Sheet resistance is also presented. The electrodes came from the same membrane cut in half.

4.8 Conclusions

This chapter was concerned with the impact of surfactants on the electrode performance of carbon based nanomaterials. A summary of the topics covered in this chapter are presented, along with suggested future work.

Section 4.1 explained the layout of chapter 4 and how chapter 4 investigates the impact of surfactant removal on electrode performance. Section 4.2 investigated the impact of surfactants on nanotube networks via C-AFM analysis. The C-AFM scans of as-made Sc-SWNT and M-SWNT electrodes demonstrated, at the nanoscale, that the electrodes were plagued by electrically inactive or “dead” spots. These dead spots were argued to be detrimental to the performance of OLEDs and OPVs because they would force charge carriers on the surface of the positive electrode to be “redirected” to electrically active spots and thereby increasing the recombination probabilities of excited particles. As a result this was argued to have a potential negative impact on the power conversion efficiency and the lumens per watt efficacy for OPVs and OLEDs, respectively. Nitric acid treatment on the SWNT electrodes was shown to dramatically increase the maximum electrical current within the nanotube network from 1.0nA to 100.0nA. Section 4.3 demonstrated the removal of the surfactant SDS through HNO_3 treatment via XPS scans; and, the removal of surfactant SC through high temperature annealing by comparing the R_{sh} of as-made and annealed graphene puresheets electrodes that were only dispersed with sodium cholate (SC). It was determined that annealing in argon environments was the more effective method to remove surfactants and as such section 4.4 motivated the annealing studies that were conducted in sections 4.5-4.7.

Section 4.5 studied the optoelectronics properties of M-SWNTs as a function of temperature by annealing electrodes in an Ar environment for 1 hour. The study demonstrated improvements in R_{sh} with increasing annealing temperatures up to 600°C. These improvements were suggested to be caused by the removal of surfactants SDS and SC. This suggestion was consistent with the results obtained in section 4.3 through XPS measurements and comparisons of R_{sh} for annealed GPS electrodes. Finally, it was noticed that annealing at a 1000°C caused a sudden increase in R_{sh}. The cause for the increase in R_{sh} was hypothesized to be attributed to the removal of surface functional groups. However, the S_{11} and S_{22} absorption peaks (attributed to <5% Sc-SWNT concentrations) present in the M-SWNTs. Therefore, the UV-Vis-NIR spectra for M-SWNTs were not sensitive enough to detect heavy dedoping.

In section 4.6, the effect of annealing on mixed SWNTs was investigated. The mixed SWNTs demonstrated a larger increase in R_{sh} due to heavy dedoping at 1000°C than the M-SWNTs did. Furthermore, the mixed SWNTs UV-Vis-NIR spectra showed a very slight increase in intensity in the S_{22} absorption peak for 1000°C Ar annealed electrode vs. the 600°C Ar annealed electrode. These observations for M-SWNT and mixed SWNTs both supported the hypothesis that the increase in R_{sh} of the 1000°C Ar annealed samples over that of the 600°C Ar annealed samples was due to heavy dedoping of the functionalized SWNT electrodes.

In section 4.7, the effect of annealing on Sc-SWNTs was investigated. The hypothesis of heavy dedoping by annealing at 1000°C in Ar was heavily supported, through an observed shift or intensification of the S_{22} absorption peak in the 1000°C Ar annealed Sc-SWNT electrode over the 600°C Ar annealed Sc-SWNT electrode. This hypothesis was further supported through the observation that the annealed samples after a 10 day exposure to air experienced a drop in R_{sh} to 36.3% and 29.6% of their original value for the Ar anneal 600°C and Ar anneal 1000°C Sc-SWNT electrodes, respectively. This suggests that the negative annealing effects can be remedied through exposure to air through unintentional doping via oxygen dopants adsorbed onto the surface of the nanotubes. The possibility of refunctionalizing the carbon nanotubes with carboxylic acid groups was not investigated and is left as future work (see Chapter 6). Lastly, it was concluded that the Sc-SWNT electrodes benefit more by being doped with HNO_3 after preparation rather than being annealed in Ar at 1000°C for 1 hr to fully remove surfactants followed by HNO_3 doping.

From this study it is concluded that only the M-SWNT electrodes are positively impacted via surfactant removal through high temperature annealing in Ar for 1 hour. The optimal annealing temperature for M-SWNTs was found to be 600°C. It is suggested to obtain optimal performance for M-SWNT electrodes, that the electrodes should be annealed at 600°C and then doped with HNO_3 and subsequently with $SOCl_2$. This study is left for future work. Furthermore, it is suggested that Sc-SWNT electrodes do not benefit from annealing at high temperatures in Ar and should be doped with HNO_3 and $SOCl_2$ after fabrication.

CHAPTER 5 : GRAPHENE CARBON NANOTUBE COMPOSITE ELECTRODES

5.1 Motivation for Graphene Carbon Nanotube Composites

Graphene is a promising candidate as a transparent electrode due to its high mobility of charge carriers that theoretically allow a highly p-doped pristine sheet of graphene to have a conductivity ratio of 330 [2], which corresponds to a transmittance of ~90% at 550nm with a R_{sh} of 10 Ω/sq. This high theoretical conductivity ratio makes graphene a suitable material for any practical transparent electrode application. However, in practice it is difficult to synthesize a pristine sheet of graphene and the effects of doping on graphene is not yet completely understood and is currently a topic of intense research. Currently as-synthesized graphene sheets are plagued by numerous defect sites that act as potential barriers that hinder charge transport and limit graphene conductivity ratios to ~11[2]; which is far short of the minimum industry standard.

Current solution processing techniques that involve graphene oxide (GO), ultracentrifuged graphene, and exfoliated graphene are currently incapable of producing large area graphene sheets (1 cm^2 or larger)[34, 35, 101]. This poses a problem for solution processed graphene, because the small area sheets need to make contact with one another for there to be conduction pathways for charge carriers to travel across the electrode. The graphene sheets that do not come into contact with other graphene sheets are often referred to as "islands", because they are isolated at the nanoscale from the other sheets of graphene. The gaps between graphene islands act as potential barriers that hinder charge transport and thereby negatively impact R_{sh}. To minimize the occurrence of graphene islands the concentration of solution processed graphene can be increased. However, as was discussed in chapter 2 this requires compromising the transmittance and therefore does not solve the problem. A proposed solution to overcome these problems with graphene is to prepare graphene SWNT composites. To augment the optoelectronic properties of carbon based nanomaterial transparent electrodes.

To understand how a composite can resolve the aforementioned problems, the conductive nature of SWNTs and graphene is discussed. A perfectly pristine sheet of graphene that is free of defects can be thought of as having an infinite number of conduction pathways for charges to travel through within the boundaries of the sheet as it is considered to be a 2D material. SWNTs are considered to be 1D "conducting sticks" that has only one conduction pathway for charges to travel through across individual nanotubes. With this mind it can be easily pictured as SWNTs acting as "bridges" over graphene islands and defect sites and thereby minimizing the effects of the potential barriers formed by the graphene islands. This concept is illustrated in Figure 5.1 where it was envisioned by Tung et al. of a carbon nanotube(CNT) acting as bridge for charge carriers to travel across two isolated graphene sheets. Tung et al. demonstrated a reduced graphene oxide (RGO) CNT composite with R_{sh} of 240Ω/sq at 86%T after chemical doping with $SOCl_2$[25]. This was a significant improvement over plain reduced graphene oxide electrodes that have reported optoelectronic properties of 10^4-10^5Ω/sq at 80%T[25].

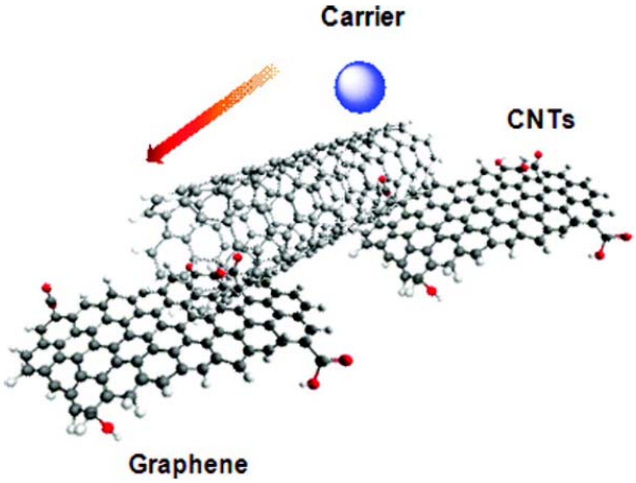

Figure 5.1 Graphene/CNT composite scheme, illustrating how a charge carrier can conduct through a CNT bridge. Taken from reference [25].

Graphene SWNT composites can also be equivantly thought of as using graphene sheets as “nano-patches” to “patch” nanotube networks (NTNs) to add conduction pathways in CNT electrodes, as shown in Figure 5.2[106]. This concept can be understood by recalling that NTNs are web-like with many voids between nanotube bundles, this gives SWNT electrodes their high transparency. Furthermore, when a sheet of graphene is placed on top of a NTN, conduction pathways for charge carriers to conduct across are added with a minimal impact on transmittance[106], typically a ~2% decrease. Moreover, recalling the UV-Vis-NIR spectra of the graphene puresheets electrodes in Figure 3.16, graphene does not have any absorption peaks, due to its lack of a bandgap, to have a significant impact on the transparency in the ultraviolet to near infrared regime.

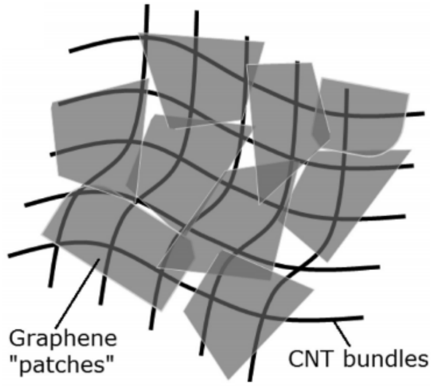

Figure 5.2 The concept of graphene “Nanopatches” on CNT networks is illustrated. Taken from reference [106].

Li et al. demonstrated a R_{sh} of 735Ω/sq at 90%T [106] by combining chemical vapor deposition (CVD) grown CNTs on nickel foils with graphene CVD grown on copper. The CNTs were placed directly on top of the graphene coated copper film and ethanol, poured on top of CNTS, was used to create strong adhesion between the graphene and CNTs. The optoelectronics properties of the individual graphene CVD synthesized by Li et al. were not presented in the article, but sheet resistances of CVD grown CNTs are on the order of 10^4Ω/sq at 80%T[42]. This also represents a significant improvement in optoelectronic properties by employing graphene carbon nanotube composite electrodes.

Xin et al. demonstrated a graphene SWNT composite with R_{sh} 181Ω/sq at 82.2 %T[107]. This was achieved through exfoliating graphene sheets with microwave irradiation at 750W (via graphite intercalation compounds) for 10s, combined it in solution with SWNTs purchased from Aldrich and finally doped the composite electrode with HNO_3 and $SOCl_2$. The graphene SWNT composite developed by Xin et al. showed a significant improvement in optoelectronic properties over exfoliated graphite, treated with HNO_3 to remove the NMP it was dispersed, with a R_{sh} of 3.56kΩ/sq with ~80%T at 550nm by J. H. Lee et al.[108]. Therefore, it is reasonable to hypothesis that graphene and CNT electrodes overall experience enhanced optoelectronic properties through the implementation of composites.

The potential of graphene SWNT composites as transparent conducting electrodes (TCEs), when compared to research on individual graphene and SWNT electrodes, is a fairly new research topic that is still in its infancy. The main benefit obtained when creating a composite is the small sacrifice in transparency for an exchange of a relatively large increase in conductivity, as demonstrated above [25, 106, 107]. This is supported by the fact that graphene does not have any absorption peaks in the UV to NIR regime and that it only decreases transmittance by ~2% transmittance per layer of graphene (see section 5.2).

In the remainder of this chapter reduced graphene oxide SWNT and graphene CVD SWNT composites are discussed. High temperature treatments are employed to reduce graphene oxide as this was determined to be the most effective reduction method in literature[109]. Afterwards, graphene CVD SWNT composites are presented.

5.2 Graphene Oxide Experimental Procedures

Graphene oxide was chosen as the first source of graphene to produce graphene SWNT composites due it being a readily available material that could be easily dispersed in aqueous solutions. The ability to disperse GO in aqueous solutions was compatible with the vacuum filtration technique that was being used throughout the course of this work. Furthermore, the ability of GO to be dispersed in aqueous solutions allows it to be manufactured at large scales with the ultrasonic spray coating technique. However, the outstanding problem with GO is that it is electrically insulating and needs to be reduced. In this section, high-temperature reduction of GO dispersed in water was investigated.

5.2.1 Dispersion of Graphene Oxide in Deionized Water

Graphene oxide aqueous solutions were prepared using PR-1-64 GO powder provided by the Dr. Robert Haddon research group at the University of California Riverside. First, 1mg of PR-1-64 GO powder was measured and placed inside a 4 dram glass vial. Next, 10ml of filtered DI water was added to the glass vial. The aqueous solution was then bath sonicated for 20 minutes with a VWR 75 bath sonicator operated at power level 1.Afterwards, the top 8ml of the solution were remove with a pipette and place into a beaker (care was taken to ensure none of the undissolved GO was picked up). Then, 30ml of DI water were filtered and poured into another beaker and 1ml of 0.5%w/v SDS was added to the same beaker. Next, a MCE membrane filter was rinsed with 60ml of DI water and placed on top of the center of the glass frit in vacuum filtration setup, recall Figure 3.5. Thereafter, the 0.5%w/v SDS diluted in 30mL of DI water was vacuum filtered to prepare the membrane. Afterwards the 8ml of GO solution was vacuum filtered and the film was dried on top of a hot plate at ~70°C typically ~10 minutes.

Transferring the GO films onto transparent substrates via dissolution of the MCE membrane in acetone (outlined in section 3.3.1) was attempted several times. All attempts had little success as all the films had poor adhesion to transparent substrates and the electrode lifted off after the second immersion in the acetone bath. Furthermore, the GO electrodes were far too brittle as the films developed cracks when even the slightest pressure was applied to promote adhesion onto the transparent substrate. To resolve this problem, SWNT solutions were added to the graphene oxide aqueous solution prior to the 20 minute bath sonication at power level 1. The composite films exhibited better adhesion to glass/quartz slides and were more robust than the GO electrode samples.

The composite films were successfully transferred onto transparent substrates, where an example of a GO mixed SWNTs composite solution and electrode transferred on glass are presented in Figure 5.3a and b, respectively. Though difficult to see in Figure 5.3 there were residual GO particles that did not completely dissolve in the DI water. It is important to note that the composite films were not easily transferred and often lifted off during acetone immersions. For this reason several films produced with the same processing conditions were prepared prior to attempting to transfer the composite electrodes onto transparent substrates. This was done to help minimize error associated with comparing films not coming from the same membrane.

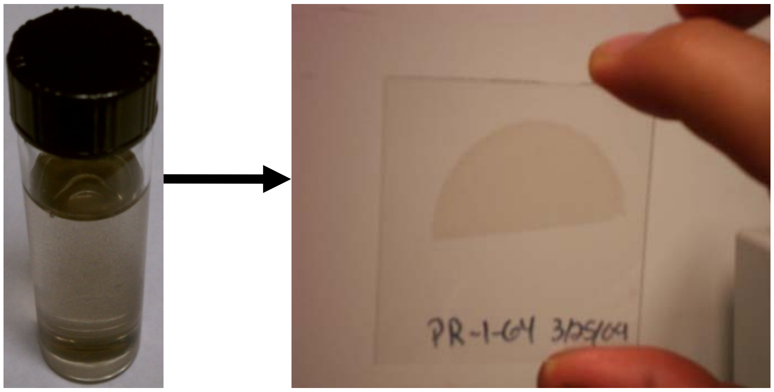

Figure 5.3 (a) GO dispersed in DI water solution. (b) Picture of SWNT puretubes GO composite film transferred onto glass.

It should be noted that instead of the P3-SWNTs dispersed in SDS that were utilized in chapter4, SWNT puretubes dispersed with SDS in aqueous solutions were purchased from Nanointegris. In this chapter the SWNT puretubes will be simply referred to as “mixed SWNTs”. An M-SWNT solution was also purchased from Nanointegris and is the same solution as was used in chapter 4. Sc-SWNTs were not used in this chapter due to the negative impacts on the optoelectronic properties of Sc-SWNTs electrodes experienced by annealing at high temperatures, as discussed in chapter 4.

5.2.2 Thermal Reduction of Graphene Oxide in an Argon Environment

In literature, it is common for researchers to attempt to reduce graphene oxide (GO) by flowing combinations of Ar and H_2 gas during the annealing process. However, it was demonstrated in literature that annealing in ultra high vacuum at a 1100°C was the most effective reduction method over both annealing in Ar and H_2, and hydrazine reduction[109]. Furthermore, in literature density functional theory calculations have shown that hydrogenation of graphene induces a band gap[110], a prime example of this is fully hydrogenated graphene, a wide bandgap semiconductor known as graphane[111]. Therefore, high temperature annealing experiments in an inert environment was the chosen path for reducing GO.

Due to equipment and lab limitations it was not feasible to perform ultrahigh vacuum annealing experiments to reduce graphene oxide, as suggested by Mattevi et al. [109]. An alternative was to anneal in an inert environment of argon, as it was hypothesized that it would yield similar results to ultrahigh vacuum annealing. The details of the annealing procedure are outlined below.

Thermal reduction of graphene oxide experiments were carried out in a First Nano Easy Tube Furnace as presented in Figure 5.4. The samples were loaded into the furnace on top of a loading tray, afterwards the load tray was remote-control closed with the Easy Tube program that was interfaced with the furnace. Before annealing the tube furnace was purged and afterwards 500 standard cubic centimeters per minute (SCCM) of Ar were flowed into the tube furnace. The tube furnace was then heated from room temperature to 1000°C in a period of 15 minutes. Afterwards the temperature of the furnace was held constant at 1000°C for 45 minutes and then the sample was allowed to cool slowly to room temperature over a period of ~3 hours. Finally, the sample was carefully removed from the furnace for further processing and characterization.

Figure 5.4 First Nano Easy Furnace used to anneal graphene oxide CNT composite samples.

It should also be noted that the pressure of the tube furnace was not monitored; this affords the possibility of unknown air leakages to have been present during the annealing runs and thereby adding an "unintentional variable" to the runs done. This led to peculiar results after each annealing run that was not consistent with observations reported in literature or results presented in chapter 4. The effects of this hypothesized unintentional variable are discussed thoroughly in this chapter.

5.2.3 Experimental Overview

The effects of annealing graphene oxide CNT composites in an Ar environment at 1000°C on the optoelectronic properties and the healing of defects were investigated in section 5.2. Experiments were performed for as-made and Ar anneal 1000°C graphene oxide (GO) mixed SWNT composite electrodes; and, as-made and Ar anneal 1000°C M-SWNT composite electrodes. The samples for the GO mixed SWNT and GO M-SWNT composite electrodes did not come from the same membrane due to the poor adhesion of the composite electrodes making it difficult to transfer onto transparent electrodes. However, the composite electrodes were fabricated under the same processing conditions.

To determine if defects were healed during the annealing process Raman spectroscopy measurements were taken before and after annealing. At each stage of the experiments the I_G/I_D values were calculated for three distinct measurement points and then the average was taken. The final value that is presented in this thesis is the average value of the three measurement points.

To distinguish between the annealing effects on SWNTs and graphene oxide, SWNT electrodes were prepared in parallel by Dr. Anuradha Bulusu[86] and were processed under the same conditions and annealed in the same conditions as was done for the composite electrodes. Both sets of data will be presented in this chapter.

In conclusion, the objective of the work done on graphene oxide SWNT composites was to determine the effects of annealing in an Ar environment at 1000°C on the optoelectronic properties and the healing of defects. Furthermore, the individual effects of annealing on graphene oxide and SWNT electrodes were distinguished through comparison with the data collected by Dr. Anuradha Bulusu on SWNT electrodes fabricated with the same processing conditions.

5.3 Graphene Oxide Carbon Nanotube Composite Electrodes

5.3.1 Graphene Oxide Mixed Carbon Nanotube Composite Electrodes

The first experiment that was conducted was for a mixed SWNT graphene oxide (GO) composite. Due to the difficulty in transferring the mixed SWNT GO composites, it is reiterated that the films did not come from the same membrane; but, were prepared under the same processing conditions. The UV-Vis-NIR spectra for as-made and Ar anneal 1000°C GO mixed SWNT composite electrodes are presented in Figure 5.5. Interestingly there is a complete upward shift in the entire UV to NIR regime in the UV-Vis-NIR spectra and the sheet resistance had also decreased. Furthermore, the S_{11} absorption peak had intensified as expected from the discussion in section 3.5. However, this simultaneous increase in the transmittance and decrease in sheet resistance, from the author's knowledge, has not been presented in the literature. Furthermore, drastic increases in the transmittance of graphene oxide via reduction to graphene have not been reported in the literature. The increase in the transmittance from this Ar annealing process is ~14%, which is well above the resolution of the Cary 5E UV-Vis-NIR spectrophotometer. This peculiar behavior is investigated in further detail in the remainder of this section.

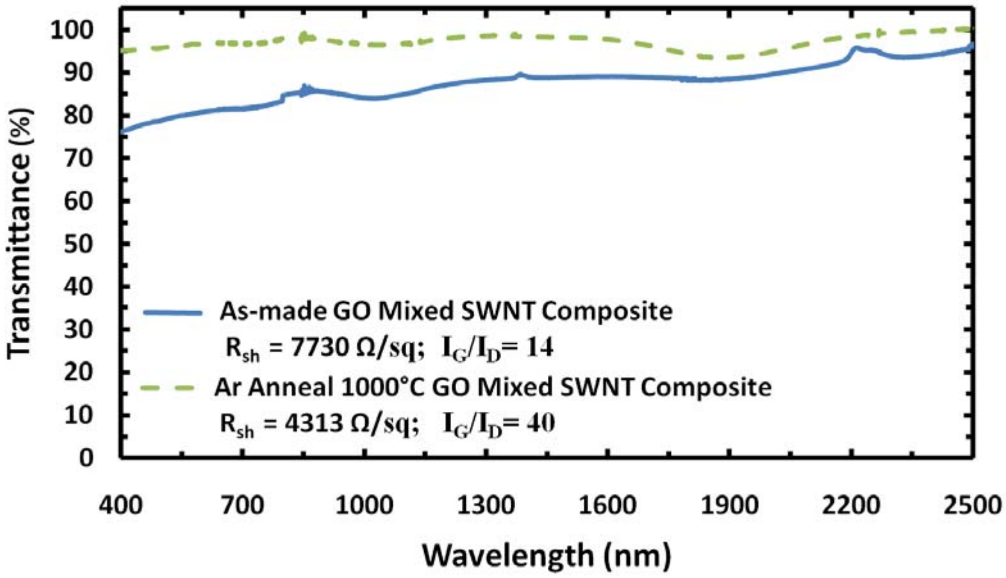

Figure 5.5 UV-Vis-NIR spectra and sheet resistance of as-made and Ar anneal 1000°C graphene oxide mixed SWNT composite electrodes.

Raman scans performed on the GO mixed SWNT composites electrodes, demonstrated an increase in the I_G/I_D ratios from 17 for the as-made composite to 40 in the 1000°C Ar anneal sample. This suggests that defects have been healed. Therefore, the sheet resistance of the post annealed graphene oxide mixed SWNT composite is likely attributed to the reduction of graphene oxide and the healing of defects. At this point it is not certain if the healing of defects is due to the reduction of graphene oxide, if it is due to the nanotubes, or both.

To distinguish between the individual contributions of graphene oxide and the mixed SWNTs, Dr. Anuradha Bulusu conducted a parallel experiment with mixed SWNT electrodes with the same processing conditions. The results of the transmittance and sheet resistance of the as-made and Ar anneal 1000°C mixed SWNT electrodes are presented in Figure 5.6. It is interesting to note that after the mixed SWNTs were annealed in an Ar environment at 1000°C the sheet resistance went up, which is consistent, with the observations made for the 1000°C Ar anneal mixed SWNT sample shown in chapter 4, (see Figure 4.10). As discussed in chapter the increase in sheet resistance is due in part to the removal of surface functional groups. However, the increase in transmittance by ~17% is peculiar and does not agree with the experiments done in chapter 4.

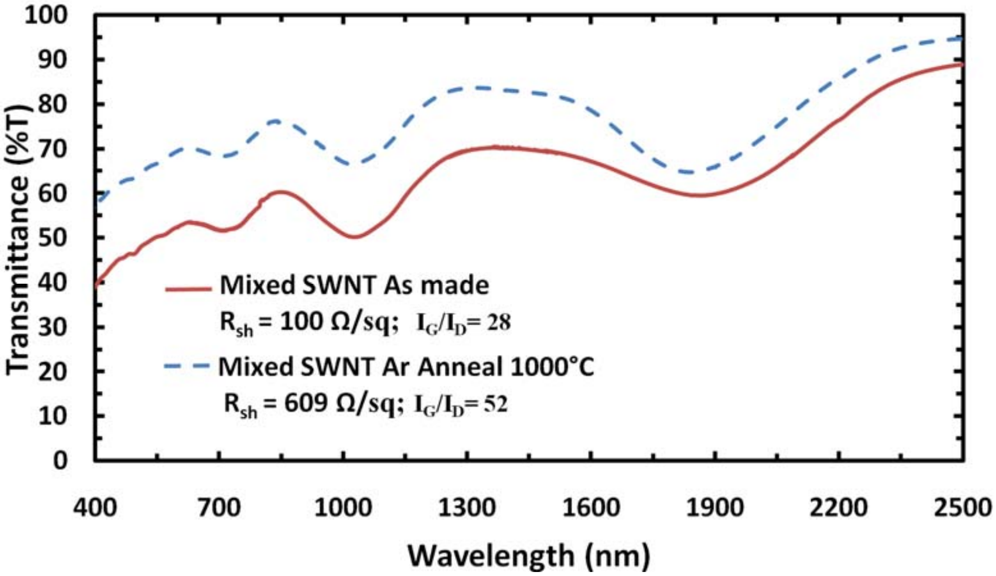

Figure 5.6 UV-Vis-NIR spectra and sheet resistance of as-made and Ar anneal 1000° mixed SWNT electrodes[86].

Raman scans performed on the mixed SWNT electrodes, contrary to the results obtained for mixed SWNTs done in chapter 4, showed an increase in the I_G/I_D ratios from 28 for the as-made mixed SWNT to 52 in the 1000°C Ar anneal mixed SWNT electrode. This suggests that defects have been healed and is consistent with the data collected for the as-made and Ar anneal 1000°C GO mixed SWNT composite electrodes.

For the mixed SWNT electrodes annealed at 1000°C in an Ar environment, it is suggested that the removal of surface functional groups is the dominating factor that is contributing to the increase in sheet resistance. Furthermore, the result of the mixed SWNT electrode also lightening strongly suggests that the increase in transmittance is not due to the reduction of graphene oxide as was hypothesized. Moreover, the mixed SWNTs experienced a comparable increase in transmittance as the GO mixed SWNT composite electrodes. This suggests that the nanotubes are more likely the source of the increase in transmittance rather than the graphene oxide.

The next topic of interest is to determine if the observed increase in transmittance is restricted to mixed SWNTs or if a similar increase in transmittance can be obtained for M-SWNT electrode.

5.3.2 Graphene Oxide Metallic Carbon Nanotube Composite Electrodes

The optoelectronic properties of the as-made and Ar anneal 1000°C graphene oxide M-SWNT composite electrode were measured and presented in Figure 5.7. Again, it is interesting to note that the UV-Vis-NIR spectra of Ar anneal 1000°C experienced an upward shift in transmittance. Furthermore, the M-SWNT Ar anneal 1000°C electrode’s sheet resistance also decreased. The M-SWNT electrode’s sheet resistance is expected to decrease because of the removal of surfactants as was shown in chapter 4.

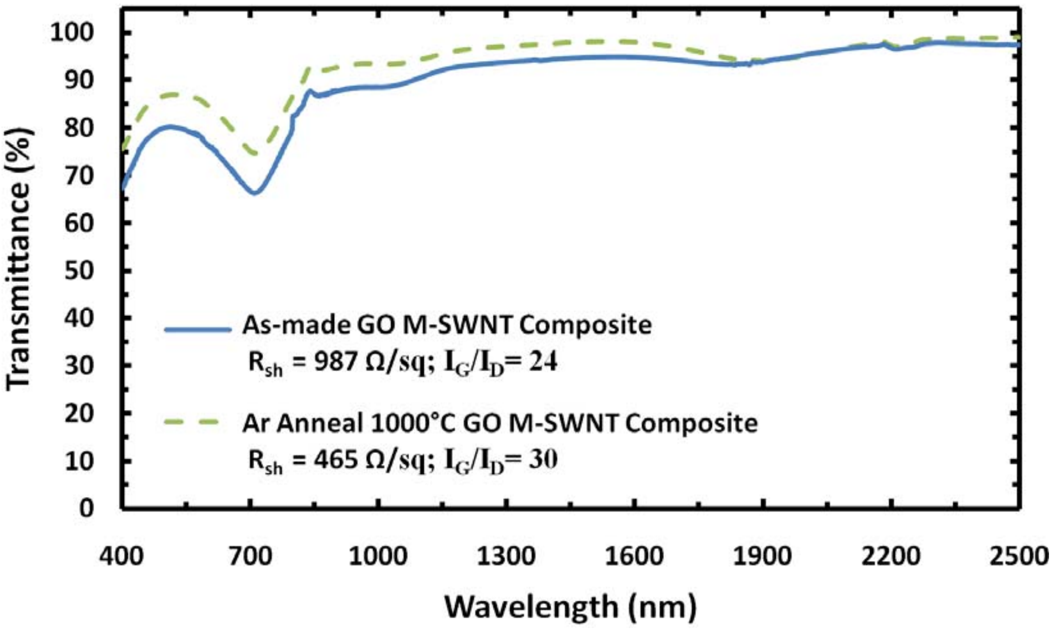

Figure 5.7 UV-Vis-NIR spectra and sheet resistance of as-made and Ar anneal 1000°graphene oxide M-SWNT composite electrodes.

Raman measurements taken on the GO M-SWNT composite electrodes, consistent with the results obtained for the GO mixed SWNTs composited electrodes, demonstrated an increase in the I_G/I_D ratios from 24 for the as-made mixed SWNT to 30 in the 1000°C Ar anneal mixed SWNT electrode. This suggests that defects have been healed and is consistent with the data collected for the as-made and Ar anneal 1000°C GO mixed SWNT composite electrodes.

To distinguish between the individual contributions of graphene oxide and the M-SWNTs, Dr. Anuradha Bulusu[86] conducted a parallel experiment with M-SWNT electrodes with the same processing conditions. The results of the transmittance and sheet resistance of the as-made and Ar anneal 1000°C M-SWNT electrodes are presented in Figure 5.8. It is interesting to note that after the M-SWNTs were annealed in an Ar environment at 1000°C, the sheet resistance improved, which is consistent, with the observations made for the 1000°C Ar anneal M-SWNT sample shown in chapter 4, (see Figure 4.9). As discussed in chapter 4 the improvement in sheet resistance for the M-

SWNT electrodes is due in part to the removal of surfactants. However, the increase in transmittance by ~9% is peculiar and does not agree with the experiments done in chapter 4.

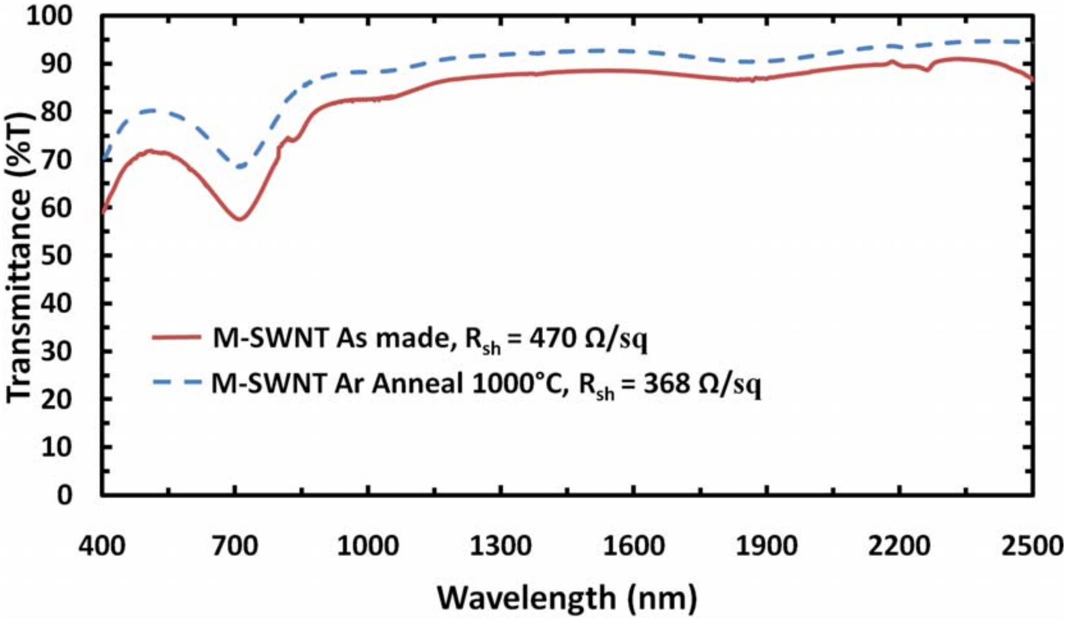

Figure 5.8 UV-Vis-NIR spectra and sheet resistance of as-made and Ar anneal 1000° mixed SWNT electrodes[86].

5.3.3 Hypothesized Effects of Oxygen Annealing

The graphene oxide SWNT composite electrodes along with the SWNT electrodes all mysteriously experienced an increase in transmittance after being annealed in Ar environment at 1000°C in the First Nano Easy Tube Furnace. An important observation that was made with regards to the experimental procedure is that the pressures inside the furnace during the annealing processes were not monitored, whatsoever. Furthermore, the First Nano Furnace was heavily used for over 5 years. Therefore, it is reasonable to hypothesis that possibly there were slight air leakages flowing into the tube furnace during annealing process, as a result of natural degradation of the furnace over its lifetime.

Of the various gases that compose air, oxygen (21% by volume in air) has been known to decompose or “eat” away carbon nanotubes[104]. Hata et al. performed a thermogravimteric analysis in air on CVD grown SWNTs, the results for the run are presented in Figure 5.9. Inspection of Figure 5.9 shows that the combustion point for SWNTs starts at about 600°C when exposed to air. Interestingly Hata et al. also demonstrated that by controlling the amount of water vapor flowed into their furnace during the CVD growth, actually assisted growth allowing them to grow a 2.5mm tall “SWNT forest”. Moreover, Tsai et al. demonstrated that “bamboo-like” defects in CVD multi-walled carbon nanotubes were healed when water vapor was introduced during their rapid vacuum arc annealing process. Tsai et al. suggested that oxygen might have played an important role in healing defects[104].

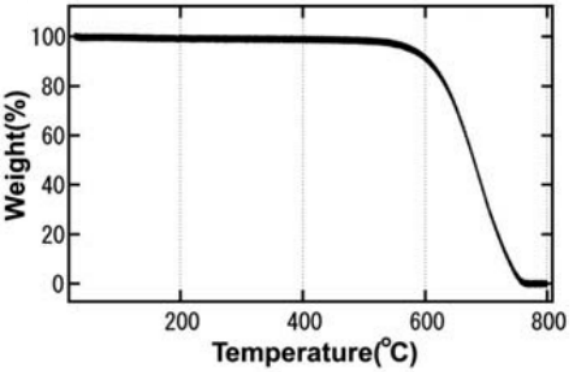

Figure 5.9 Thermogravimetric analysis data for 10mg CVD SWNT in air with a 10°C/min ramp rate. Taken from reference[112].

Due to time and available equipment constraints, an in-depth study on the effects of annealing in a controlled oxygen environment was not carried out. Therefore, this upcoming discussion does not attempt to give strong evidence that in the presence of oxygen was the reason for the observed increases in transmittance in the experimental runs presented in this section. Rather the presence of oxygen in the annealing processes is presented as a hypothesis and is left for future work.

To begin the discussion of the hypothesized effects of annealing, a summary of the experimental data obtained for both the GO mixed SWNT and the GO M-SWNT is presented in Table 5.1. The composite electrodes both experienced improvements in sheet resistance along with an increase in I_G/I_D on top of the improvements in transmittance. The increase in transmittance observed for the composite GO SWNTs is hypothesized to be caused by the slight presence of oxygen inside the tube furnace during the annealing process. The presence of oxygen is suspected to be the key difference as to why the healing of defects was observed in the experimental runs done in this chapter as opposed to the ones done in chapter 4. The decrease in sheet resistance for the GO SWNT composites is suggested to be caused by a combination of the removal of insulating surfactants SDS and SC, the healing of defects, and the reduction of graphene oxide.

Table 5.1 Summary of optoelectronic properties and I_G/I_D for prepared reduced graphene oxide SWNT composites.

Sample	R_{sh} (Ω/sq)	Transmittance (%T)	I_G/I_D
Mixed SWNT **As-made**	7730	83	17
Mixed SWNT **1000°C Ar Anneal**	4313	97	40
M-SWNT **As-Made**	987	79	24
M-SWNT **1000°C Ar Anneal**	465	88	30

As discussed earlier in this section to compliment the studies done on GO SWNT composites, parallel experiments were performed on SWNT electrodes fabricated and characterized with the same processing conditions. A summary of the optoelectronic and I_G/I_D data collected for the mixed SWNT and M-SWNT electrodes is presented in **Table** 5.2

Table 5.2 Summary of optoelectronic properties and I_G/I_D for SWNT electrodes [86].

Sample	R_{sh} (Ω/sq)	Transmittance (%T)	I_G/I_D
Mixed SWNT As Made	100	50	28
Mixed SWNT 1000°C Ar Anneal	609	67	52
M-SWNT As-Made	470	71	-
M-SWNT 1000°C Ar Anneal	368	80	-

The experimental runs for the SWNTs electrodes performed [86], also demonstrated comparable increases in transmittance for both mixed SWNTs and M-SWNTs. Furthermore, the I_G/I_D was also shown to increase for the mixed SWNTs suggesting the healing of defects as was demonstrated for the GO mixed SWNT composite electrodes. Unfortunately, there was no I_G/I_D collected for the M-SWNT electrodes and therefore it is not known if the defects were healed through thermal annealing. The increase in sheet resistance for the 1000°C Ar anneal mixed SWNT electrode is likely attributed to the removal of surface functional groups as was demonstrated in chapter 4. Lastly, the improvement in sheet resistance in the 1000°C Ar anneal M-SWNT electrode is suggested to be attributed to the removal of surfactants and "possibly" the healing of defects.

5.4 CVD Grown Graphene Metallic Carbon Nanotube Composites

In this section, a CVD grown graphene M-SWNT composite electrode was studied briefly in an attempt to obtain the best performing CBN electrode. To determine the relative improvement in the optoelectronic properties obtained by adding two graphene layers a comparison as-made M-SWNT electrode was characterized as well.

Furthermore, a single graphene layer's optoelectronic properties were characterized to give a reference point for the graphene CVD.

5.4.1 Experimental Procedures

Graphene CVD samples grown on copper were provided by Hossein Sojoudi and were prepared using the catalyst etching and subsequent stamping. The M-SWNT electrode was prepared from solution bought from Nanointegris and were prepared using the vacuum filtration method outlined in section 3.3. The M-SWNT electrodes were transferred onto a quartz slide through the film transfer process outlined in section 3.3.1. The M-SWNT electrode was prepared using an old frit and low quality DI water (see section appendix C).

The optoelectronic properties for the graphene CVD samples were characterized and the results are presented in Figure 5.10. As expected the graphene CVD has no absorption peaks and has a transmittance of ~97% at a wavelength of 550nm.

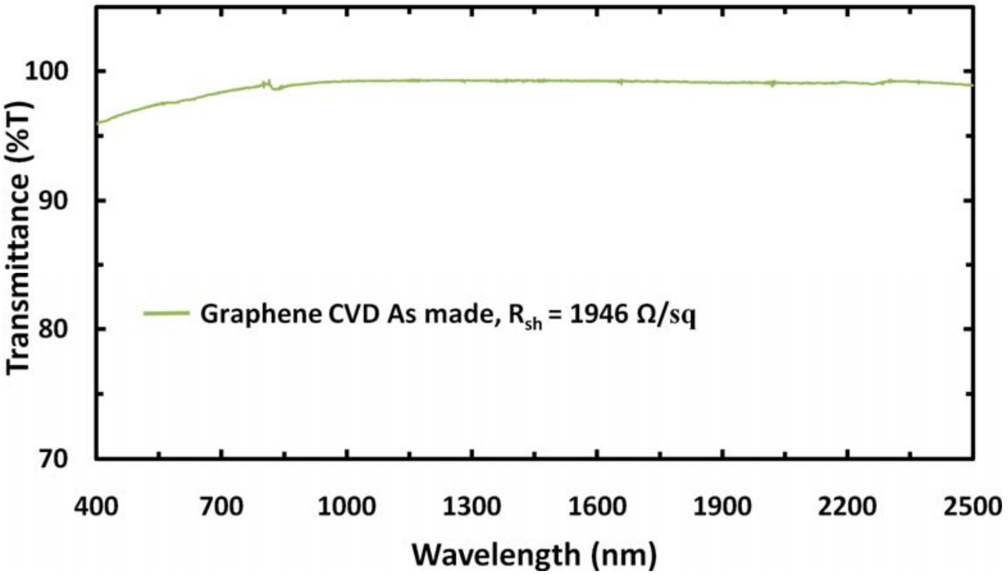

Figure 5.10 UV-Vis-NIR spectra along with sheet resistance of graphene CVD electrode. Graphene electrode provided by Hossein Sojoudi in Dr. Samuel Graham's research group.

5.4.2 Results of Chemical Vapor Deposition Graphene Metallic Carbon Nanotube Composite

In this experiment, a vacuum filtered M-SWNT film was cut in half and one half was transferred onto a clean quartz slide and was labeled film A and the other half of M-SWNT film was used for the graphene M-SWNT composite, film B. This was done to track the improvement in the optoelectronic properties of M-SWNT electrode by adding two layers of graphene. To build the graphene M-SWNT composite or fim B, a layer of graphene CVD was transferred onto a clean quartz slide, then the M-SWNT electrode was transferred on top of the graphene CVD layer, and finally another graphene layer was deposited on top of the M-SWNT electrode. The characterized optoelectronic properties of the "sandwiched" graphene CVD M-SWNT composite and of the M-SWNT electrode are presented in Figure 5.11.

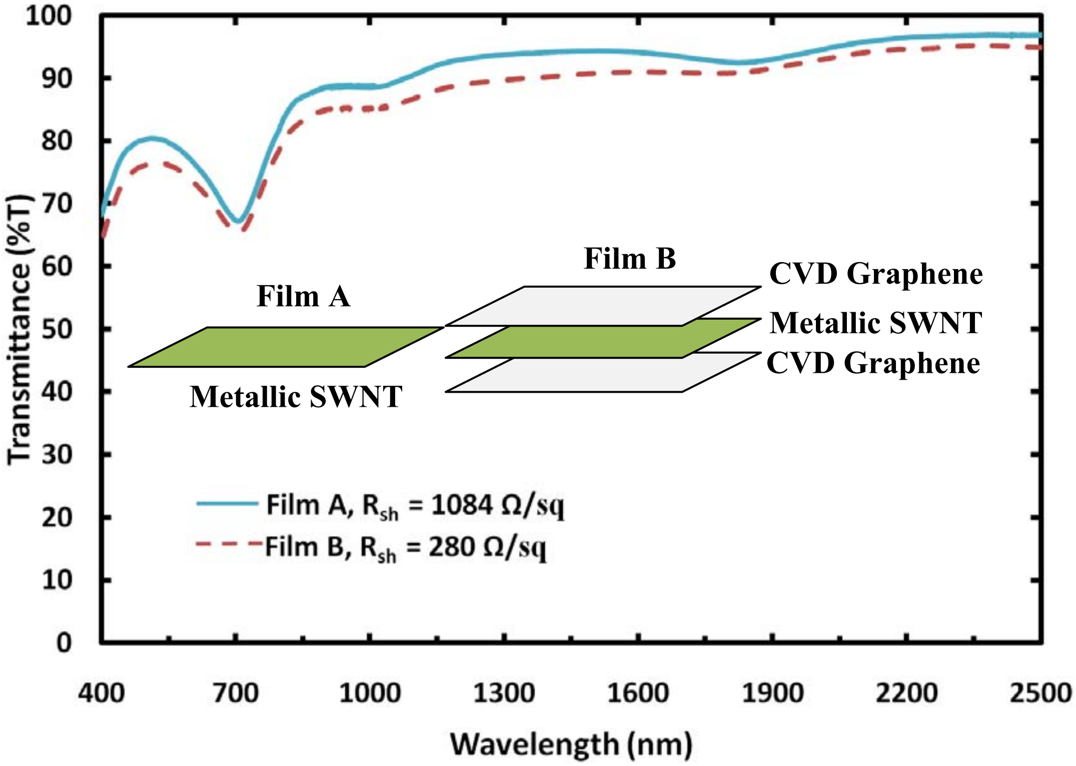

Figure 5.11 Comparison of M-SWNT transparent electrode versus sandwiched graphene CVD composite

5.5 Conclusions

This chapter discussed the use of graphene SWNT composite electrodes as a means to improve the electronic properties of SWNT electrodes with a minimal impact on the transmittance. In this chapter, graphene oxide SWNT and CVD grown graphene SWNT composites electrodes were investigated. A summary of the topics covered in this chapter are presented, along with suggested future work.

Section 5.1 introduced graphene SWNT composites and motivated the need to study these composite materials as potential transparent electrodes for organic electronics. It was explained that the addition of graphene creates a significant increase in conduction pathways for charge carriers to conduct while minimally sacrificing optical transmittance (~2%T). Furthermore, a brief literature review was provided as well.

Section 5.2 discussed the experimental procedures utilized to prepare graphene oxide (GO) electrodes dispersed in DI water. However, the GO films were not easily transferred onto transparent substrates and it was necessary to add SWNTs in the GO solution to transfer the GO onto transparent substrates. The experimental methods utilized to anneal GO SWNT composites electrodes in an Ar environment at 1000°C were outlined.

In section 5.3 the graphene oxide SWNT composite electrodes along with the SWNT electrodes all mysteriously experienced an increase in transmittance after being annealed in Ar environment at 1000°C in the First Nano Easy Tube Furnace. An important observation that was made with regards to the experimental procedure is that the pressures inside the furnace during the annealing processes were not monitored. The increase in transmittance observed for the composite GO SWNTs and SWNT electrodes was hypothesized to be caused by a slight presence of oxygen inside the tube furnace, due to air leakage, during the annealing process. The presence of oxygen was suspected to be the reason as to why the healing of defects was observed in the experimental runs done in this chapter. This is supported by the study of Tsai et al. were it was demonstrated that “bamboo-like” defects in CVD multi-walled carbon nanotubes were healed when water vapor was introduced during their rapid vacuum arc annealing process. Tsai et al. suggested that oxygen might have played an important role in healing defects[104]. The observed decrease in sheet resistance for the prepared GO SWNT composites, despite increases in transmittance suggesting possible removal of material, was suggested to be caused by a combination of the removal of insulating surfactants SDS and SC, the healing of defects, and the reduction of graphene oxide. For the 1000°C Ar anneal mixed SWNT electrode the observed increase in sheet resistance for the was suggested to be attributed to the removal of surface functional groups as was demonstrated in chapter 4. For the 1000°C Ar anneal M-SWNT electrode improvement in sheet resistance was suggested to be attributed to the removal of surfactants and “possibly” the healing of defects.

Section 5.4 characterized the optoelectronics of an M-SWNT electrode labeled film A and that of “sandwiched” graphene CVD MSWNT composite electrode labeled film B, where a layer of graphene was deposited above and below the MSWNT electrode. An improvement in the optoelectronic properties for film A was observed from a sheet resistance of 1084Ω/sq with 80%T at a wavelength of 550nm to a sheet resistance 280Ω/sq with 76%T at a wavelength of 550nm.

For future work, it is suggested to perform an annealing study of SWNT electrodes in a controlled oxygen environment, where Ar is flowed into the furnace to dilute the oxygen to ensure the films are not completely eaten away. Raman measurements to investigate the healing of defects are suggested as well. Lastly, a more detailed study of graphene CVD M-SWNT composite electrodes is also left for future work.

CHAPTER 6 : CONCLUSIONS AND FUTURE WORK

6.1 Summary of Research and Conclusions

The first goal of this thesis was to add to the fundamental understanding of the physics involved with the removal of surfactants for solution processed SWNT electrodes. Surfactant removal techniques that were studied included annealing in argon environments with temperatures up to 1000°C and through nitric acid treatments. The second goal of this thesis was to investigate the potential of graphene SWNT composite electrodes as high performing transparent electrodes. The insight gained in this work is suggested to be used for future studies to help optimize the optoelectronics properties of carbon based nanomaterial transparent conductive electrodes.

Important findings in this work are as follow:

- Chapter 4 expanded the understanding on the impact of surfactant removal on electrode performance. C-AFM measurements for as-made Sc-SWNT and M-SWNT electrodes demonstrated, at the nanoscale, that the electrodes were plagued by electrically inactive or “dead” spots. These dead spots were argued to be detrimental to the performance of OLEDs and OPVs because they would force charge carriers on the surface of the positive electrode to be “redirected” to electrically active spots; and thereby increase the recombination probabilities of excited particles. Furthermore, nitric acid doped and dedoped M-SWNT electrodes demonstrated a dramatic improvement in the current conductivity maps obtain from C-AFM measurements with a +10mV bias from 1nA for the as made M-SWNT electrode to 100nA for the doped and dedoped M-SWNT electrodes. A similar trend was found for Sc-SWNT doped and dedoped electrodes; however the Sc-SWNT electrodes were not as electrically active as the M-SWNT electrodes. Suggesting that Sc-SWNT electrodes needed to be further doped with thionyl chloride to outperform M-SWNT electrodes. Moreover, it was found that an optimal annealing temperature for M-SWNT electrodes was 600°C in an argon environment for 1 hour. The Sc-SWNT and mixed SWNTs were found to not benefit from annealing treatments. Finally, it was observed that the Ar anneal 600°C and Ar anneal 1000°C Sc-SWNT electrodes after a 10 day exposure to air, experienced a drop in R_{sh} to 36.3% and 29.6% of its original value, respectively. This suggests that the negative effects of annealing are reversible. The decrease in sheet resistance is suggested to be likely due to oxygen adsorption from exposure to air.

- In chapter 5, graphene oxide SWNT composite electrodes along with the SWNT electrodes all mysteriously experienced an increase in transmittance after being annealed in Ar environment at 1000°C in the First Nano Easy Tube Furnace. An important observation that was made with regards to the experimental procedure is that the pressures inside the furnace during the annealing processes were not monitored. The increase in transmittance observed for the composite GO SWNTs and SWNT electrodes was hypothesized to be caused by a slight presence of oxygen inside the tube furnace, due to air leakage, during the annealing process. The presence of oxygen is suspected to be the reason as to why the healing of defects was observed in the experimental runs done in this chapter. The observed decrease in sheet resistance for the prepared GO SWNT composites was suggested to be caused by a combination of the removal of insulating surfactants SDS and SC, the healing of defects, and the reduction of graphene oxide. For the 1000°C Ar anneal mixed SWNT electrode the observed increase in sheet resistance was suggested to be attributed to the removal of surface functional groups as was demonstrated in chapter 4. For the 1000°C Ar anneal M-SWNT electrode improvement in sheet resistance was suggested to be attributed to the removal of surfactants and “possibly” the healing of defects. Finally, the addition of chemical vapor deposition grown graphene layers above and below an M-

SWNT was found to significantly improve the electronic properties of M-SWNT electrode with only minimal impact on optical transmittance.

6.2 Future Work

For future work on the impact of surfactant removal, it is suggested to characterize Ar annealed SWNT electrodes with conductive tip atomic force microscopy measurements to investigate the nanoscale currents maps of the annealed electrodes. It is suspected that a noticeable increase in conductivity should be observed, but it is not clear how much. It would be interesting to observe how the Ar annealed SWNT electrodes compare to the nitric acid doped SWNT electrodes. This would give additional knowledge on the pros and cons of using thermal treatments. Also, a thermogravimetric analysis on mixed SWNT, semiconducting SWNT, and metallic SWNT electrodes is suggested for future work to better understand how trace surfactants are removed as a function of temperature.

For future work on annealing studies, it is suggested to anneal SWNT electrodes in a controlled oxygen environment, where Ar is flowed into the furnace to dilute the oxygen to ensure that the films are not completely eaten away. Raman measurements to investigate the healing of defects are suggested as well.

For future work on refunctionalization of carbon nanotubes after being annealed in an Ar environment, it is suggested to flow a hydrocarbon gas such as methane or acetylene in argon environment during the secondary anneal process. The presence of hydrocarbons may have the potential to refunctionalize the carbon nanotubes and possibly heal defects. Another possible technique to refunctionalize the nanotubes is through acid reflux treatment with sulfuric acid.

Finally, for future work it is suggested to study an optimally annealed metallic SWNT graphene composite electrode that is subsequently treated with nitric acid and thionyl chloride. To do this it is suggested to first deposit a layer of chemical vapor deposition grown graphene on a transparent substrate. Next, deposit a metallic SWNT electrode on top of the graphene layer and anneal at the optimized temperature of 600°C. Thereafter, the electrode should be doped with nitric acid and subsequently with thionyl chloride. Finally, another layer of chemical vapor deposition graphene is suggested to be deposited on top of the electrode.

APPENDIX A: STRUCTURE AND ELECTRONIC PROPERTIES OF CARBON BASED NANOMATERIALS

A.1 Structure and Electronic Properties of Graphene

In Figure A.1, the unit cell of graphene is constructed by enclosing two carbon atoms, A and B. The lattice vectors $\vec{a}_1$ and $\vec{a}_2$ can be determined through inspection as shown in equation A.1, where the lattice constant is defined in equation A.2. The chiral vector $\vec{C}_h$ can be used to uniquely identify any position on the graphene sheet. $\vec{C}_h$ is defined in equation A.3, where *m* and *n* are integers.

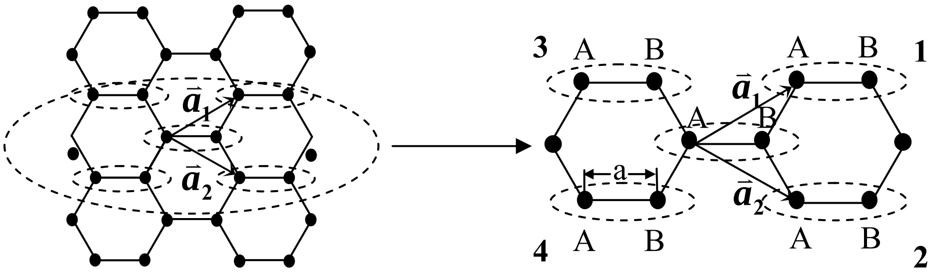

Figure A.1 Graphene honeycomb lattice structure with unit cell and lattice vectors shown. The nearest neighbor unit cells are numbered from 1 to 4. Adapted from reference[113].

$$\vec{a}_1 = \frac{3a}{2}\hat{x} + \frac{\sqrt{3}a}{2}\hat{y};\ \vec{a}_2 = \frac{3a}{2}\hat{x} - \frac{\sqrt{3}a}{2}\hat{y} \tag{A.1}$$

$$a = \sqrt{3}a_{C-C} = \sqrt{3}(0.142\text{nm}) = 0.246\text{nm} \tag{A.2}$$

$$\vec{C}_h = m\vec{a}_1 + n\vec{a}_2 \tag{A.3}$$

To determine the density of states of graphene it is first necessary to solve the Schrödinger equation for the 2D energy dispersion relation, $E_{2D}(k_x,k_y)$. The Schrödinger equation is defined in equation A.4, where *H* is the Hamiltonian operator, and *Φ* is the wave function. To solve for the energy dispersion relation of graphene, the Schrödinger equation can be written in matrix form as shown in equation A.5.

$$E\Phi = H\Phi;\ H = -\frac{\hbar}{2m}\nabla^2 + U \tag{A.4}$$

$$E\{\phi\} = [H]\{\phi\} \tag{A.5}$$

However, equation A.5 is impractical as the size of the Hamiltonian matrix is NbxNb, where N is the number of unit cells in a structure and b is the number of basis functions per unit cell. Typically N is a huge number, thereby complicating matters by yielding a very large Hamiltonian matrix. Fortunately, for periodic structures equation A.5 can be rewritten as shown in equation in A.6, so that all the unit cells in a structure can be summed N times and thus shrinking the Hamiltonian to a bxb matrix.

$$E\{\phi_n\} = \sum_m [H_{nm}]\{\phi_m\} \tag{A.6}$$

Next, there are two carbon atoms per unit cell in graphene and there are four valence orbitals (2s, $2p_x$, $2p_y$, $2p_z$), where the core level 1s is stable and can be ignored, making b equal to eight. Therefore, there are 8 basis functions in the unit cell, resulting in an 8x8 Hamiltonian matrix, which is still too large to solve without the aid of a computer. Fortunately, it has been found that for a flat sheet of graphene the 2s, $2p_x$, and $2p_y$ orbitals are dissociated from the $2p_z$ orbital in the Hamiltonian matrix [113]. This follows since the energy levels for the 2s, $2p_x$, and $2p_y$ orbitals lie far above or far below the Fermi level and the $2p_z$ orbital lies around the Fermi level [113].

The three valence orbitals of carbon in the 2s, $2p_x$, $2p_y$ orbitals hybridize to form an sp^2 orbital. The sp^2 orbitals form σ-bonds that bind graphene together and as such are only useful to determine the mechanical properties of graphene [113]. The remaining valence orbital $2p_z$ forms π-bonds in graphene, which are largely responsible for charge transport. Thus, when considering electronic properties of graphene it is only necessary to use the $2p_z$ orbital as a basis function to calculate the density of states [113]. Therefore, the original Hamiltonian matrix has again been shrunk from an 8x8 matrix to a 2x2 matrix and therefore simplifying the problem immensely.

Graphene's structure is periodic and therefore Bloch's theorem (equation A.4) in discrete form applies as a solution to the wavefunction in Schrödinger's equation. Substituting equation A.7 into equation A.6 and simplifying yields equation A.8. Now a new Hamiltonian matrix can be defined, which shall be denoted as [$h(k)$] in equation A.9.

$$\{\phi_n\} = \{\phi_0\} e^{i\vec{k}\cdot\vec{r}_n} \tag{A.7}$$

$$E\{\phi_0\} = \sum_m [H_{nm}] e^{i\vec{k}\cdot(\vec{r}_m - \vec{r}_n)} \{\phi_0\} \tag{A.8}$$

$$[h(k)] = \sum_m [H_{nm}] e^{i\vec{k}\cdot(\vec{r}_m - \vec{r}_n)} \tag{A.9}$$

The terms in the new Hamiltonian can be determined through the tight binding method by adding the contributions of the nearest-neighbors with equation A.9 and referring to Figure 2.2. The new Hamiltonian [$h(k)$] is setup as shown in equation A.10. Equation A.10 can then be simplified as shown in equation A.11. By defining a new dummy variable h_0, [$h(k)$] can be rewritten as shown in equation A.12, where h_0^* is the conjugate of h_0 and t is the nearest-neighbor transfer integral with a value of ~2.8eV[114].

$$[h(\vec{k})] = \begin{bmatrix} 0 & t \\ t & 0 \end{bmatrix} + \begin{bmatrix} 0 & 0 \\ t & 0 \end{bmatrix} e^{i\vec{k}\cdot\vec{a}_1} + \begin{bmatrix} 0 & 0 \\ t & 0 \end{bmatrix} e^{i\vec{k}\cdot\vec{a}_2} + \begin{bmatrix} 0 & t \\ 0 & 0 \end{bmatrix} e^{-i\vec{k}\cdot\vec{a}_1} + \begin{bmatrix} 0 & t \\ 0 & 0 \end{bmatrix} e^{-i\vec{k}\cdot\vec{a}_2} \tag{A.10}$$

$$[h(\vec{k})] = \begin{bmatrix} 0 & t\left(1 + e^{-i\vec{k}\cdot\vec{a}_1} + e^{-i\vec{k}\cdot\vec{a}_2}\right) \\ t\left(1 + + e^{i\vec{k}\cdot\vec{a}_1} + e^{i\vec{k}\cdot\vec{a}_2}\right) & 0 \end{bmatrix} \tag{A.11}$$

$$[h(\vec{k})] = \begin{pmatrix} 0 & h_0 \\ h_0^* & 0 \end{pmatrix}; \; h_0 = t\left(1 + e^{-i\vec{k}\cdot\vec{a}_1} + e^{-i\vec{k}\cdot\vec{a}_2}\right) \tag{A.12}$$

Expanding equation A.12 and simplfying h_o can be rewritten as shown in equation A.13. Recallinng euler's formula h_o can be rewritten as shown in equation A.14 below.

$$h_0 = t\left(1 + e^{-i\frac{3}{2}ak_x}\left(e^{i\frac{\sqrt{3}}{2}ak_y} + e^{-i\frac{\sqrt{3}}{2}ak_y}\right)\right) \tag{A.13}$$

$$h_0 = t\left(1 + 2e^{-i\frac{3}{2}ak_x}\cos\left(\frac{\sqrt{3}}{2}ak_y\right)\right) \tag{A.14}$$

Finally solving for the eigenvalues yields the solution for the 2D energy dispersion relation as shown in equation A.15.

$$E_{2D}(k_x,k_y)=\pm t\left\{1+4\cos\left(\frac{\sqrt{3}k_y a}{2}\right)\cos\left(\frac{3k_x a}{2}\right)+4\cos^2\left(\frac{\sqrt{3}k_y a}{2}\right)\right\}^{1/2} \qquad \text{(A.15)}$$

The density of states can then be determined from equation A.16.[115]

$$D(E)=\sum_{\mu}\delta\left(E_\mu(\vec{k})-E\right) \qquad \text{(A.16)}$$

When dealing with a large enough sheet of graphene sheet the summation in equation in 2.10 can be transformed into a integral as shown in equation A.17. [116]

$$\mathrm{DOS}(E)=\frac{2}{N}\sum_{\mu=1}^{N}\int\frac{1}{\left|\frac{dE_\mu(k)}{dk}\right|}\delta\left(E_\mu(\vec{k})-E\right)dE \qquad \text{(A.17)}$$

The energy band theory for graphene that considers the next nearest-neighbors contributions was originally calculated by P.R. Wallace[117] and can be expressed as shown in equation A.18 [114], where $f(k)$ is defined in equation A.19 and t' is the next nearest-neighbor transfer integral .

$$E_{\mathrm{2D}}(\vec{k})=\pm t\sqrt{3+f(k)}-t'f(k) \qquad \text{(A.18)}$$

$$f(k)=2\cos\left(\sqrt{3}k_y a\right)+4\cos\left(\frac{\sqrt{3}k_x a}{2}\right)\cos\left(\frac{3k_x a}{2}\right) \qquad \text{(A.19)}$$

The density of states of graphene per unit cell, considering the contributions of the next nearest-neighbors with an assumed value of $t'=0.2t$ and neglecting the contributions of the next nearest-neighbor constributions are shown in Figure A.2 (a) and (b), respectively.

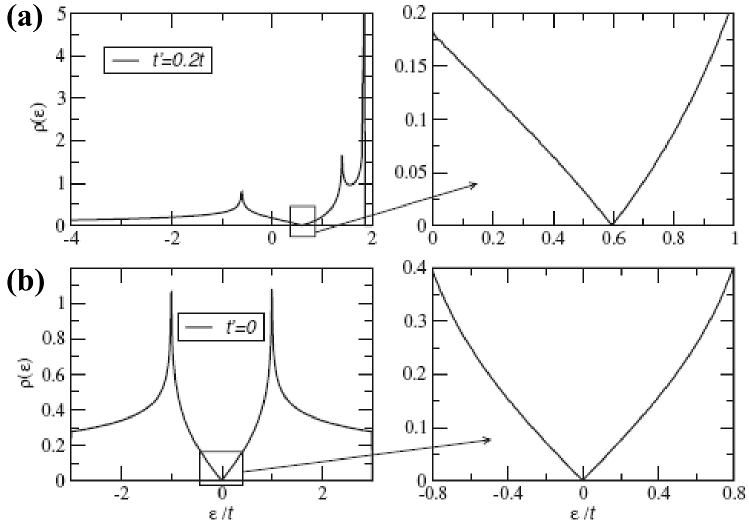

Figure A.2 (a) Density of states of graphene per unit cell as a function of energy considering next nearest neighbors with *t'*=0.2*t*. (b) Density of states of graphene per unit cell as a function of energy neglecting the next nearest neighbors with *t'*=0.Taken from reference [114].

A.2 Structure and Electronic Properties of Carbon Nanotubes

By referring to Figure A.3 it can be seen that the wrap angle θ is defined as the angle between $\overrightarrow{a_1}$ and the chiral vector $\boldsymbol{C}_\mathbf{h}$. The wrap angle is then defined as shown in equation A.20 and varies between 0° and 30° [87]. The diameter of carbon nanotubes is on the order of nanometers and its diameter can be determined through equation A.21, which is obtained through inspection of Figure A.3.

$$\boldsymbol{\theta} = \tan^{-1}\left(\frac{\sqrt{3}\boldsymbol{m}}{2\boldsymbol{n}+\boldsymbol{m}}\right) \tag{A.20}$$

$$\boldsymbol{d}_t = \frac{|\boldsymbol{C}_h|}{\pi} \tag{A.21}$$

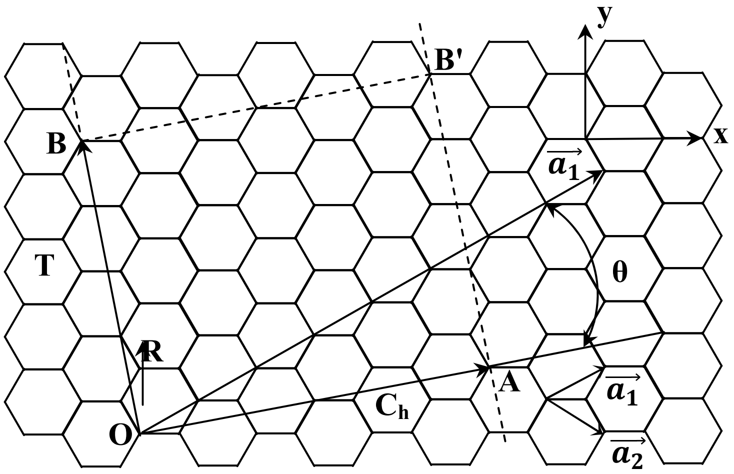

Figure A.3 An unrolled carbon nanotube with (n, m) = (4, 2). The rectangle OAB'B is the unit cell for the carbon nanotube. Adapted from Reference [87].

To get the density of states of CNTs, it is necessary to start with the 2D energy dispersion relation of graphene from equation A.15. The resulting plot of the energy dispersion relation of graphene as a function of k_x and k_y is presented in Figure A.4. For clarity, the first Brillouin zone is drawn below graphene's bandstructure. The reciprocal lattice vectors that are used in reciprocal space are defined in equation A.22. The points Γ, K, and M are high symmetry points that are used for obtaining 1D energy dispersion relations for CNTs [87]. When a carbon nanotube is rolled up from a sheet of graphene a periodic boundary condition can be imposed in the circumferential direction as shown in equation A.23, where j is an integer [118]. The periodic boundary condition only allows a set of wavevectors that satisfy equation A.24 to exist, where λ is the de Broglie wavelength [87].

$$\vec{b}_1 = \frac{2\pi a}{3}\hat{x} + \frac{2\pi a}{\sqrt{3}}y;\ \vec{b}_2 = \frac{2\pi a}{3}\hat{x} - \frac{2\pi a}{\sqrt{3}}y \qquad (A.22)$$

$$\vec{C}\cdot\vec{k} = 2\pi j \qquad (A.23)$$

$$n\lambda = \pi d_t \qquad (A.24)$$

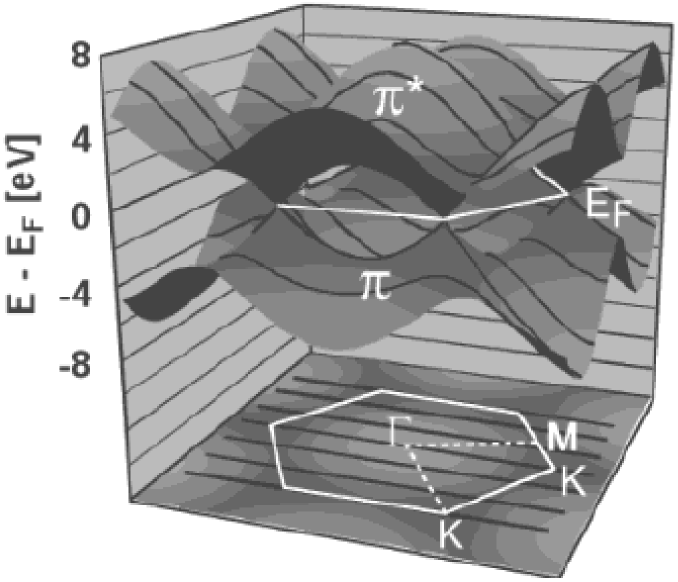

Figure A.4 2D energy dispersion relation of graphene plotted as a function of k_x and k_y. The conduction π^* and valence π bands meet at the six K points (Dirac points). The first Brillouin zone of graphene in reciprocal space is shown below the band structure of graphene. The black lines represent the allowed states of a (3, 3) nanotube or the perpendicular wave vectors that satisfy the equation $\vec{\boldsymbol{C}} \cdot \vec{\boldsymbol{k}} = \boldsymbol{2\pi j}$. Taken from reference [118].

Furthermore, the Dirac points K is where the energy levels lie at zero and thus, a carbon nanotube will have no band gap if the wave vectors pass through the center of one of the Dirac points as is the case for a (3,3) CNT. Similarly, if a wavevector does not pass through the Dirac point a band gap will be created. This results in carbon nanotubes exhibiting either metallic or semiconducting properties depending on the wrap angle of the carbon nanotube.

The angle at which the CNT wraps determines if it is a zigzag, armchair, or chiral nanotube. CNTs with a wrap angle of 0° or indices (n,0) are called zigzag nanotubes, a wrap angle of 30° or indices(n,n) correspond to armchair nanotubes. All other wrap angles correspond to chiral nanotubes. Examples of zigzag, armchair, and chiral nanotubes are shown in Figure A.5.

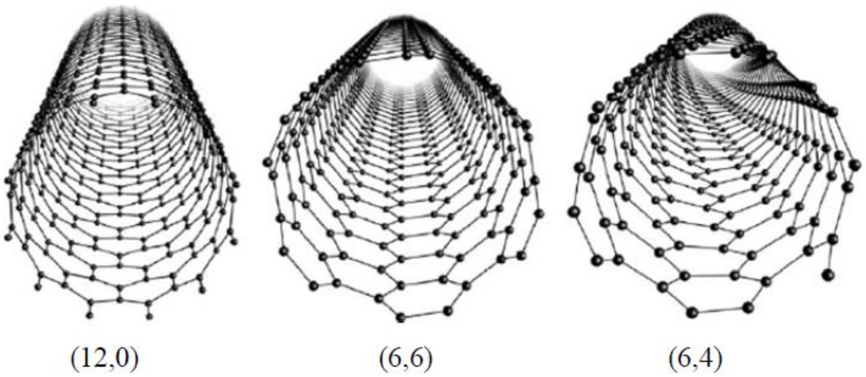

Figure A.5 Atomic structures of (12,0) zigzag, (6,6) armchair, and (6,4) chiral nanotubes. Taken from reference [119].

All armchair CNTs are metallic and other metallic nanotubes can be more generally determined through equation A.25, where q is an integer. Equation A.25 is a direct result of the periodic boundary condition imposed in equation A.24 [120]. All other CNTs that do not satisfy equation A.25 are semiconducting.

$$\boldsymbol{2n + 3m = 3q} \tag{A.25}$$

The 1D energy dispersion relations obtained from the wavevectors passing through the 2D energy dispersion relation in the 1st Brillouin zone can be used to calculate the DOS of CNTs through the use of the zone folding approximation. It is important to note that the zone folding approximation does not take into account the curvature of CNTs[20]. The resulting DOS for a metallic (9,0) SWNT and a semiconducting SWNT (10,0) are shown in Figure A.6 (a) and (b), respectively.

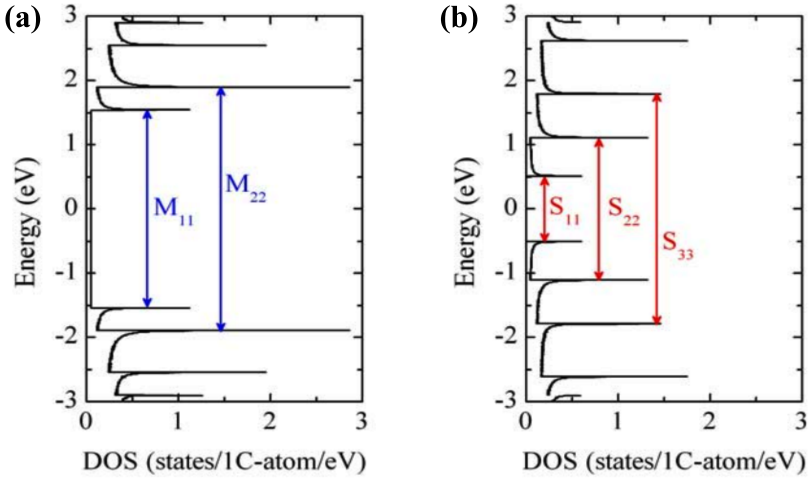

Figure A.6 DOS versus energy for (a) (9,0) and (b) (10,0) SWNT, derived by zone-folding of the band structure of the graphene sheet. Fermi Energy is assumed to be located at 0eV. Taken from Reference [20].

The singularity points in the DOS for both M-SWNT and Sc-SWNT are called van Hove singularities and the distance between them are called energy transitions, labeled M_{11}, M_{22}, S_{11}, S_{22}, and S_{33} in Figure A.6. These energy transition absorption peaks show up in UV-Vis NIR spectroscopy measurements and are an invaluable tool that is used to determine the effectiveness of a dopant and the degree of dedoping after thermal annealing.

APPENDIX B: OTHER SHEET RESISTANCE MEASUREMENT TECHNIQUES

B.1 Two Point Probe Method

A very crude method to measure the sheet resistance is the two-point probe method, which involves the use of a multimeter and two probing wires as shown in Figure B.1a. Typically, the sheet resistance using this method is simply taken as the resistance value read on the multimeter, as was done by Parekh et al.[53], where a R_{sh} as low as 30Ω/sq was claimed. It is clear from the circuit diagram in Figure B.1b that the actual resistance measured from the multimeter is the total resistance, R_T as shown in equation B.1.

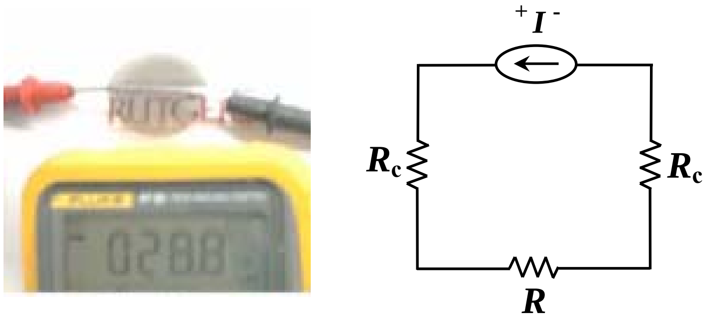

Figure B.1 (a) Picture of two point probe method used to measure sheet resistance. Taken from reference[53] (b) Equivalent circuit diagram of two point probe.

$$R_T = 2R_c + R \tag{B.1}$$

This methodology of using the 2 point probe technique however is incorrect as the sheet resistance is related to the bulk resistance as suggested by equation 3.2. Where the cross-sectional area for circular vacuum filtered films (see Figure B.1a) is πDt, where D is the diameter. By referring to equation 3.2 and substituting the cross-section area for a circular vacuum filtered film and recalling the definition of R_{sh} (equation 2.2) yields equation B.2. If it is assumed that the two probes are measured at a length that is approximately equal to the diameter of the film. Equation 3.7 can be simplified into equation B.3.

$$\boldsymbol{R} = \frac{\boldsymbol{\rho}}{\boldsymbol{t}}\frac{\boldsymbol{L}}{\boldsymbol{\pi D}} = \boldsymbol{R}_{\mathbf{sh}}\frac{\boldsymbol{L}}{\boldsymbol{\pi D}} \tag{B.2}$$

$$\boldsymbol{R} \approx \frac{\boldsymbol{R}_{\mathbf{sh}}}{\boldsymbol{\pi}} \tag{B.3}$$

This means that the bulk resistance is π times larger than the sheet resistance. Therefore, the true R_{sh} at the most can be theoretically underestimated by a factor of π. This is significant and can lead to misleading results; however it is important to note that an underestimation of a factor of π is not likely as the contact resistance, which is typically not negligible, has not been accounted for in the two-point probe technique. Therefore, the inability to properly indentify the resistance contributions from the contact resistance makes the two point probe technique unreliable and difficult to extract the true R_{sh}.

B.2 Four Point Probe Method

The four-point probe method avoids the issue of contact resistance in sheet resistance measurements and was first developed by Kelvin[121]. In this method a constant current source is applied to the outer probes and a voltmeter is connected to the inner probes to measure the voltage drop. A four point probe schematic and electrical circuit diagram are shown in Figure B.2 a and b, respectively, where the spacing between electrical probes S_1, S_2, S_3 are equal to each other or simply equal to S. In Figure B.2 the voltage drops attributed to the contact resistances connecting the voltmeter to the bulk resistance are considered to be negligible and can therefore be neglected in the circuit diagram. The reason they are considered to be negligible is that by the principle of operation of a voltmeter, the voltage is measured over an equivalent open-circuit. In other words, even if there were resistance between the contact of the voltmeter and the bulk resistance they would be infinitely large and in parallel with the bulk resistance. Applying the rule for resistors in parallel, the contributions are simply 1/∞ or equivalently zero.

Therefore, the bulk resistance can then simply be determined by using Ohm's law across it as is shown in equation B.4. The contact resistance can be extracted from equation B.1 which applies to the outer probes.

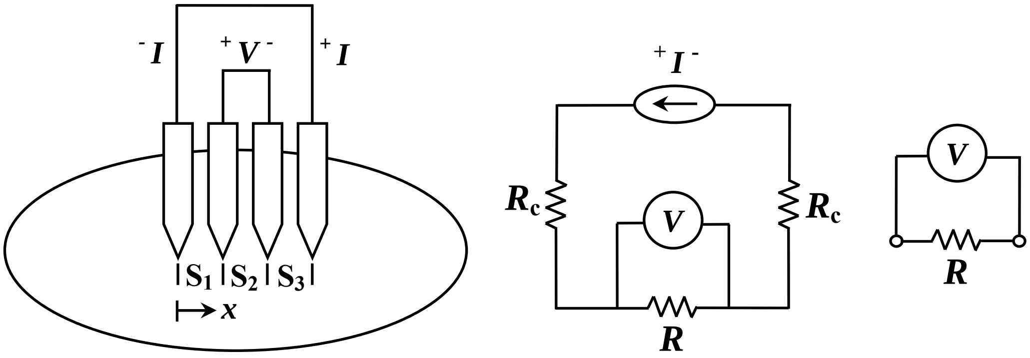

Figure B.2 (a) Schematic of four point probe method used to measure sheet resistance. Adapted from references [122, 123] (b) Equivalent circuit diagram of four point probe. (c) Open-circuit voltage measured by voltmeter across *R*.

$$R = \frac{V}{I} \tag{B.4}$$

To obtain the sheet resistance for a circular sample as shown in Figure B.2a it is necessary to start from the differential form of equation 3.2 across the inner probes as shown in equation B.6. Integrating both sides and expanding yields equation B.7. Evaluating the integral and noting that R_{sh} is defined as the resistivity divided by the thickness(equation 2.2) yields equation B.8 [123].

$$dR = \rho \frac{dx}{A_c} \tag{B.6}$$

$$R = \int_{S}^{2S} \frac{\rho}{t} \frac{dx}{2x\pi} \tag{B.7}$$

$$R = R_{sh} \frac{\ln(2)}{2\pi} \tag{B.8}$$

This implies that even though the four point probe method resolves the contact resistance problem there needs to be a correction factor, *k*, to account for the geometry of the sample. To finish this example so that the correction factor for a circular sample is similar to what is given in literature, a current balance for the inner probes shows that the current passing across *R* is in fact 2*I* or twice the current from the current source. Applying Ohm's law gives *R*=V/(2*I*) combining this result with equation yields equation B.9 and the correction factor is ~4.53 which is agreement with literature [122].

$$\boldsymbol{R}_{\mathbf{sh}} = \frac{\pi}{\ln(2)} \frac{V}{I} = k \frac{V}{I} \tag{B.9}$$

Although the four point probe measurement is an improvement from the two-point probe the correction factor needed to calculate R_{sh} is dependent upon the geometry. Due to the difficulty in producing samples with precisely the exact same geometry, unwanted experimental error may arise from using a four point probe method. However, the transfer length method (TLM), an extension of the transmission line method, is a suitable technique to accurately measure the sheet resistance of CBN transparent electrode.

APPENDIX C: EFFECTS OF PROCESSING CONDITIONS AND CONTAMINANTS ON TRANSPARENT ELECTRODES

C.1 Effect of Processing Conditions on Carbon Based Nanomaterials

Throughout the course of this work it was experimentally observed that the processing conditions had a direct impact on the conductivity of as-made CBN electrodes. Besides the presence of Fluorinated Hydrocarbons contaminants (see section 2.5.2) provided unintentionally by vendor Nanointegris and aggregation of CBNs (well documented in literature for SWNTs) in solution overtime that the author had limited control over, other processing conditions were investigated. Of all the CBN solutions used in this work, the graphene puresheets (GPS) research grade solution was found to be the most sensitive to processing conditions. As a direct consequence of GPS solutions sensitivity to processing conditions it was possible to pinpoint which processing conditions needed to be addressed to improve the fabrication of CBN electrodes. Unfortunately, due to the late availability of this solution (samples available around March 2010 and solutions purchased in July 2010) all samples prepared in this work were not prepared with optimal processing conditions.

To address the issue of inconsistency in as-made samples throughout the course of this work, with what was observed in literature, and even in different stages of this work; a set of experiments with distinct processing conditions was conducted to pinpoint the processing conditions that affected the CBN electrodes the most. In this experiment it was found that the condition of the glass frit old (used for at least 2 years) or new (used at most 2 months) and the resistivity of DI water in MΩ-cm were the most influential in determining the conductivity of the vacuum filtered CBN electrodes. Shown in Figure C.1a and b are pictures of the new and old glass frits, respectively. From inspection of Figure C.2 it is easily noticed that the new glass frit is smoother than the old glass frit.

Utilizing the new glass frit should result in smoother vacuum filtered films. Thus, it is hypothesized that the smoother films will have more interparticle contacts than the old frit. The logic for this is that the rougher films will likely have CBN poking out on the surface of the electrode causing shorts; whereas the smoother films will have the tendency to lie flat thereby creating more interparticle contacts.

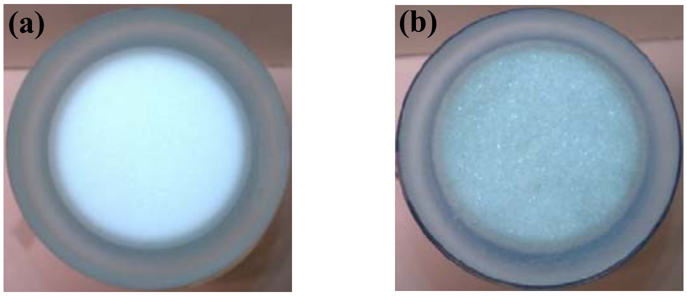

Figure C.1 (a) Picture of new glass frit. (b) Picture of old glass frit. There is a noticeable difference between the two glass frits. The new glass frit is smoother than the old glass frit, thus resulting in smoother vacuum filtered films.

The results of the experiment are presented in Table C.1. For clarity high quality and low quality DI water will correspond to resistivities of ~16 MΩ-cm and ~0.5 MΩ-cm, respectively.

Table C.1 Comparison of as-made graphene puresheets electrodes fabricated with distinct processing conditions.

As-made	**Processing Conditions**			
R_{sh} (Ω/sq)	**New Glass Frit**	**Old Glass Frit**	**Low Quality DI Water**	**High Quality DI Water**
50,654		X	X	
26,462		X		X
13,299	X			X

From the results obtained in Table C.1it is clear that having a relatively new frit and using higher quality DI water are essential for obtaining high quality CBN electrodes. It is suggested that lower quality DI water has a negative impact on the conductivity of CBN electrodes due to the unfiltered salts and minerals causing shorts in the film. However, further research would need to be performed to validate this theory. For the condition of the glass frit, it is hypothesized that the older glass frits will likely have been clogged up due to heavy usage over a 2 year time span. This would likely cause the vacuum filtered films, at the nanoscale, to have uneven patches caused by clogged material over the surface areas of the glass frit. This would likely increase the surface roughness of vacuum filtered film and decrease the number of contact points between CBNs. As a result the conductivity of the films would be negatively impacted.

Furthermore, it was also found that processing conditions had to some extent an irreversible negative impact on the conductivity of CBN electrodes. In this next experiment the same processing conditions were repeated for GPS films annealed in Ar at 1000°C. The results are presented in Table C.2.

Table C.2 Comparison of Ar anneal graphene puresheets electrodes fabricated with distinct processing conditions.

Ar Annealed 1000°C	**Processing Conditions**			
R_{sh} **(Ω/sq)**	**New Glass Frit**	**Old Glass Frit**	**Low Quality DI Water**	**High Quality DI Water**
3,554		X	X	
3,154		X		X
2,416	X			X

This study has addressed the issue of inconsistencies observed of fabricated CBN transparent electrodes in this work. As a result of not pinpoint these processing conditions early in the stage of this research, it is reiterated that the goal of this thesis is not to fabricate CBN electrodes with the best optoelectronic properties, but rather to observe, understand, and adequately describe the underlying physics involved throughout the course of this work.

C.2 Complications with Fluorinated Hydrocarbon Contaminants

Although Nanointegris has been able to consistently deliver type sorted SWNTs, which have been invaluable in the research conducted in this work, the DGUC process is not without its problems, as fluorinated hydrocarbon contaminants have been detected in solutions sent by Nanointegris. These fluorinated hydrocarbon contaminants cannot be completely eliminated from Nanointegris' process. The fluorinated hydrocarbon contaminants are immiscible in water and when it is present in the SWNT solution it can cause phase separation at the macroscopic and microscopic scale. Shown in Figure C.2e a and b is a picture of spots forming at the macroscopic scale for a Sc-SWNT electrode and SEM image at 2000x magnification of a doped MSWNT that was annealed prior to doping at 600°C, respectively.

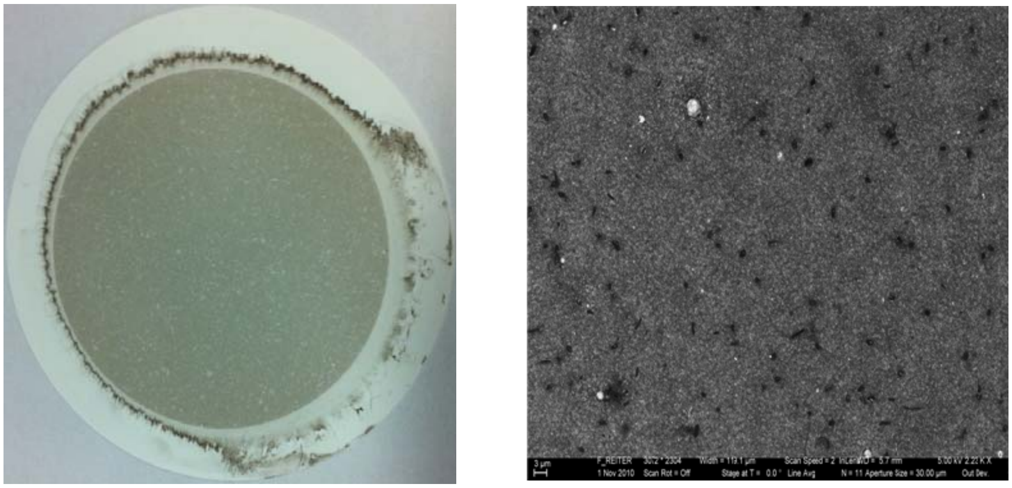

Figure C.2 (a) Photo of Semiconducting SWNT film vacuum filtered from solution containing fluorinated hydrocarbon contaminants. (b) SEM image of doped Metallic SWNT Film Annealed at 600C containing contaminants.

This fluorinated hydrocarbon is suspected to stick to the walls of any glassware it comes into contact with and thereby contaminating any new films that were made using the same glassware. The spots that form on the SWNT surface compromise the film integrity, quality, and negatively impact the sheet resistance of SWNT films due to the higher presence of dead spots. It is not known how to remove this chemical. Furthermore, the Fluorine in this contaminant is suspected to bond to the walls of the CNT as the Fluorine was still detected by XPS to be present on films that were annealed to temperatures of 1000°C. For future work, it is suggested to use ultrasonic spray coating to deposit these films to avoid forming breaks in SWNT films.

REFERENCES

1. Cui, J., et al., *Indium Tin Oxide Alternatives—High Work Function Transparent Conducting Oxides as Anodes for Organic Light-Emitting Diodes.* Advanced materials, 2001. **13**(19): p. 1476-1480.
2. De, S. and J.N. Coleman, *Are There Fundamental Limitations on the Sheet Resistance and Transmittance of Thin Graphene Films?* Acs Nano, 2010. **4**(5): p. 2713-2720.
3. Leterrier, Y., et al., *Mechanical integrity of transparent conductive oxide films for flexible polymer-based displays.* Thin Solid Films, 2004. **460**(1-2): p. 156-166.
4. Saran, N., et al., *Fabrication and characterization of thin films of single-walled carbon nanotube bundles on flexible plastic substrates.* Journal of the American Chemical Society, 2004. **126**(14): p. 4462-4463.
5. Bae, S., et al., *Roll-to-roll production of 30-inch graphene films for transparent electrodes.* Nature Nanotechnology, 2010. **5**(8): p. 574-578.
6. Phillips, J.M., et al., *TRANSPARENT CONDUCTING THIN-FILMS OF GAINO3.* Applied Physics Letters, 1994. **65**(1): p. 115-117.
7. Chkoda, L., et al., *Work function of ITO substrates and band-offsets at the TPD/ITO interface determined by photoelectron spectroscopy.* Synthetic Metals, 2000. **111**: p. 315-319.
8. Tolcin, A.C. *Indium Statistics and Information*. 2011 [cited 2011 April 1]; Available from: http://minerals.usgs.gov/minerals/pubs/commodity/indium/**.**
9. *Chinese Indium Strategies: Threats and Opportunities for Displays, Photovoltaics and Electronics*. [cited 2011 April 2]; Available from: http://nanomarkets.net/market_reports/report/chinese_indium_strategies_threats_and_opportunities_for_displays_photovoltaics_and_electronics/**.**
10. Minami, T., *Transparent conducting oxide semiconductors for transparent electrodes.* Semiconductor Science and Technology, 2005. **20**(4): p. S35-S44.
11. Carter, G., M.J. Nobes, and D.G. Armour, *THE EROSION ENERGY EFFICIENCY OF SPUTTERING.* Vacuum, 1982. **32**(8): p. 509-512.
12. *Sony Color Flexible OLED: worlds first 16.7 million bendy display*. [cited 2011 March 21]; Available from: http://www.product-reviews.net/2007/05/25/sony-color-flexible-oled-worlds-first-167-million-bendy-display/**.**
13. *Organic solar cells*. [cited 2011 March 21]; Available from: http://solarpower.e-bookz.info/?p=159**.**
14. *Solid-State Lighting Research and Development: Multi Year Program Plan*, U.S.D.o. Energy, Editor. March 2010: Washington D.C. p. 162.
15. *White OLED Outlook Brightens with Efficiency Breakthrough*. [cited 2011 March 21]; Available from: http://pressroom.geconsumerproducts.com/pr/ge/OLED_KM_2010.aspx**.**
16. Pardo, D.A., G.E. Jabbour, and N. Peyghambarian, *Application of Screen Printing in the Fabrication of Organic Light-Emitting Devices.* Advanced materials, 2000. **12**(17): p. 1249-1252.
17. Smalley, R.E., *Future Global Energy Prosperity: The Terawatt Challenge.* MRS Bulletin, 2005. **30**(06): p. 412-417.

18. Zweibel, K., *The Terawatt Challenge for Thin-Film PV*, N.R.E. Laboratory, Editor. 2005. p. 49.
19. Kazmerski, L. *Best Research-Cell Efficiencies*. 2011 [cited 2011 March 30]; Available from**:** www.nrel.gov/pv.
20. Jackson, R., *Development of single wall carbon nanotube transparent conductive electrodes for organic electronics*. 2009, Georgia Institute of Technology: United States -- Georgia. p. 223.
21. Kippelen, B. and J.-L. Bredas, *Organic photovoltaics.* Energy & Environmental Science, 2009. **2**(3): p. 251-261.
22. Minami, T., *New n-Type Transparent Conducting Oxides.* MRS Bulletin, 2000. **25**(08): p. 38-44.
23. Jiang, X., et al., *Aluminum-doped zinc oxide films as transparent conductive electrode for organic light-emitting devices.* Applied Physics Letters, 2003. **83**(9): p. 1875-1877.
24. Louwet, F., et al., *PEDOT/PSS: synthesis, characterization, properties and applications.* Synthetic Metals, 2003. **135**(1-3): p. 115-117.
25. Tung, V.C., et al., *Low-Temperature Solution Processing of Graphene-Carbon Nanotube Hybrid Materials for High-Performance Transparent Conductors.* Nano Letters, 2009. **9**(5): p. 1949-1955.
26. Saran, N., et al., *Fabrication and Characterization of Thin Films of Single-Walled Carbon Nanotube Bundles on Flexible Plastic Substrates.* Journal of the American Chemical Society, 2004. **126**(14): p. 4462-4463.
27. Ng, M.H.A., et al., *Efficient coating of transparent and conductive carbon nanotube thin films on plastic substrates.* Nanotechnology, 2008. **19**(20).
28. Wu, Z.C., et al., *Transparent, conductive carbon nanotube films.* Science, 2004. **305**(5688): p. 1273-1276.
29. Tenent, R.C., et al., *Ultrasmooth, Large-Area, High-Uniformity, Conductive Transparent Single-Walled-Carbon-Nanotube Films for Photovoltaics Produced by Ultrasonic Spraying.* Advanced materials, 2009. **21**(31): p. 3210-+.
30. Yim, J.H., et al. *Fabrication of transparent single wall carbon nanotube films with low sheet resistance*. 2008: AVS.
31. Small, W.R. and M. in het Panhuis, *Inkjet Printing of Transparent, Electrically Conducting Single-Walled Carbon-Nanotube Composites.* Small, 2007. **3**(9): p. 1500-1503.
32. Ausman, K.D., et al., *Organic solvent dispersions of single-walled carbon nanotubes: Toward solutions of pristine nanotubes.* Journal of Physical Chemistry B, 2000. **104**(38): p. 8911-8915.
33. Stankovich, S., et al., *Graphene-based composite materials.* Nature, 2006. **442**(7100): p. 282-286.
34. Gu, W.T., et al., *Graphene sheets from worm-like exfoliated graphite.* Journal of Materials Chemistry, 2009. **19**(21): p. 3367-3369.
35. Green, A.A. and M.C. Hersam, *Solution Phase Production of Graphene with Controlled Thickness via Density Differentiation.* Nano Letters, 2009. **9**(12): p. 4031-4036.
36. Reina, A., et al., *Large Area, Few-Layer Graphene Films on Arbitrary Substrates by Chemical Vapor Deposition.* Nano Letters, 2009. **9**(1): p. 30-35.

37. Kymakis, E., E. Stratakis, and E. Koudoumas, *Integration of carbon nanotubes as hole transport electrode in polymer/fullerene bulk heterojunction solar cells.* Thin Solid Films, 2007. **515**(24): p. 8598-8600.
38. Hu, L., D.S. Hecht, and G. Gruner, *Percolation in transparent and conducting carbon nanotube networks.* Nano Letters, 2004. **4**(12): p. 2513-2517.
39. Kim, H., et al., *Effect of film thickness on the properties of indium tin oxide thin films.* Journal of Applied Physics, 2000. **88**(10): p. 6021-6025.
40. Malard, L.M., et al., *Raman spectroscopy in graphene.* Physics Reports-Review Section of Physics Letters, 2009. **473**(5-6): p. 51-87.
41. Eklund, P.C., J.M. Holden, and R.A. Jishi, *Vibrational modes of carbon nanotubes; Spectroscopy and theory.* Carbon, 1995. **33**(7): p. 959-972.
42. Geng, H.Z., et al., *Effect of acid treatment on carbon nanotube-based flexible transparent conducting films.* Journal of the American Chemical Society, 2007. **129**(25): p. 7758-+.
43. Geng, H.-Z., K.K. Kim, and Y.H. Lee. *Recent progress in carbon nanotube-based flexible transparent conducting film*. 2008: SPIE.
44. Iijima, S., *HELICAL MICROTUBULES OF GRAPHITIC CARBON.* Nature, 1991. **354**(6348): p. 56-58.
45. Ebbesen, T.W. and P.M. Ajayan, *LARGE-SCALE SYNTHESIS OF CARBON NANOTUBES.* Nature, 1992. **358**(6383): p. 220-222.
46. Bethune, D.S., et al., *COBALT-CATALYZED GROWTH OF CARBON NANOTUBES WITH SINGLE-ATOMIC-LAYERWALLS.* Nature, 1993. **363**(6430): p. 605-607.
47. Yurekli, K., C.A. Mitchell, and R. Krishnamoorti, *Small-angle neutron scattering from surfactant-assisted aqueous dispersions of carbon nanotubes.* Journal of the American Chemical Society, 2004. **126**(32): p. 9902-9903.
48. Strano, M.S., et al., *The role of surfactant adsorption during ultrasonication in the dispersion of single-walled carbon nanotubes.* Journal of Nanoscience and Nanotechnology, 2003. **3**(1-2): p. 81-86.
49. Islam, M.F., et al., *High Weight Fraction Surfactant Solubilization of Single-Wall Carbon Nanotubes in Water.* Nano Letters, 2003. **3**(2): p. 269-273.
50. Okazaki, T., et al., *Photoluminescence Mapping of "As-Grown" Single-Walled Carbon Nanotubes: A Comparison with Micelle-Encapsulated Nanotube Solutions.* Nano Letters, 2005. **5**(12): p. 2618-2623.
51. Anson-Casaos, A., J.M. Gonzalez-Dominguez, and M.T. Martinez, *Separation of single-walled carbon nanotubes from graphite by centrifugation in a surfactant or in polymer solutions.* Carbon, 2010. **48**(10): p. 2917-2924.
52. Unalan, H.E., et al., *Design criteria for transparent single-wall carbon nanotube thin-film transistors.* Nano Letters, 2006. **6**(4): p. 677-682.
53. Parekh, B.B., et al., *Improved conductivity of transparent single-wall carbon nanotube thin films via stable postdeposition functionalization.* Applied Physics Letters, 2007. **90**(12).
54. Zhou, Y.X., L.B. Hu, and G. Gruner, *A method of printing carbon nanotube thin films.* Applied Physics Letters, 2006. **88**(12).
55. Kaempgen, M., G.S. Duesberg, and S. Roth, *Transparent carbon nanotube coatings.* Applied Surface Science, 2005. **252**(2): p. 425-429.

56. Ferrer-Anglada, N., et al., *Synthesis and characterization of carbon nanotube-conducting polymer thin films.* Diamond and Related Materials, 2004. **13**(2): p. 256-260.
57. Moon, J.S., et al., *Transparent conductive film based on carbon nanotubes and PEDOT composites.* Diamond and Related Materials, 2005. **14**(11-12): p. 1882-1887.
58. Zhang, D., et al., *Transparent, Conductive, and Flexible Carbon Nanotube Films and Their Application in Organic Light-Emitting Diodes.* Nano Letters, 2006. **6**(9): p. 1880-1886.
59. Jackson, R., et al., *Stability of Doped Transparent Carbon Nanotube Electrodes.* Advanced Functional Materials, 2008. **18**(17): p. 2548-2554.
60. Collins, P.C., M.S. Arnold, and P. Avouris, *Engineering carbon nanotubes and nanotube circuits using electrical breakdown.* Science, 2001. **292**(5517): p. 706-709.
61. Li, H., et al., *Selective Interactions of Porphyrins with Semiconducting Single-Walled Carbon Nanotubes.* Journal of the American Chemical Society, 2004. **126**(4): p. 1014-1015.
62. Arnold, M.S., et al., *Sorting carbon nanotubes by electronic structure using density differentiation.* Nature Nanotechnology, 2006. **1**(1): p. 60-65.
63. Green, A.A. and M.C. Hersam, *Ultracentrifugation of single-walled nanotubes.* Materials Today, 2007. **10**(12): p. 59-60.
64. Green, A.A. and M.C. Hersam, *Colored Semitransparent Conductive Coatings Consisting of Monodisperse Metallic Single-Walled Carbon Nanotubes.* Nano Letters, 2008. **8**(5): p. 1417-1422.
65. Lu, F.S., et al., *Metallic single-walled carbon nanotubes for transparent conductive films.* Chemical Physics Letters, 2010. **497**(1-3): p. 57-61.
66. Blackburn, J.L., et al., *Transparent Conductive Single-Walled Carbon Nanotube Networks with Precisely Tunable Ratios of Semiconducting and Metallic Nanotubes.* Acs Nano, 2008. **2**(6): p. 1266-1274.
67. Jackson, R.K., et al., *Evaluation of Transparent Carbon Nanotube Networks of Homogeneous Electronic Type.* Acs Nano, 2010. **4**(3): p. 1377-1384.
68. Bower, C., et al., *Intercalation and partial exfoliation of single-walled carbon nanotubes by nitric acid.* Chemical Physics Letters, 1998. **288**(2-4): p. 481-486.
69. Zhou, W., et al., *Charge transfer and Fermi level shift in p -doped single-walled carbon nanotubes.* Physical Review B, 2005. **71**(20): p. 205423.
70. Graupner, R., et al., *Doping of single-walled carbon nanotube bundles by Bronsted acids.* Physical Chemistry Chemical Physics, 2003. **5**: p. 5472-5476.
71. Novoselov, K.S., et al., *Electric field effect in atomically thin carbon films.* Science, 2004. **306**(5696): p. 666-669.
72. Berger, C., et al., *Ultrathin Epitaxial Graphite: 2D Electron Gas Properties and a Route toward Graphene-based Nanoelectronics.* The Journal of Physical Chemistry B, 2004. **108**(52): p. 19912-19916.
73. Kroto, H.W., et al., *C60: Buckminsterfullerene.* Nature, 1985. **318**(6042): p. 162-163.
74. Geim, A.K. and K.S. Novoselov, *The rise of graphene.* Nature Materials, 2007. **6**(3): p. 183-191.

75. Park, S. and R.S. Ruoff, *Chemical methods for the production of graphenes.* Nat Nano, 2009. **4**(4): p. 217-224.
76. Di, C.-a., et al., *Patterned Graphene as Source/Drain Electrodes for Bottom-Contact Organic Field-Effect Transistors.* Advanced materials, 2008. **20**(17): p. 3289-3293.
77. Palacios, T., A. Hsu, and W. Han, *Applications of graphene devices in RF communications.* Communications Magazine, IEEE, 2010. **48**(6): p. 122-128.
78. Dan, Y., et al., *Intrinsic Response of Graphene Vapor Sensors.* Nano Letters, 2009. **9**(4): p. 1472-1475.
79. Fowler, J.D., et al., *Practical Chemical Sensors from Chemically Derived Graphene.* Acs Nano, 2009. **3**(2): p. 301-306.
80. Bolotin, K.I., et al., *Ultrahigh electron mobility in suspended graphene.* Solid State Communications, 2008. **146**(9-10): p. 351-355.
81. Dürkop, T., et al., *Extraordinary Mobility in Semiconducting Carbon Nanotubes.* Nano Letters, 2003. **4**(1): p. 35-39.
82. Jacoboni, C., et al., *A review of some charge transport properties of silicon.* Solid-State Electronics, 1977. **20**(2): p. 77-89.
83. Morin, F.J., *Lattice-Scattering Mobility in Germanium.* Physical Review, 1954. **93**(1): p. 62.
84. Fawcett, W., A.D. Boardman, and S. Swain, *Monte Carlo determination of electron transport properties in gallium arsenide.* Journal of Physics and Chemistry of Solids, 1970. **31**(9): p. 1963-1990.
85. Barnes, T.M., et al., *Reversibility, dopant desorption, and tunneling in the temperature-dependent conductivity of type-separated, conductive carbon nanotube networks.* Acs Nano, 2008. **2**(9): p. 1968-1976.
86. Bulusu, A., *Post doctoral research fellow in Dr. Samuel Graham's research group* 2009, George Woodruff School of Mechanical Engineering, Georgia Institute of Technology.
87. Dresselhaus, M.S. and P.C. Eklund, *Phonons in carbon nanotubes.* Advances in Physics, 2000. **49**(6): p. 705-814.
88. Shockley, W., *Research and investigation of inverse epitaxial UHF power transistors*, W.P.A.F.B. Air Force Atomic Laboratory, Ohio A1-TOR-64-207, Editor. 1964.
89. Berger, H.H., *Models for contacts to planar devices.* Solid-State Electronics, 1972. **15**(2): p. 145-158.
90. Meier, D.L. and D.K. Schroder, *Contact resistance: Its measurement and relative importance to power loss in a solar cell.* Electron Devices, IEEE Transactions on, 1984. **31**(5): p. 647-653.
91. Jackson, R. and S. Graham, *Specific contact resistance at metal/carbon nanotube interfaces.* Applied Physics Letters, 2009. **94**(1): p. 012109.
92. Oussalah, S., B. Djezzar, and R. Jerisian, *A comparative study of different contact resistance test structures dedicated to the power process technology.* Solid-State Electronics, 2005. **49**(10): p. 1617-1622.
93. Look, D.C., *Electrical Characterization GaAs Materials and Devices*. Design and Measurement in Electronic Engineering, ed. H.L.G. D. V. Morgan. 1989, Chichester: John Wiley & Sons. 290.

94. Cohen, S.S., *CONTACT RESISTANCE AND METHODS FOR ITS DETERMINATION.* Thin Solid Films, 1983. **104**(3-4): p. 361-379.

95. *Work Functions for Photoelectric Effect.* [cited 2011 March 21]; Available from: http://hyperphysics.phy-astr.gsu.edu/hbase/tables/photoelec.html**.**

96. Shan, B. and K. Cho, *First Principles Study of Work Functions of Single Wall Carbon Nanotubes.* Physical Review Letters, 2005. **94**(23): p. 236602.

97. Shi, Y., et al., *Work Function Engineering of Graphene Electrode via Chemical Doping.* Acs Nano, 2010. **4**(5): p. 2689-2694.

98. Marayuma, S. *Shigeo Marayuma's Fullerene and Carbon Nanotube Site.* 2007 [cited 2011 March 21]; Available from: http://www.photon.t.u-tokyo.ac.jp/~maruyama/nanotube.html**.**

99. Beechem, T.E., III, *Metrology of gallium nitride electronics using micro-Raman spectroscopy*. 2008, ProQuest, UMI Dissertations Publishing. p. n/a.

100. Loudon, R., *The Raman effect in crystals.* Advances in Physics, 2001. **50**(7): p. 813 - 864.

101. Zhu, Y., et al., *Graphene and Graphene Oxide: Synthesis, Properties, and Applications.* Advanced materials, 2010. **22**(35): p. 3906-3924.

102. Bulusu, A., *Post doctoral research fellow in Dr. Samuel Graham's research group*. 2010, George Woodruff School of Mechanical Engineering, Georgia Institute of Technology.

103. Frank, O., et al., *In-situ Vis/NIR spectroelectrochemistry of single-walled carbon nanotubes enriched with (6,5) tubes.* physica status solidi (b), 2008. **245**(10): p. 2239-2242.

104. Tsai, J., Li J, Tseng A *Defect Healing of Carbon Nanotubes by Rapid Vacuum Arc Annealing* in *MRS Symp. Proc.* 2008.

105. Ci, L., et al., *Annealing amorphous carbon nanotubes for their application in hydrogen storage.* Applied Surface Science, 2003. **205**(1-4): p. 39-43.

106. Li, C.Y., et al., *Graphene Nano-"patches" on a Carbon Nanotube Network for Highly Transparent/Conductive Thin Film Applications.* Journal of Physical Chemistry C, 2010. **114**(33): p. 14008-14012.

107. Xin, G.Q., et al., *A graphene sheet exfoliated with microwave irradiation and interlinked by carbon nanotubes for high-performance transparent flexible electrodes.* Nanotechnology, 2010. **21**(40).

108. Lee, J.H., et al., *One-Step Exfoliation Synthesis of Easily Soluble Graphite and Transparent Conducting Graphene Sheets.* Advanced materials, 2009. **9999**(9999): p. NA.

109. Mattevi, C., et al., *Evolution of Electrical, Chemical, and Structural Properties of Transparent and Conducting Chemically Derived Graphene Thin Films.* Advanced Functional Materials, 2009. **19**(16): p. 2577-2583.

110. Balog, R., et al., *Bandgap opening in graphene induced by patterned hydrogen adsorption.* Nat Mater, 2010. **9**(4): p. 315-319.

111. Elias, D.C., et al., *Control of Graphene's Properties by Reversible Hydrogenation: Evidence for Graphane.* Science, 2009. **323**(5914): p. 610-613.

112. Hata, K., et al., *Water-Assisted Highly Efficient Synthesis of Impurity-Free Single-Walled Carbon Nanotubes.* Science, 2004. **306**(5700): p. 1362-1364.

113. Datta, S., *ECE 495N Lecture 21: Graphene Bandstructures*. 2008.

114. Castro Neto, A.H., et al., *The electronic properties of graphene.* Reviews of Modern Physics, 2009. **81**(1): p. 109-162.
115. Datta, S., *ECE 495N Lecture 23: Density of States II*. 2008.
116. Saito, R., G. Dresselhaus, and M.S. Dresselhaus, *Trigonal warping effect of carbon nanotubes.* Physical Review B, 2000. **61**(4): p. 2981.
117. Wallace, P.R., *THE BAND THEORY OF GRAPHITE.* Physical Review, 1947. **71**(9): p. 622-634.
118. Avouris, P., *Molecular Electronics with Carbon Nanotubes.* Accounts of Chemical Research, 2002. **35**(12): p. 1026-1034.
119. Charlier, J.C., X. Blase, and S. Roche, *Electronic and transport properties of nanotubes.* Reviews of Modern Physics, 2007. **79**(2): p. 677-732.
120. Datta, S., *Quantum Transport: Atom to Transistor*. 2005, Cambridge: Cambridge University Press. 418.
121. Thomson, S.W., *Reprint of Papers on Electrostatics and Magnetism*. 1884, London: MacMillan.
122. Smits, F.M., *MEASUREMENT OF SHEET RESISTIVITIES WITH THE 4-POINT PROBE.* Bell System Technical Journal, 1958. **37**(3): p. 711-718.
123. Chan, J. *Four-Point Probe Manual.* 1994 [cited 2011 January 11]; Available from: http://microlab.berkeley.edu/ee143/Four-Point_Probe/**.**